Numerical modelling and optimization of new RHS column-to-I beam connections.

Wu, Jian

Numerical Modelling and Optimization of New RHS Column-to-I Beam Connections

by

Jian Wu M.Eng

A thesis submitted to the Swansea University for degree of Doctor of Philosophy

May 2013

Civil and Computational Engineering Centre, College of Engineering, Swansea University

ProQuest LLC.
789 East Eisenhower Parkway
P.O. Box 1346
Ann Arbor, MI 48106 – 1346

Acknowledgments

I would like to express my gratitude to my supervisors, Prof. Y.T.Feng and Dr. C.F.Li, for the help and guidance I received throughout this project. This thesis would not have been completed without their contribution.

I would like to thank Professor Y. Kurobane and Professor Y. Makino, my former advisor in Kumamoto University, Japan for the guidance and support in my early years of study, I will miss them forever.

I much acknowledge my son, Wu tian hong, for his understanding and stay in Swansea two months with me.

I would also like to thank my brother – Mr Wu yi.

I wish to express my thanks to my wife, Mrs Fang xiao qing, a strong female, who supports throughout my study.

I would like to thank my mother-Mrs Fu yi fang to give me selfless love, I owe her so much.

Finally, I would like to thank my father-Mr Wu fu qiang who had already left this world when I started my Ph.D research. I would like to tell him that I have already completed my study, I will miss him forever.

Abstract

The fracture of the connections in large earthquake are caused not only by the conditions of strain rate, material properties of steel, welding detail of scallop, tack welding and end tabs, but also by the forms of column-beam connections. In the 1994 Northridge earthquake (USA), brittle facture initiated at a very low level of plastic demand, and in some cases, structure remained nearly elastic. In the 1995 Kobe earthquake (Japan), however, majority of rectangular hollow section (RHS) column-to-beam connections that fractured during the earthquake accompanied extensive yielding or local buckling at beam-ends. After the earthquake, improvement of connection design was proposed and various beam-to-column connections were recommended to be configured with sufficient strength so that plastic hinges occur within the beam span and away from the face of the column (SAC Joint Venture 1995). One way to reach the sufficient strength of a connection is to reinforce the beam ends by additional members or plates. Another approach is to reduce the cross section of the beam intentionally to produce an intended plastic hinge zone located away from the column face. The researchers hope to develop a new design concept for avoidance of brittle facture. Thus, the research described the current project focused on the development of finite element models to find optimized designs for avoiding premature occurrences of brittle fracture in RHS column-to-I beam connections.

The thesis firstly describes the validation of finite element models against experimental results. The ABAQUS finite element package is used to simulate the experimental behaviour observed in tests. The comparison shows an accurate correlation between the finite element and experimental results of the connection behaviour. This proves that the finite element method is capable of accurate predicting RHS column-to-I beam connection behaviour. Subsequently, two optimized joints, based on weakening the beam section, are proposed and

discussed. Particularly, it provides an alternative way to develop some new design concepts.

For partially restrained column-to-beam connections, the moment-rotation curves are of great importance for designers, however, in the past, these curves only obtain from the experiments in combination with an analytical approach. Along with the development of finite element method, moment-rotation behaviour can be obtained from numerical method.

Contents

List of Figures

Chapter 2

Chapter 3

Chapter 4

Chapter 5

Chapter 6

Chapter 7

Chapter 8

List of Tables

CHAPTER 1

Introduction

1.1 Background

Steel structural hollow sections, circular, square and rectangular, are some of the most efficient structural sections under compression loading, and are unique in the world of structural steel sections because their geometries are such that their masses are distributed away from their longitudinal axes, making them ideal for use as column. The conventional beam-to-column connections, which are most commonly applied in the world, are diaphragms through the columns at the positions of the beam flanges which are groove-welded to the through diaphragms, while the beam webs are either welded to the column faces or bolted to the columns via shear tabs. Engineers believed that the joints between the beam flanges and columns using Complete Joint Penetration (CJP) groove welded can satisfy the over-strength criteria to allow formation of plastic hinges in beams (European Committee for Standardization, CEN 1994, International Conference of Building Officials, ICBO 1994). However, the Kobe earthquake in Japan (1995) revealed that the conventional types of rectangular hollow section (RHS) column-to-beam connections in building frames were susceptible to brittle fracture under the strong ground motion. In the earthquake, most cracks in RHS column-to I beam connections started with ductile tear, and then changed to brittle fracture at the beam-ends after the connections sustained extensive yielding or local buckling.

The potential for brittle fractures in steel building structures has increased in recent years as a result of the following changes in structural design, as observed by Rolfe and Barsom (1996):

1) Structural engineers and architects are designing more complex structures than in the past.
2) There is an increased use of high-strength, thick, welded steel members, as compared with lower-strength, thinner, riveted or bolted steel members.
3) The choice of construction practices has become increasingly dependent on the minimum cost.
4) More precise methods of computer analyses, which decrease the factor of safety that has been historically incorporated in design, are being used.

After the earthquake, various improvements of connection design were proposed. Improved details to prevent brittle fractures were developed not only under the consideration of material properties, welding details of scallop, tack welding and end tabs, but also the connection forms. One way to achieve the sufficient strength of connections is to reinforce the beam ends by additional members or plates. Another alternative approach is to reduce the cross section of the beam intentionally (weaken the beam section), to produce an intended plastic hinge zone located away from the column face and reduce the stress levels in the vicinity of the complete joint penetration (CJP) flange welds. Researchers hope to develop a new design concept to avoid premature occurrence of brittle fracture.

1.2 The Aim and Objectives of the Present Research

A series of tests was conducted on RHS column-to-beam connections reinforced at the beam ends. The primary purpose of the tests are to find possible solutions for avoiding premature occurrences of brittle fracture so that beam-to-column connections would show a sufficient deformation capacity to meet inelastic demand from earthquakes. After the tests on both conventional and improved connections, it was found that fractures in connections did not occur in the improved connection and a larger energy dissipation capacity was achieved.

However, because of the high costs of experiments, the number of tests is usually limited. Even if the cost is not a main concern, the experiments are generally limited to the variation of a few parameters that have the most effect upon the connection behavior. A partial solution to this problem is to use finite element packages to model additional variations in parameters. In the last decades, the finite element method (FEM) has been developed as a cost-effective and reliable tool and offers more flexibility and possibility to investigate a wider range of parameters than experiments can cover. Thus, the research on beam-to-column connections is further extended using the finite element method.

The aim of this study is to use the finite element method to investigate RHS column-to-I beam connections for avoidance of brittle fracture at the beam ends. After comparing with the experimental results to validate the finite element method, the finite element method can be use to provide reliable analysis of the behavior of connections and develop more new connection types.

For partially restrained column-to-beam connections, the moment-rotation curves

are of great importance for designers, however, in the past, these curves are only obtain from the experiments in combination with an analytical approach. Along with the development of finite element method, the moment-rotation behaviour can be obtained from numerical methods.

The objection of the present research

1. to validate the finite element method with the experimental result
2. to creation the reliable models
3. to develop more new connection types

1.3 The Layout of the Thesis

The thesis starts with a literature review about the research in Chapter 2. Then, a series of experiments which was conducted by the author before this project are reported in Chapter 3. The details include the test set-up, welding procedure, material properties, and loading procedure etc. The experiment and results are also described.

The basic concept of non-linear continuum mechanics is introduced in Chapter 4. The use of the finite element method in solving material and geometric nonlinearity problems is discussed in Chapter 5. These provide the basis of the computational strategy employed in the subsequent chapters.

Chapter 6 is concerned with finite element simulations of a number of test specimens. Four test specimens are simulated numerically and the finite element results are validated against a series of test data described in Chapter 3.

Chapter 7 uses the FEM to simulate more new connection types. As stated in the beginning of this Chapter, by weakening the beam section, connection assemblages are found to show excellent plastic deformation capacity. This approach can be done either by cutting a portion of the beam flange (reduced beam section, RBS) or by reducing the beam web (RBW) connections. Among these methods, the RBS is known to be better. However, this type of connection is relatively costly due to the cutting of flanges at four locations at each end, especially in the presence of floor slabs for rehabilitation purpose. Moreover, in these connections, the cutting of flanges reduces the beam stability and increases the probability of beam lateral torsional buckling. On the other hand, these problems are less severe in the RBW connections where the reductions are made in the beam web. Therefore, the numerical investigation in the present project is concentrated on RBW connections. Although only two configurations of RBW connection are simulated in this Chapter, it provides an alternative way to develop some new design concepts.

Chapter 8 gives the design equations of connections, and Chapter 9 draws some conclusions, and highlights recommendations for future work.

CHAPTER 2

Review

2.1 Brittle Fractures of Steel Moment Connections in the Kobe Earthquake

The 1995 Kobe earthquake took structural engineering professionals by surprise for the fact that many of weld connections in modern steel building frames sustained brittle fracture. Engineers had held a believe for a long time that the joints between the beam flanges and columns using Complete Joint Penetration (CJP) groove welded satisfy the over-strength criteria to allow formation of plastic hinges in beams (CEN 1994, ICBO 1994). The 1995 Kobe earthquake revealed that the conventional types of RHS column-to I beam connections were susceptible to brittle fracture under the strong ground motion. These fractures were concentrated on regions around beam bottom flange groove welds at the beam ends in multi-story moment resisting frames.

2.1.1 Connection Details

The typical detail of beam-to-column connections, which is designed to fulfil requirements for fully restrained moment connections according to the Japanese building code, is shown in Figure 2.1. The connection has through diaphragms at the position of beam flanges. The connection panel is actually a stub-column groove welded to the through diaphragms at the ends. The beam flanges are shop-welded to the diaphragms using single bevel complete penetration groove welds with backup bars, while the beam web is fillet welded to the column flange.

The connection detail for field welding application is similar to Figure 2.1, except that the beam flange are field welded and the beam webs are field bolted. Gas metal arc welding has used both for shop and field welding. Cope holes are prepared in the beam webs for almost all of the connections.

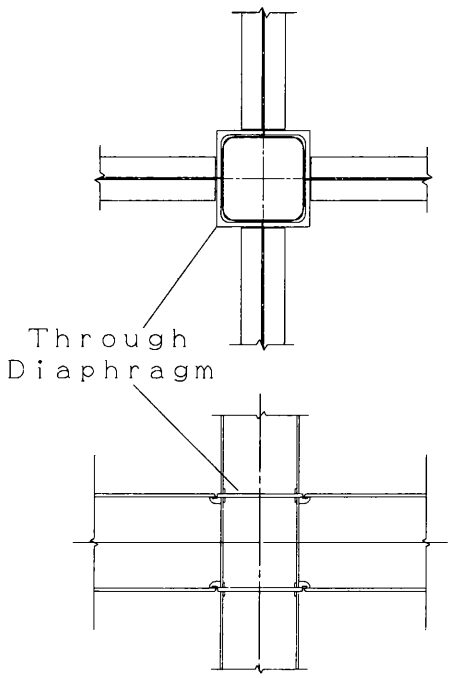

Figure 2.1 Typical shop welded connection

2.1.2 Failure Modes

Three representative fracture paths are illustrated in Figure 2.2. Many of the fractures observed following the earthquake appeared to occur within or initiate from the beam flange groove welds. The majority of fractures occurred at the beam bottom flanges.

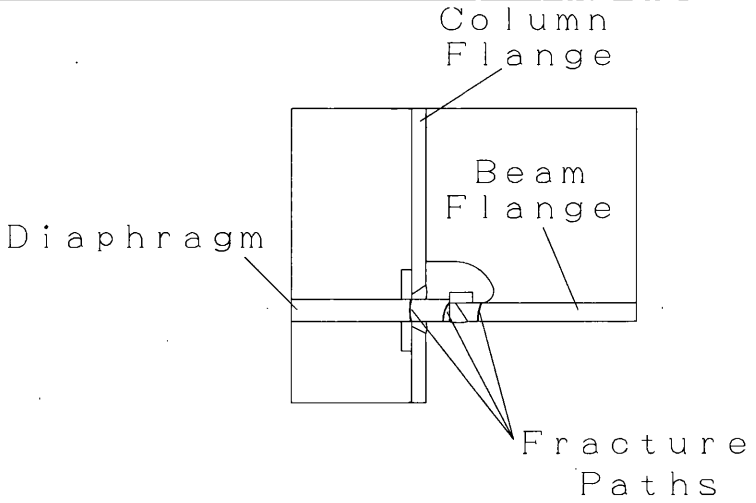

Figure 2.2 Fracture paths

a. Tensile failures started from corners of cope holes. Most of these cracks initiated by ductile tear but changed to brittle fractures as they grew (AIJ Kinki 1995). Figure 2.3 shows one example of these cracks. The crack ran across the full flange section in a brittle manner. The fracture occurred after fully yielding of the flange section.

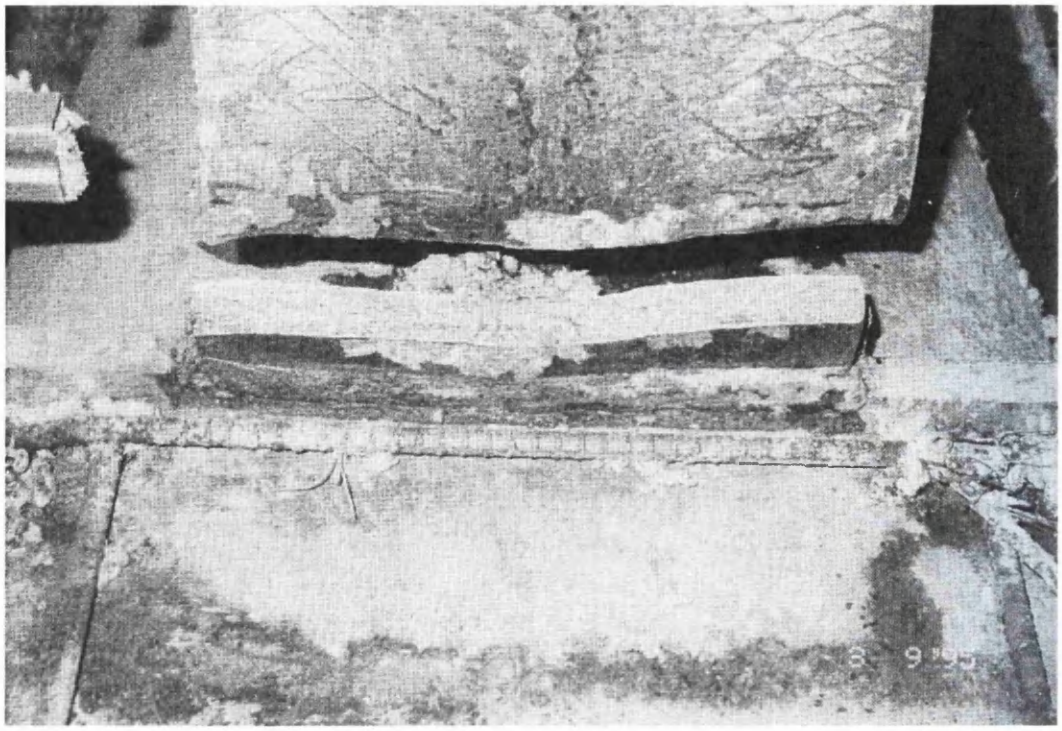

Figure 2.3 Crack initiated at corner of cope hole ran across flange [Inoue 1995]

b. Figure 2.4 shows a crack started from the toes of welds between the beam flange and the diaphragm. A divot of diaphragm material was pulled away from the diaphragm itself. The crack extended in a brittle manner with shear lips after yielding of the beam flange. Cracks frequently emerged from notch roots formed by steel weld tab and beam flanges, and then, ran into the welds and the beam flanges in a brittle manner.

Figure 2.4 Crack begun at weld toe ran through diaphragm [Inoue 1995]

2.1.3 Possible Causes of Brittle Fractures

Causes of tensile failures at beam ends have been studied over the past years, which are summarized below:

a. The Kobe earthquake recorded ground motions significantly stronger than the design spectra specified in the Japanese building code. The input energy due to the Kobe earthquake was approximately 3 times the energy postulated in the code (Akiyama 1997). Therefore, the plastic deformations sustained by members and connections should have been much greater than those postulated at the design stage.

b. The groove welds at the beam ends in large-sized moment connections are under conditions more critical than those prepared for by designers and fabricators before the Kobe earthquake.
c. An abrupt change in contour at the root or at the toes of welds no doubt invites severe stress concentrations. Backup bars and weld tabs create notches at the root of un-fused regions, which also contribute to elevate concentrated stresses.
d. Weld defects are unavoidable in any welded structure.
e. The strain rate effect on material toughness properties is also one of the reasons.

Test results obtained at the University of Texas at Austin (Engelhardt and Sabol 1994) and Lehigh University (Kaufmann and coworkers 1996) demonstrated that the beam flange groove welds were incapable of carrying axial loads in the flanges until plastic hinges formed at the beam ends. Low-toughness weld metal obtained by using the electrodes and by high deposition rate welding rate welding procedures appears to have played an important role inducing brittle fractures.

In 1995, Engelhardt and Sabol (Engelhardt and Sabol 1995) proposed that improved performance of moment connections may not be achieved solely by improving weld quality. This is because the lack of flexural capacity in the bolted web connections leads to overstress of the beam flange and the flange groove welds. They performed a simplified analysis of a beam, with the assumption that the web connection does not transfer moment and that the beam must attain a bending moment of $1.2M_p$ to develop large plastic rotations.

2.2 Research of Moment Connection Behaviour with Conventional and Improved Details – Experimental Aspect

2.2.1 Post-earthquake Research

A large-scale research project was started a few months after the Kobe earthquake (AIJ Kinki 1997). The primary purpose of the project was to find viable improved detail of connections so that beam-to-column assemblies would show a sufficient deformation capacity to meet severe inelastic demand from future earthquakes. The improvements in details, however, were proposed to be achievable by ordinary fabricators with only minor changes in their equipment and resources. More thorough research in connection design to seek long term solutions for preventing brittle fractures in connections was outside the scope of the project. Beam-to-column connections selected for the research were RHS column and wide flange beams, with the through diaphragms at the positions of beam flanges, because these connections were most commonly used in Japan.

A series of cyclic loading test was performed on beam-to-column assemblies using 86 specimens. Variables incorporated in these tests include:

I. Main variables:

1) Connections designed for shop and field welding applications
2) Dimensions and material properties of beams
3) Conventional and improved profiles of beam copes
4) Thickness of through diaphragms
5) Steel weld tab and flux weld tab

II. Supplementary variables:

1) Stringer beads and weave beads
2) Static loading and dynamic loading
3) Test temperatures, room temperature and cryogenic temperature

For each of selected combinations of the main variables, 4 duplicate specimens were fabricated by two different fabricators and tested at two different institutions.

Test results were rather surprising because they showed that brittle fractures could not be prevented, if steel buildings were subjected to strong ground motion like the Kobe earthquake. The cumulative plastic deformation factor η (as defined in Appendix 2), which are listed in table 2.1, represents the plastic deformation capacity under cyclic loading conditions.

Table 2.1 Investigation results of post-Kobe earthquake

Welding	η	n
shop welding	50.8	70
field welding	48.3	16

Note: η denotes the cumulative plastic deformation factor, and n denotes the number of specimens.

Thus, it will be limited in terms of improving the plastic deformation requirement of the connection if only some dimensional changes are made. Therefore, other new design concepts were further considered, including in reinforcing the beam ends by additional members or plate or reducing the cross

section of the beam intentionally to produce an intended plastic hinge zone located away from the column face,

2.2.2 New Connections

In 1998, Kurobane et al. (Kumamoto University, Japan) developed a new type of connections with the beams being connected to the through diaphragm plates by bolts (see Figure 2.5). These new connections belong to one of the alternative approaches to the conventional connections that have welded joints at critical sections at the beam ends. The through diaphragms are extended sufficiently long to accommodate bolted beam splices used as field connections. The thickness of the through diaphragms can be chosen to be greater than the thickness of the beam flanges so that the weakest sections move from the beam sections adjacent to the column faces to the beam splices. The performance of new connections is largely governed by the performance of beam splices in cyclic loading.

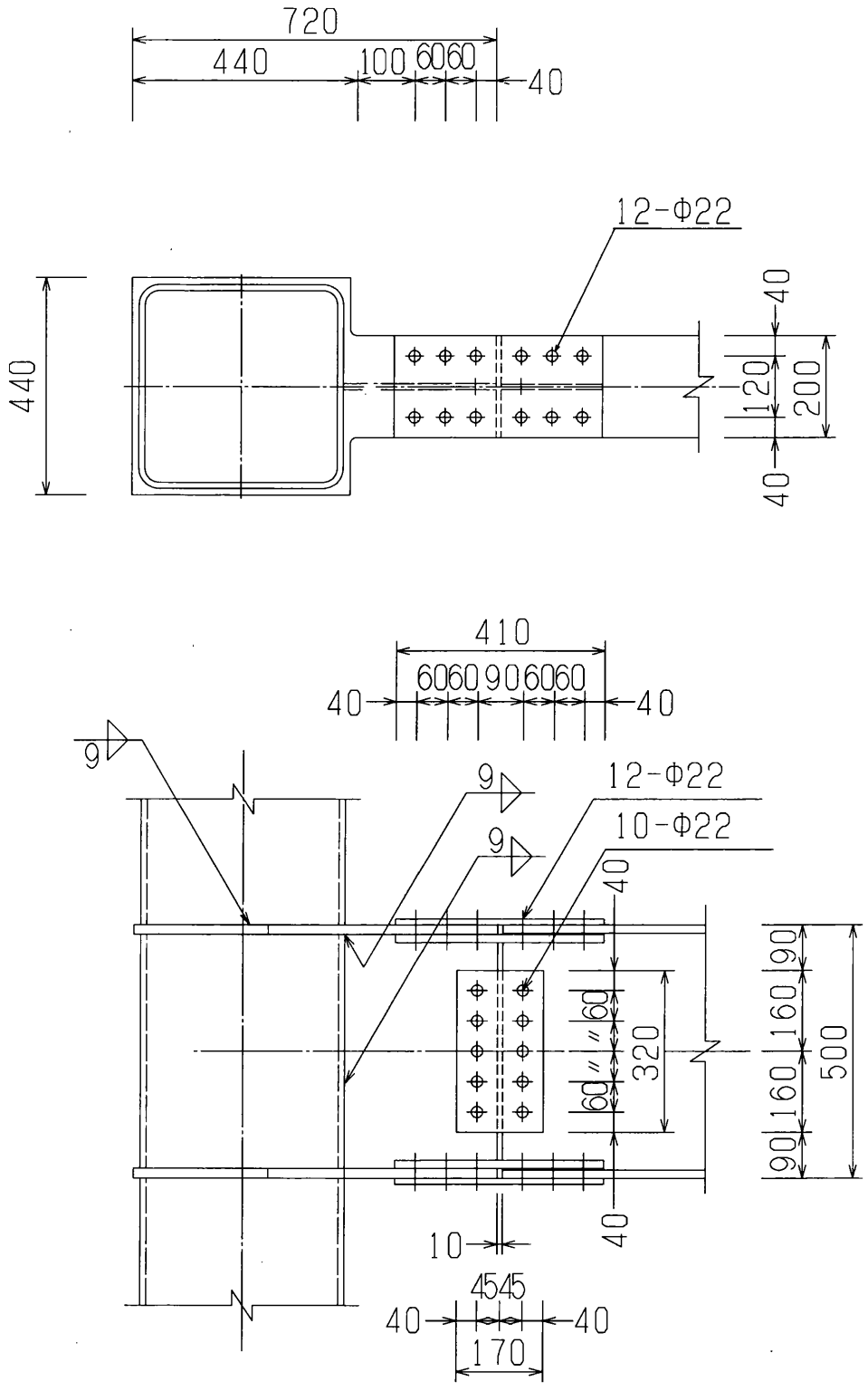

Figure 2.5 New bolted connection

A series of tests was conducted, and Figure 2.6 shows examples of the moment vs. rotation hysteretic curves, in which a new connection is compared with a conventional connection. Both the new and conventional connections use the same beam and column section.

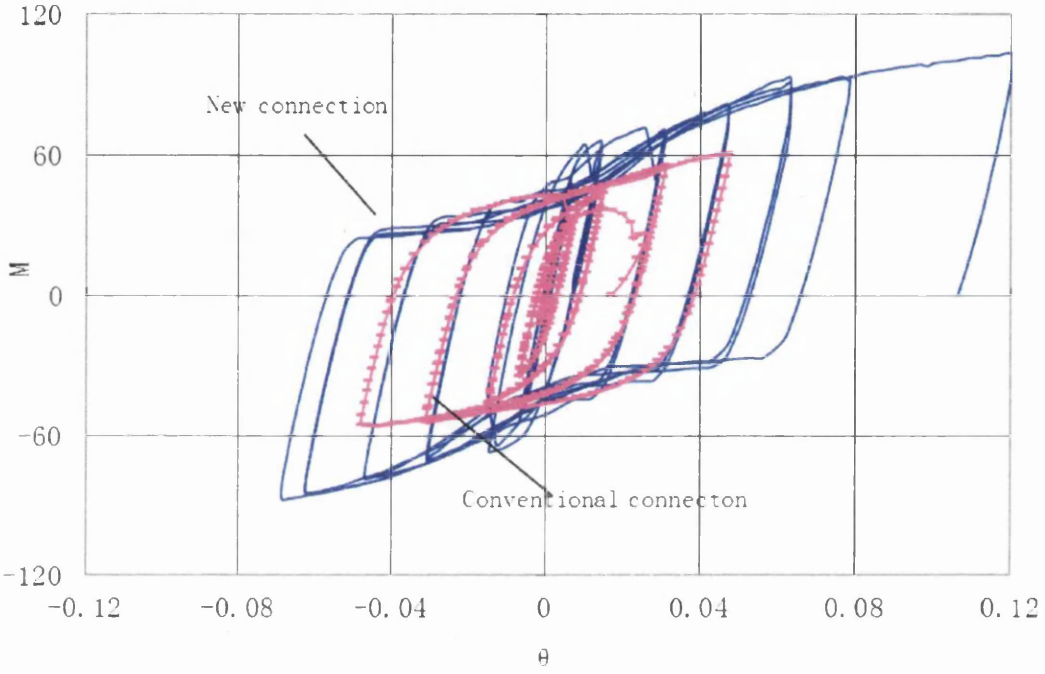

Figure 2.6 Moment vs. rotation hysteretic curves

The conventional connection sustained cracks along the toes of welds at the outer edges of the beam flange (one crack initiated on the side of the beam flange and the other crack initiated on the side of the through diaphragm). The two cracks extended in a ductile manner and led to a separation of the beam flange from the

connection. The cumulative plastic deformation factor η reached 56 (see Figure 2.7)

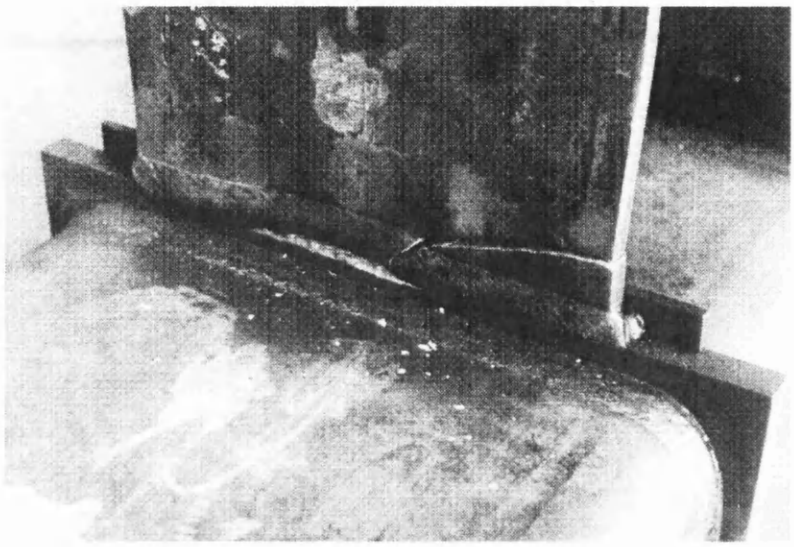

Figure 2.7 Failure mode of conventional connection [Kurobane 1998]

The new connections sustained the combined tensile yielding and local buckling of the beam flanges and web adjacent to the beam splice, of the splice plates and of the flanges and the web of the stub beam connected to the column (see Figure 2.8). One of the beam flange sustained necking and was about to tear off at the final stage. Four major slips at the bolted beam splice occurred during the first 2 cycles. The cumulative plastic deformation factor η reached 158.

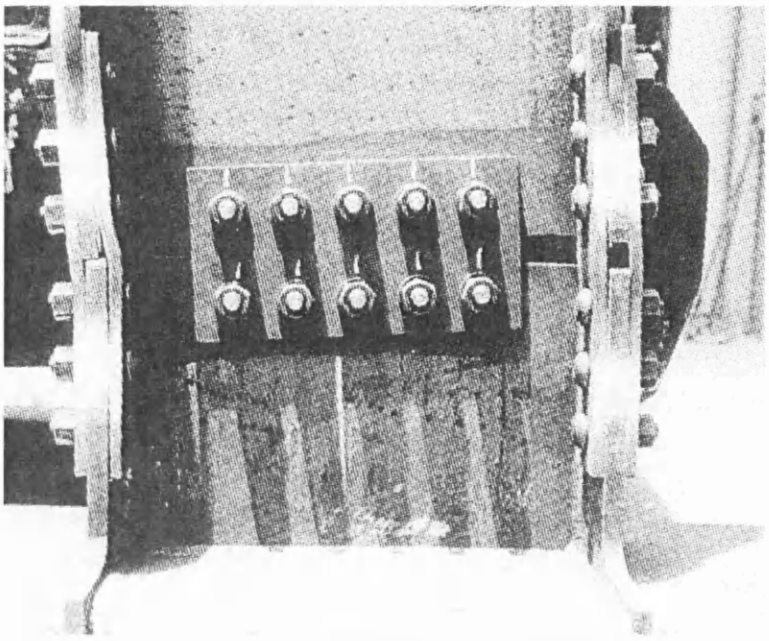

Figure 2.8 Failure mode of new bolted connection [Kurobane 1998]

Advantages of these new connections over conventional connections are not only in a greater energy absorbing capacity (see Figure 2.9) but also in the fact that brittle fracture can be avoided by using sufficiently tough material for the beam. The beam flanges at bolted connections sustained plastic deformation largely in plain stress state, suggesting the flanges would fail by plastic instability rather than by brittle fracture.

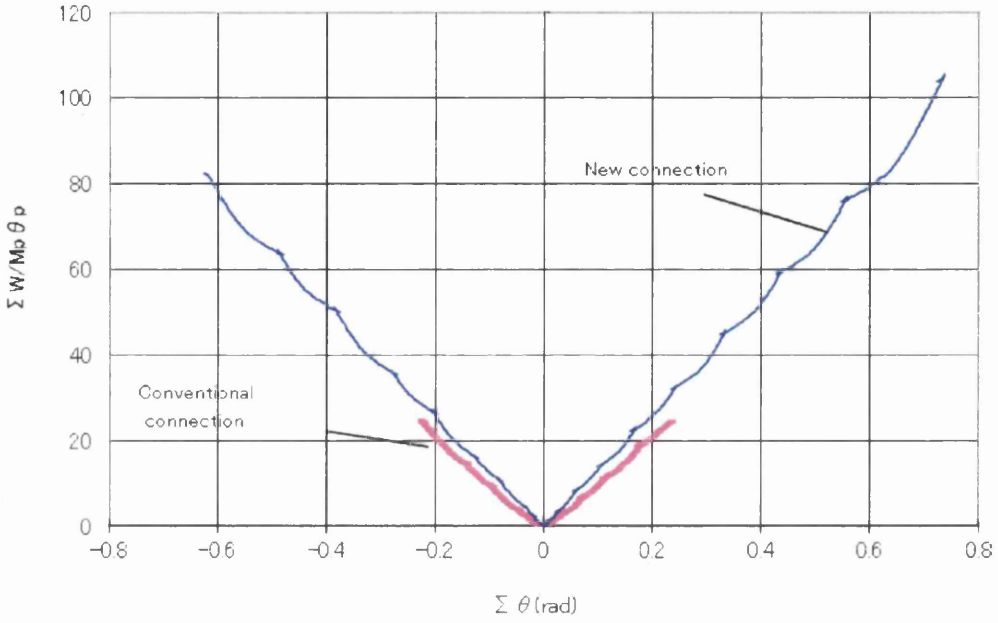

Figure 2.9 Cumulative plastic deformation factor based on dissipated energies

In 1999, Kurobane (Kumamoto University, Japan) proposed ways to strengthen a beam-to-column joint with horizontal haunches based on the extensive series of tests. Kurobane et al. used welded built-up beam sections in which each of the beam flanges with horizontal haunches were cut from a single piece of plate. The joints can be fabricated by welding trapezoidal rib plates to flanges of rolled wide flange section beam. Test results using these joints were found successful in demonstrating sufficient rotation capacity.

Based on the previous works, the Author (Wu 1999) conducted a series of tests on RHS column-to-I beam specimens under cyclic loading. The specimens included both welded and bolted connections, similar to the connections tested by

Kurobane et al. (kurobane 1998) The connection detail is to use the through-diaphragm in which a cut is prepared along the edge of the through- diaphragm so that the beam flange fits into the cut, creating a welded joint of rabbet ([or] -shape) to reinforce the beam end strength (See Figures 2.10 and 2.11). After performing a series of tests on both conventional and improved connections, it was found that fractures in connections did not occur in the improved connection and larger energy dissipation capacity was performed than the conventional types. More details about this work are described in the next Chapter.

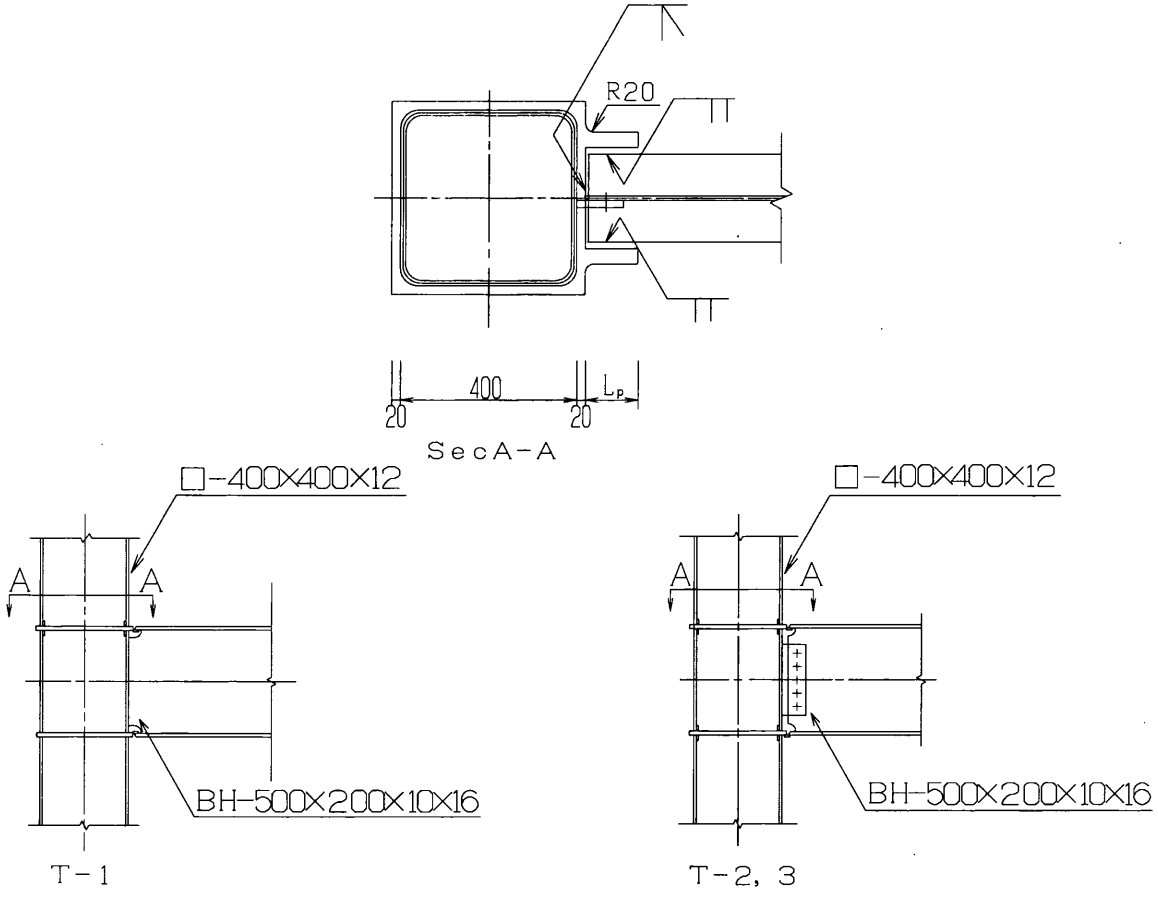

Figure 2.10 New connection of improved type (1)

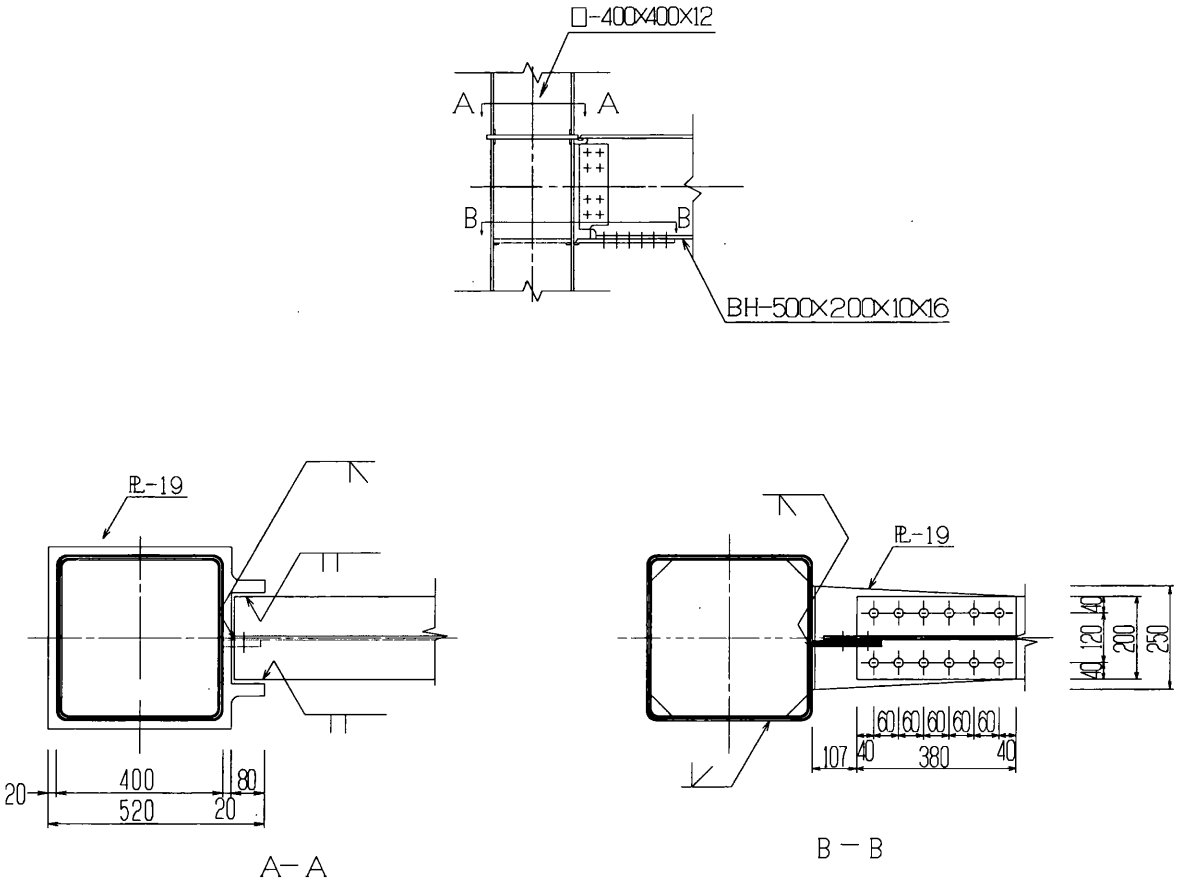

Figure 2.11 New connection of improved type (2)

2.3 Numerical Simulations on Bolted Connections - Numerical Modelling Aspect

As the current project concerns modelling the behaviours of RHS column-to-I beam connections, the creation of a reliable finite element model is a primary aim. Steel beam-to-column connections normally use welded and bolted. Because a bolted connection consists of complex interaction between various entities, it is more complicated than welded connection in finite element modelling. Some existing numerical simulation work on bolted connections is reviewed first.

Bolted end-plate connections have been widely applied in steel structures, because of the simplicity and economy of their fabrication and assembly. Figure 2.12 shows an example of a bolted end-plate connection. Because of limitation in computational capabilities, both in term of software and hardware, the first attempts of simulating bolted connection only involved two-dimensional (2D) models.

Krishnamurthy (Krishnamurthy, N and Graddy, D.E 1976) can be considered as one of pioneers in the field of finite element simulations in bolted connections. He reported several publications in 1970's. Because 3D FE models were computationally expensive, Krishnamurthy and Graddy (Krishnamurthy, N and Graddy, D.E 1976) analysed a benchmark connection by 2D and 3D models. The correlation between these results was the use for the prediction of other 3D models based on the results of corresponding 2D models.

Sherbourne and Bahaari (Sherbourne, A.N and Bahaari, M.R 1994) presented an analytical method based on finite element modelling to study the moment-rotation relationship for a steel bolted connection. The shell element approach has been used to model beams, columns and endplates. The finite element code ANSYS was used for the equivalent 3D analysis. The contributions of various connections, like bolts, endplate and column flanges on the flexibility of the connection was identified.

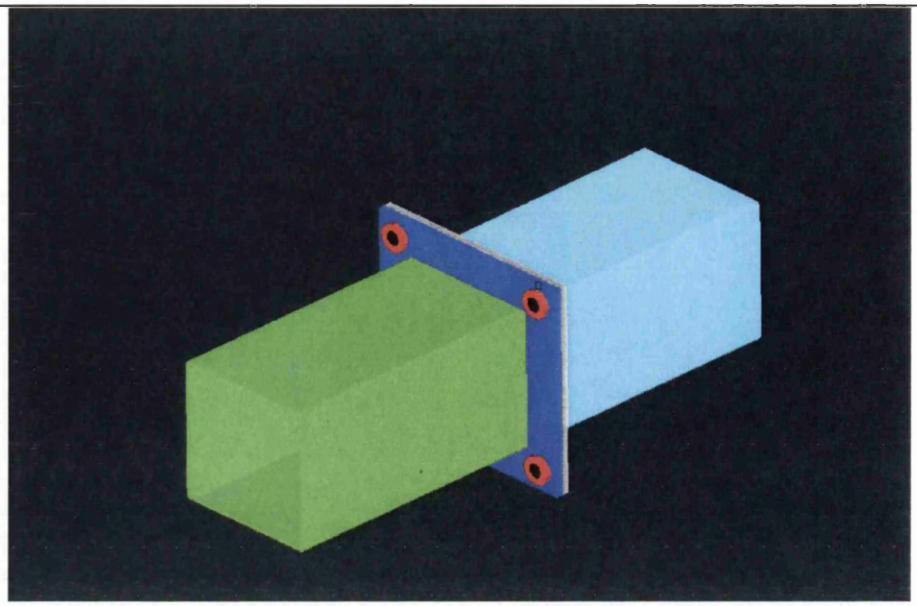

Figure 2.12 An example of a bolted end-plate connection [Wheeler et al 1997]

As computers became more powerful during the last two decades, a steady increase in the size of the finite element models became possible. This made the analyses of less simplified and more realistic. In 1996, Choi and Chung (Choi, C.K and Chung, G.T 1996) performed a finite element analysis for models, including the bolts and completely based on solid elements. Because bolted connections consist of various components with complex interaction between the various entities, it is understood that a more accurate description of the geometry of the components requires a more complex solution procedure. The authors highlighted the iterative character of the solution strategy to describe these highly non-linear processes, both in term of material behaviour and geometric response.

Not only enhanced the capacity of the hardware, but also the capabilities of the software improved, New solution techniques were derived, making numerical analyses much more efficient in terms of computational time, The introduction of

sophisticated contact algorithms further widened the application of numerical methods. "Contact" in its simplest form can be described by the use of so-called "gap elements" which impose displacement compatibility between user-defined pairs of nodes. However, such elements can only be used when friction can be ignored. In addition, modelling of such elements is a tedious and time-consuming task. To overcome these problems, commercial finite element packages developed more user-snug options, such as contact between surface and interface element instead of the node-to-node contact definition required by gap elements. The improved contact algorithms also enabled the modelling of shear and friction between the contacting surfaces.

In 1997, Bursi and Jaspart (Bursi, O.S and Jaspart, J.P 1997) presented their numerical results on isolated bolted tee-stub connections. Unlike most of the previous studies, the bolt head and the flange plate were now modelled as individual components and no longer connected through common nodes, enabling the relative movement between these components. The work used the finite element method and the ABAQUS finite element code to analyse four-bolt un-stiffened extended moment endplate connections under static loading. The purpose of the study was to examine the stiffness and strength behaviour of these connections. The results obtained from the finite element analyses were evaluated by comparing with those obtained from an experimental study. Endplate rotation and bolt forces were both considered. It was intended to show the feasibility of using the finite element method via commercial codes to determine moment-rotation characteristics of semi-rigid connections. The finite element model considered by the authors was quite complex. The bolt and bolt

head were modelled using beam elements. Both preloaded and non-preloaded bolts were considered. The endplate and beam element were eight-node brick element. Contact elements were used to describe the interaction between the endplate and the rigid column flange. Around the bolt holes, nodes were constrained in the direction perpendicular to the face of the endplate.

The same approach was followed by Wheeler et al. (Wheeler, A.T, Clarke, M.J and Hancock, G.J 2000) who carried out numerical simulations on bolted end-plate connections subjected to pure bending. Figure 2.13 shows one of the configurations analysed. Prior to the finite element simulations of the assembled model, Wheeler et al (Wheeler, A.T, Clarke, M.J and Hancock, G.J 2000) first conducted a series of numerical analyses to determine the most efficient type of element and corresponding mesh density for each of the components (i.e. end-plate, bolts, weld beam section). They recommended the use of eight nodded, hybrid elements with four elements modelled through the thickness of the end plate. The same element type was employed to model the bolts. To avoid the problems associated with rigid body movements, loading of the connection was carried out in five steps, such as pre-tensioning of the bolts, applying moment to the tip of the beam section, etc.

Another example of an experimental programme followed up by a numerical study is the work reported by Willibald et al (Willibald, S, Packer, J.A and Puthli, R.S 2001) who investigated bolted flange-plate connections for square and rectangular hollow sections under pure tension. Except for the element type employed for the bolts, the concept of the finite element models analysed by

Willibald closely followed the approach adopted by Wheeler et al. Unlike Wheeler, Willibald used twenty-nodded, quadratic brick elements to model the bolts.

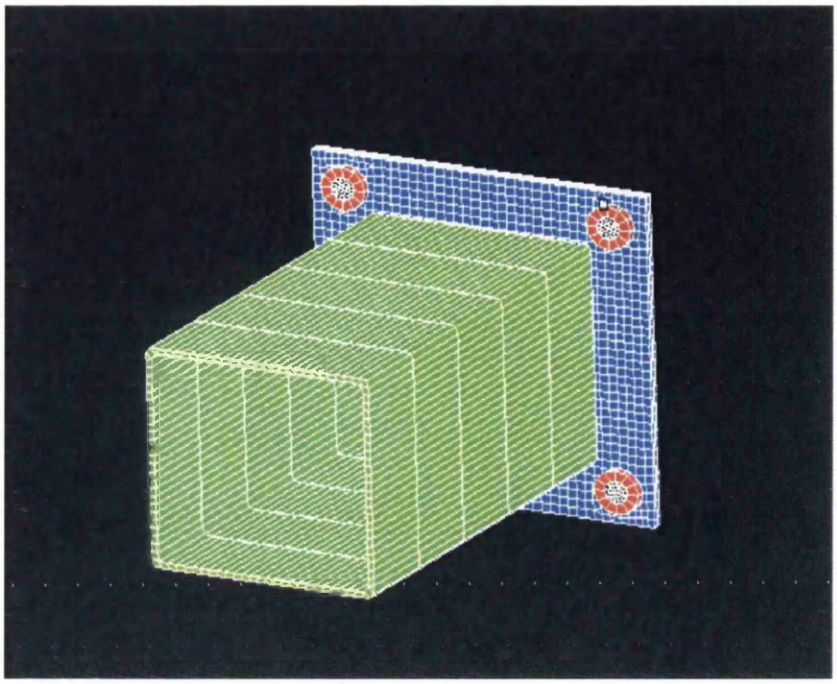

Figure 2.13 An example of FE analysed by Wheeler et al [Wheeler et al 2000]

In end-plate connections, load transfer primarily takes place through axial loading of the bolts. However, when bolted connections are subjected to shear load, the finite element simulations become more complicate, because of the specification of additional contact surfaces. An example of the use of shear bolts, including the difficulties encountered in the finite element analyses, is described by Swanson et al. After having conducted a series of experiments, Swanson et al (Swanson, J.A, Kokan, D.S and Leon, R.T 2000) carried on with finite element simulations on bolted T-stub connections. The configuration, illustrated in Figure 2.14, consists of a T-stub section which was attached to a column flange through tension bolts. Shear bolts were used to connect the beam flange to the T-sub. The finite element mesh, almost exclusively modelled by quadratic, solid elements,

contained approximately 7300 elements, resulting in 53000 degrees of freedom. The convergence problems caused by rigid body motions, had to be overcome by assuming artificial boundary conditions on the T-stub section.

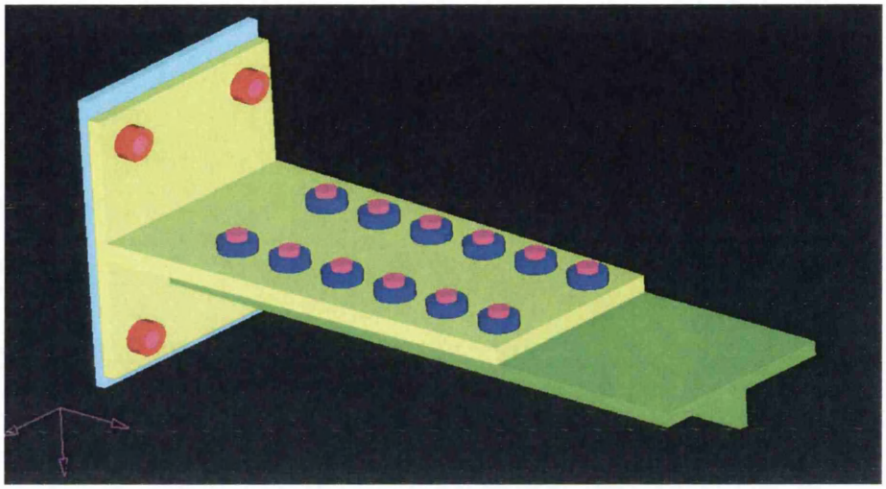

Figure 2.14 T-stub connections study by Swanson et al [Swanson et al 2000]

CHAPTER 3

Experiments and Results

In order to find possible solutions for avoiding premature occurrences of brittle fracture in RHS column-to-I beam connections, a series of tests was conducted by the author in 1999 (Wu 1999). The specimens tested included both welded and bolted connections. Test results show that the improved connection does not fail by fracture as observed in the convention types and has a larger energy dissipation capacity than the conventional types. By comparing with the experimental results to validate the finite element method, we can create reliable finite element models to study and develop more new connection types. For the convenience of the FE validation and reference, the experiments and the relevant results are presented in this Chapter.

3.1 Building Code

The existing seismic codes, such as the Japan building code (Building Centre of Japan BCJ 1997), Eurocode 3 (CEN 1994) and ICBO 1994, require that beam-to-column connections in special moment resisting frames be strong enough to ensure formations of plastic hinges preferably at the beam ends. The following over-strength criterion is recommended for connection design in BCJ 1997, CEN 1994:

$$M_{f.Rd} \geq \alpha M_p \tag{3.1}$$

in which $M_{f.Rd}$ and M_p denote the flexural resistance of the connection at the column face and full-plastic moment of the beam, respectively; α is the over-strength factor. The value of α specified in the Architectural institute of Japan (AIJ) Recommendation (1997) varies with the material to be used and is typically between 1.25 and 1.4 (average 1.3). Eurocode 3 recommends the over-strength factor of

$$\alpha = 1.2\gamma_{Mw} / \gamma_{Mo} = 1.36 \text{ or greater} \tag{3.2}$$

3.2 Specimen Design

In order to compare the test results, specimens were made in two types: T-1 and T-2, 3 and 4 (see Figures 3.2, 3.3, 3.4 and 3.5). T-1 is a conventional connection type, with $_{END}M_u \geq 1.3M_p$, where $_{END}M_u$ is the ultimate flexural capacity of the specimen and M_p is the full plastic moment of the beam; T-2, 3 and 4 are the improved types, with $_{END}M_u = \alpha\ (_fM_{u,} + _wM_p)$, where $_fM_u$ is the ultimate moment of the beam flange and $_wM_p$ is the plastic moment of the beam web, and

$$\alpha = \frac{L_p + L_h + L_t}{L_h + L_t} \tag{3.3}$$

Where the lengths L_h, L_p and L_t are shown in Fig.3.1. Note that the L_p in T-3 is 65mm longer than T-1 and T-4, 40mm longer than in T-2 in order to compare deformation capacity.

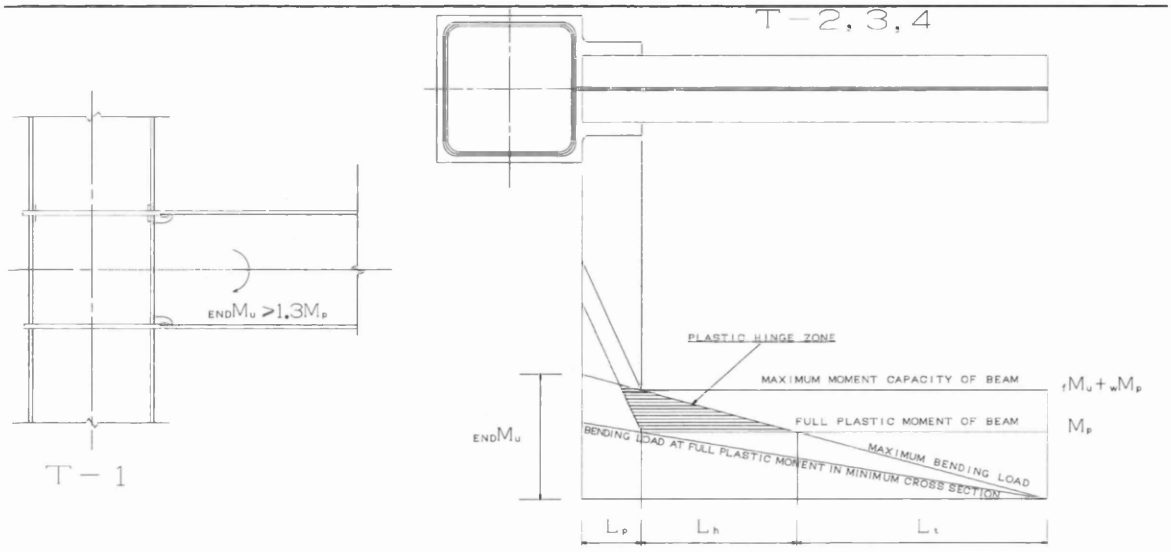

Figure 3.1 Specimen design

3.3 Specimen Details

Full size beam-to-column connections were tested to failure under cyclic loads. All the specimens were one-sided connections, each having a wide flange beam with the nominal dimensions (in mm) of 500×200×10×16 welded to a cold-formed square hollow section column with the nominal dimensions of 400×400×12. All the specimens had through diaphragms at the positions of the beam flanges to transmit axial forces in the flanges to the columns. The diaphragms were cut from a single piece of plate in which a cut was prepared along the edge of through diaphragm so that the beam flange fit into the cut, creating a welded joint of rabbet ([-shape) to reinforce the beam end strength. In specimen T-2 and T-3, both beam flanges were welded to the through diaphragm plates while the beam web was bolted to the fin plate by a single row of five bolts. In specimen T-1, the beam web was welded to the column flange, and both beam flanges were welded to the through diaphragm plates. T-4 had through diaphragms at the beam top flanges and internal diaphragms at the beam bottom flanges while the beam web

was bolted to the shear tab by a double row of four bolts. At the position of internal diaphragm, a flange plate with bolt holes was butt-welded, which was connected to the beam bottom flange by the single-shear high-strength bolted joint. All the specimens at the beam end used complete joint penetration groove welds. Configurations of specimens are shown in Figures 3.2, 3.3, 3.4 and 3.5.

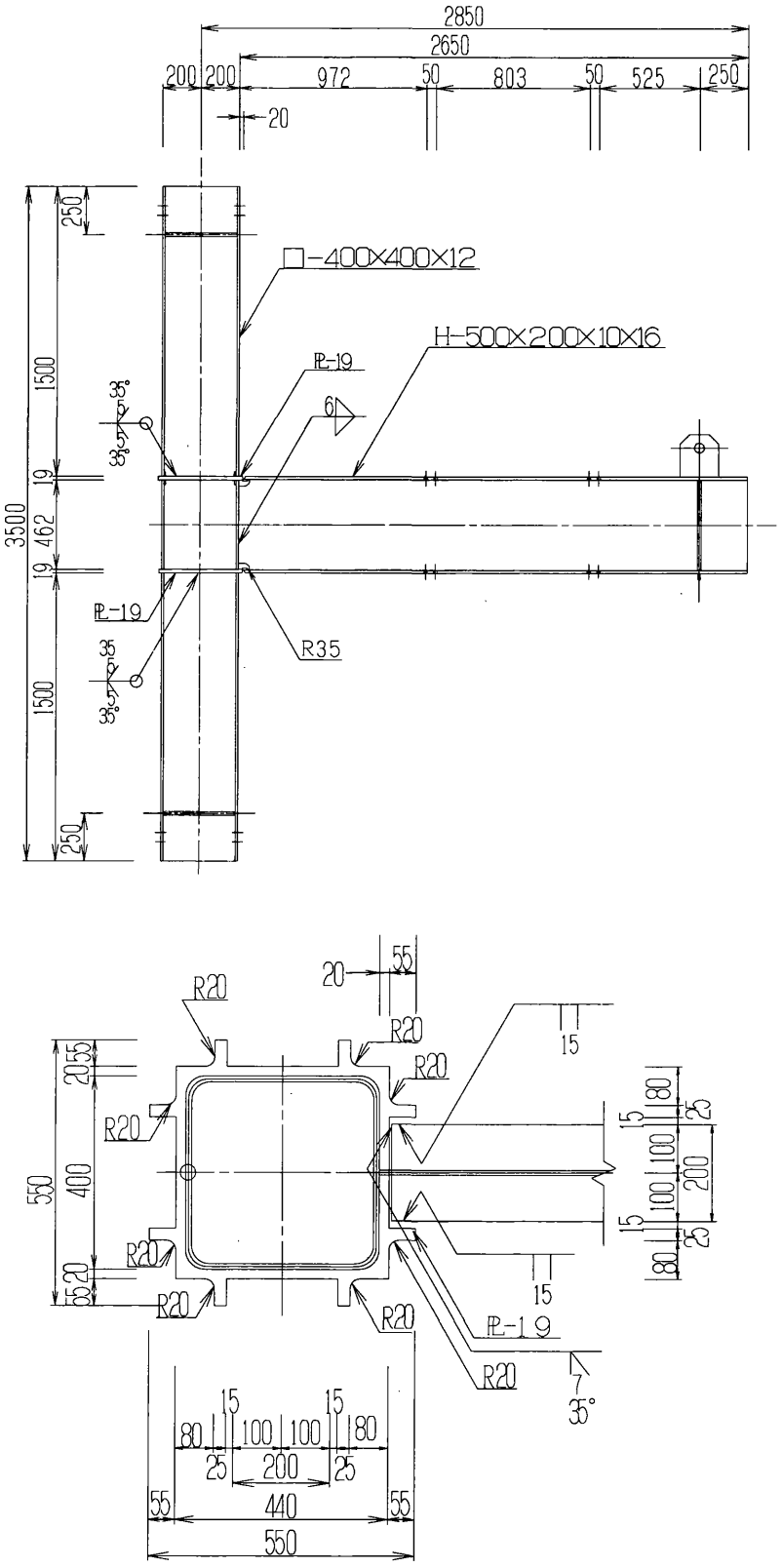

Figure 3.2 Detail of connection T-1

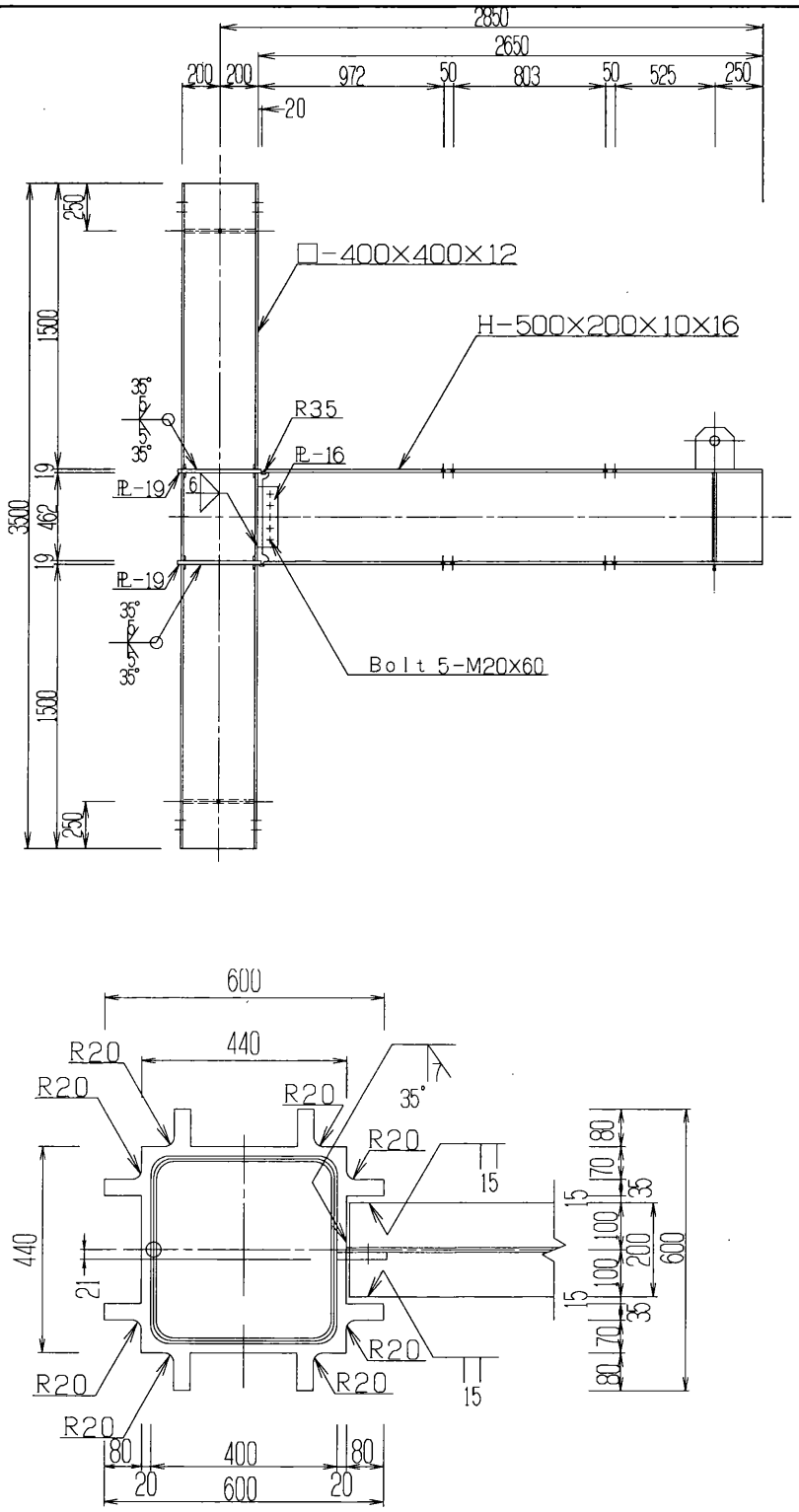

Figure 3.3 Detail of connection T-2

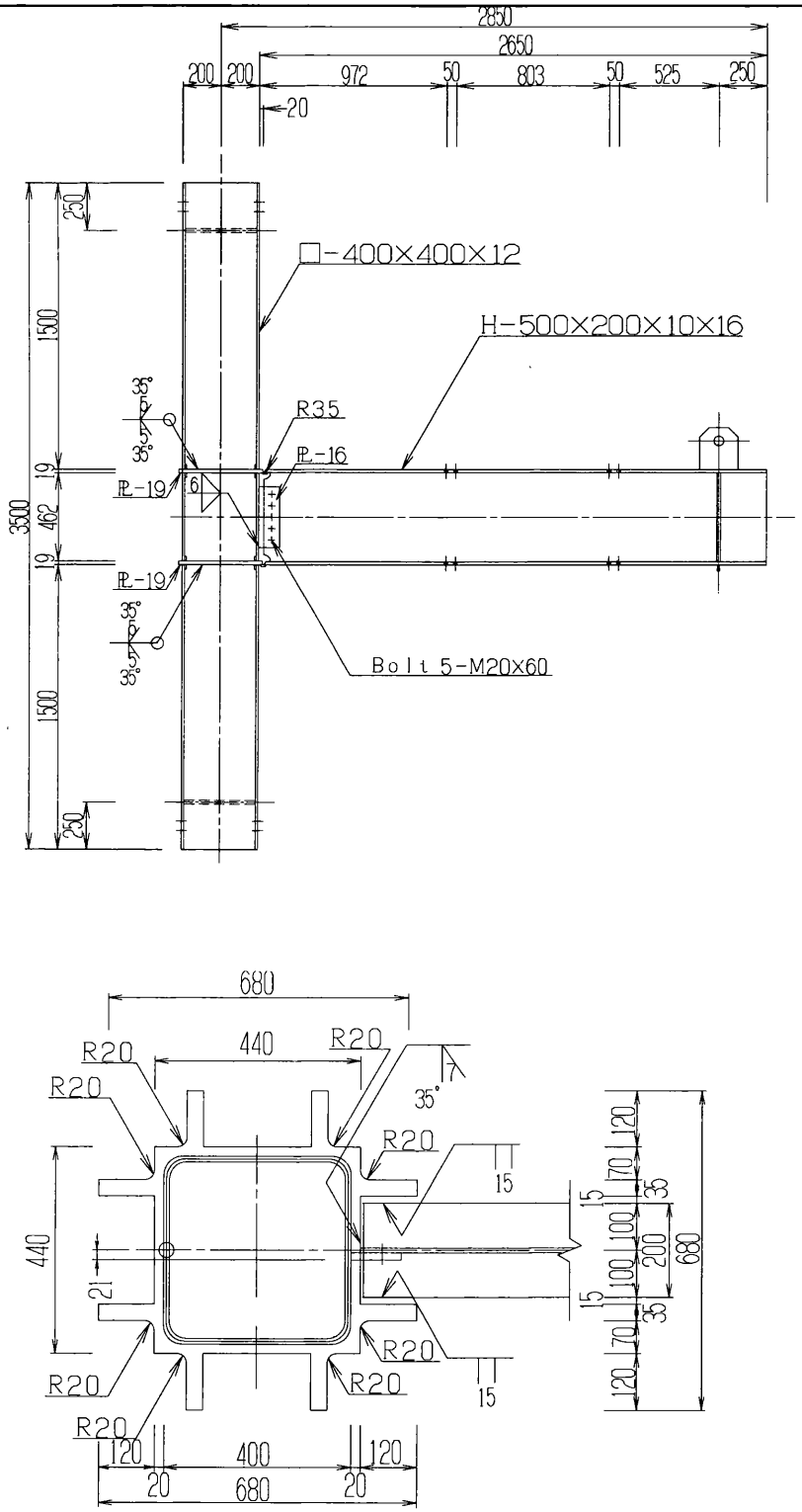

Figure 3.4 Detail of connection T-3

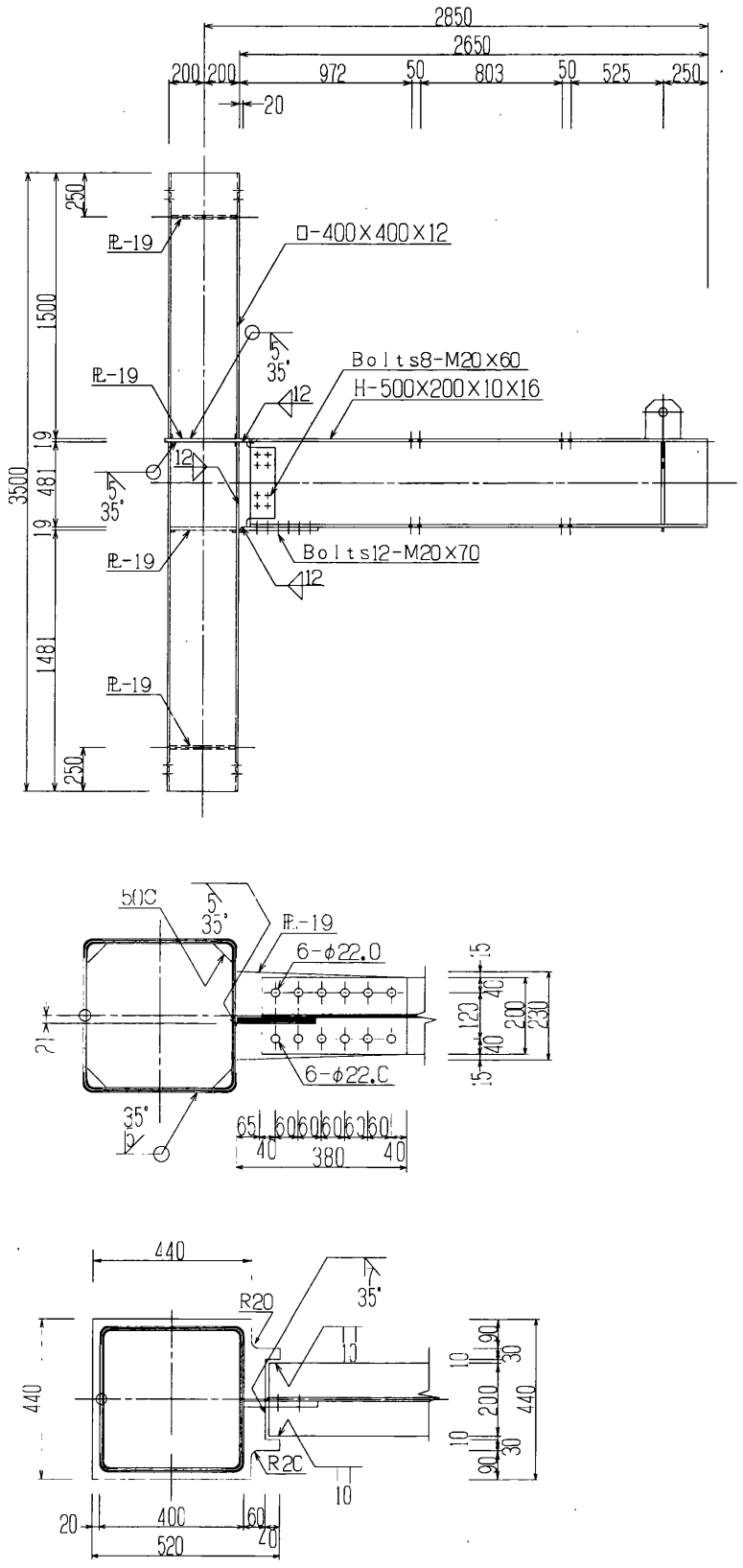

Figure 3.5 Detail of connection T-4

3.4 Material Properties

All the tensile coupon tests were taken from one section of the beam and column. The details are shown in Appendix 1. Mechanical properties of materials are summarized in Table 3.1. All the materials were of weld-able low-carbon steel specified as Japan industrial standard (JIS) SS400 and STKR400, roughly equivalent to US ASTM A36 and A501 steels.

Table 3.1 Mechanical properties of materials

Location	σ_y N/mm^2	σ_u N/mm^2	E.L %	E kN/mm^2	Y.R	t mm
Beam flange	306	448	23	212	0.68	15.45
Beam web	331	447	25	208	0.74	9.72
Column	338	439	22	202	0.77	11.48
Fin plate16mm	311	467	25	207	0.67	15.96
Diaphragm plate19mm	278	406	29	212	0.69	18.62

Note: σ_y= stress at the yield strength; σ_u= stress at ultimate tensile strength ; E.L.= elongation; E= elastic modulus ; Y.R.= yield ratio (σ_y/σ_u); t=Thickness

3.5 Test Set-up and Load Sequences

All the specimens were configured to form a T-shaped assembly with a single wide flange beam connections. The both ends of the column were fixed to a strong floor, while the cyclic shear load was applied at the end of the beam by a double hydraulic jack. The loading arrangements are shown in Figure 3.6. Lateral bracing systems were provided at two positions of the beam.

Displacement measurements taken were not only the horizontal displacement u_1 at the loading point but also the vertical displacement v_1 and v_2 at the

diaphragms and the horizontal displacement u_2 at the column end. The rotation of the beam θ was calculated by the following equation:

$$\theta = \frac{u_1 - u_2}{L} - \frac{v_2 - v_1}{J_d} \tag{3.4}$$

Where L and J_d denote the distance from the loading point to the column face and the distance between the centroids of the top and bottom beam flanges, respectively.

All the specimens were subjected to slowly applied cyclic loading in the following way: at least 2 cycles of reversed loading in an elastic region and, subsequently, displacement controlled cyclic loading with the amplitude increased as $\pm 2\theta_p$, $\pm 4\theta_p$, $\pm 6\theta_p$, ... up to failure, where θ_p represents the elastic beam rotation when the beam moment at the column face reached the full plastic moment M_p which can be calculated by the following equation:

$$\theta_p = \frac{L}{3EI} M_p + \frac{1}{GA_w} \frac{M_p}{L} \tag{3.5}$$

Two cycles of loading were applied at each displacement increment.

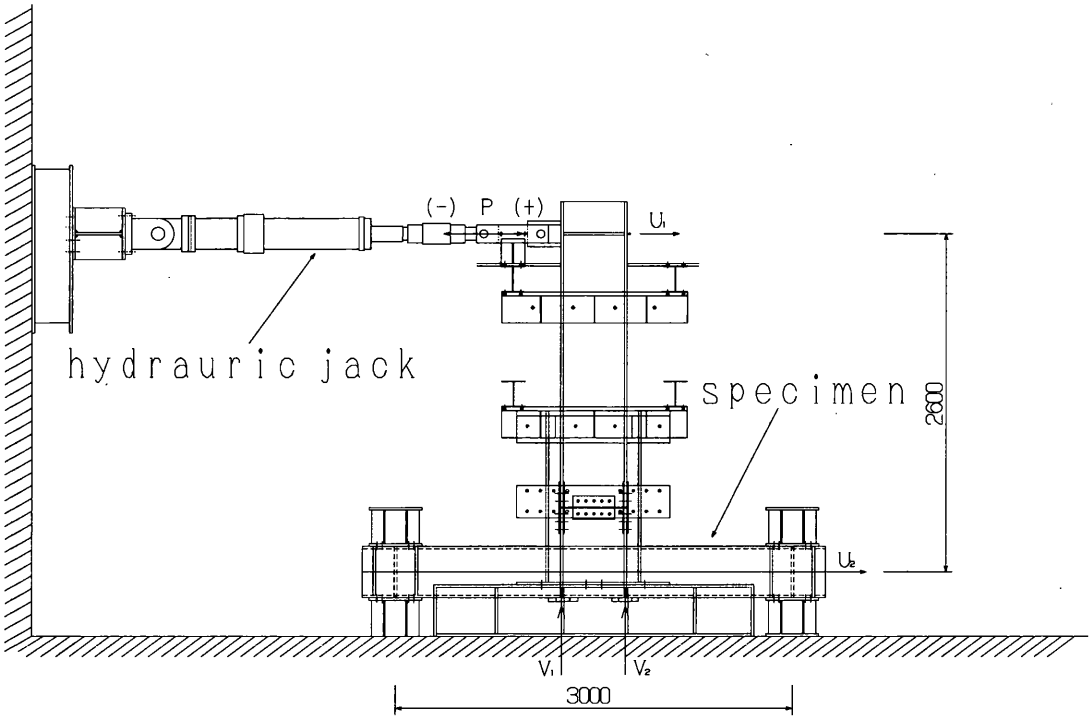

Figure 3.6 Test set-up

Note: u_1, u_2: horizontal displacement

v_1, v_2: vertical displacement

P: load

3.6 Summary of Test Results

Figures 3.7, 3.8, 3.9 and 3.10 show the bending moment vs. beam rotation hysteric curves at the column faces. The moment is the maximum moment at the column face M_m and is non-dimensionalized by the full-plastic moment M_p of the beam. The moment takes positive values when the bottom flange is in tension. θ is determined by equation 3.4.

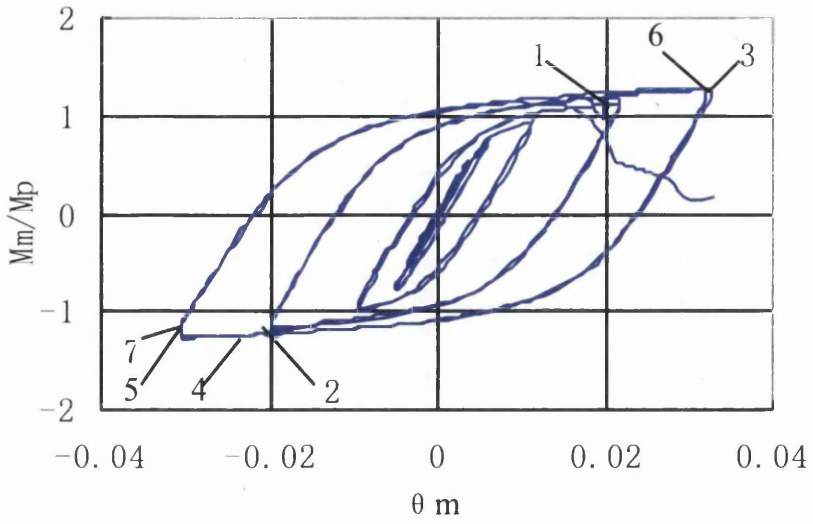

Figure 3.7 the bending moment vs. beam rotation hysteric curves (T-1)

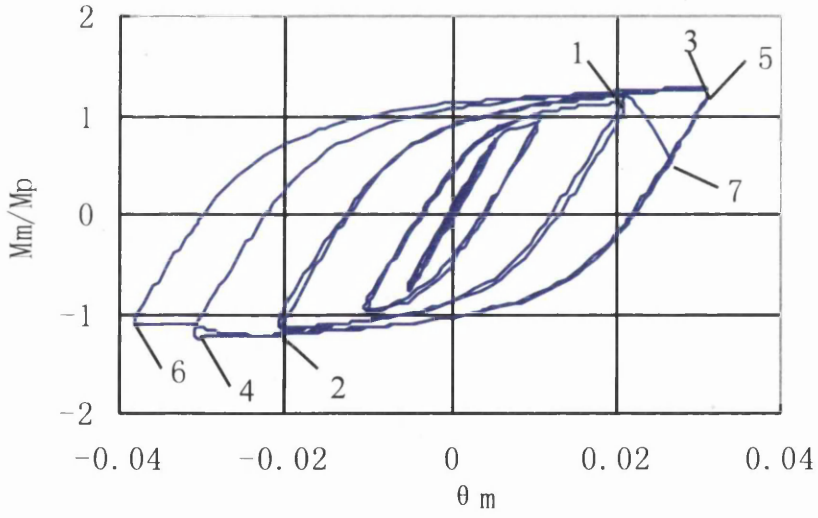

Figure 3.8 the bending moment vs. beam rotation hysteric curves (T-2)

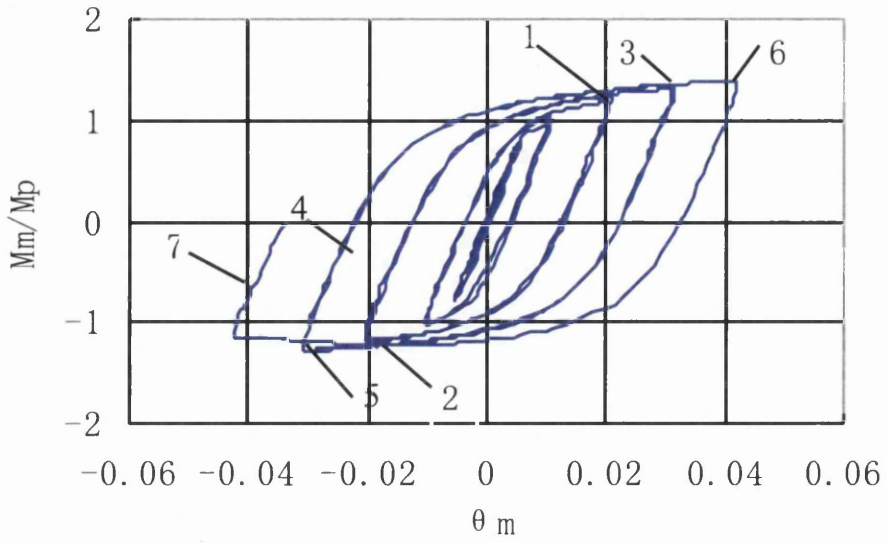

Figure 3.9 the bending moment vs. beam rotation hysteric curves (T-3)

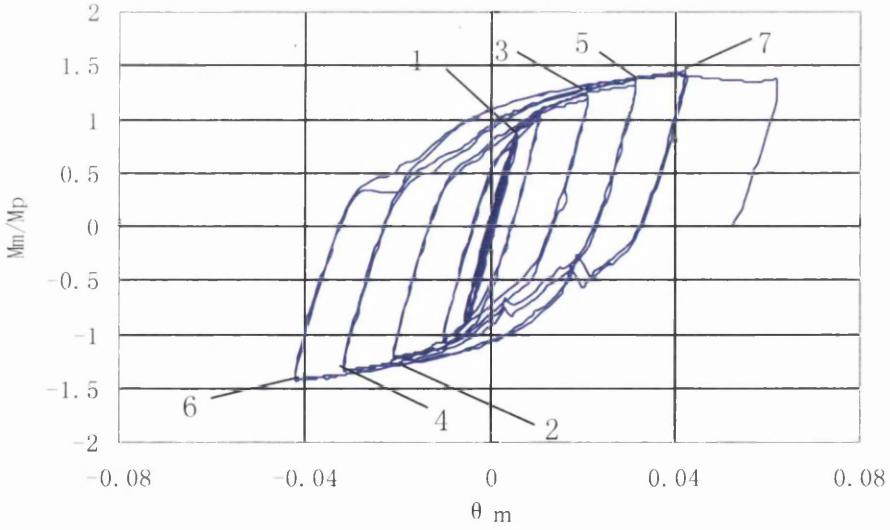

Figure 3.10 the bending moment vs. beam rotation hysteric curves (T-4)

Specimen T-1 showed the following failure sequences:

1. A hair crack was found at the bottom flange.

2. A hair crack was found at the top flange.

3. The crack extended to 2mm at the bottom flange.

4. Bolt slip.

5. The crack extended to 3mm at the top flange

6. The crack extended to 6mm at the bottom flange while a crack was found at the bottom cope.

7. The crack expanded to 6mm at the top flange.

Specimen T-2 showed the following failure sequences.

1. A hair crack was found at the bottom flange.

2. A hair crack was found at the top flange.

3. The crack extended to 2mm at the bottom flange while a crack was found at the bottom of beam cope.

4. The crack extended to 4mm at the top flange while a crack was found at the top of beam cope.

5. The bottom cope crack extended to 1mm. A crack was found at the web.

6. The crack extended to 40 mm at the top flange.

7. The crack extended to 30mm at the bottom flange, which led to bottom cope tear off through.

Specimen T-3 showed the following failure sequences.

1. A crack was found at the bottom flange.

2. A crack was found at the top flange.

3. The crack extended to 2mm at the bottom flange.

4. The top and bottom flanges were buckling.

5. The crack extended to 2mm at the top flange.

6. The crack extended to 4mm at the bottom flange.

7. The web was buckling

Specimen T-4 showed the following failure sequences.

1. Bottom bolts slip (beam flange).

2. A crack was found at the top flange.

3. Bolts slip (beam web).

4. The bottom flange was buckling.

5. The top flange was bucking.

6. The crack extended to 2 mm at the bottom flange.

7. The web was buckling

One of the important failure modes observed in the test was tensile failure of the beam flanges. First, cracks were found either at the tip of the weld toes of horizontal haunches or at the toe of beam copes. Then, these cracks grew gradually with load cycling and were linked together, and finally led to tensile failure of the beam flange in T-1 and T-2 (see Figure 3.11). T-3 and T-4, which was designed to have sufficient tensile capacity at the flange ends, reached the maximum loads only leading to local buckling of the top and bottom flanges and web of the beams (see Figures 3.12 and 3.13). Although the cracks described above were found in this specimen as well, the crack growth was stable.

Figure 3.11 Tensile failure T-1 and 2

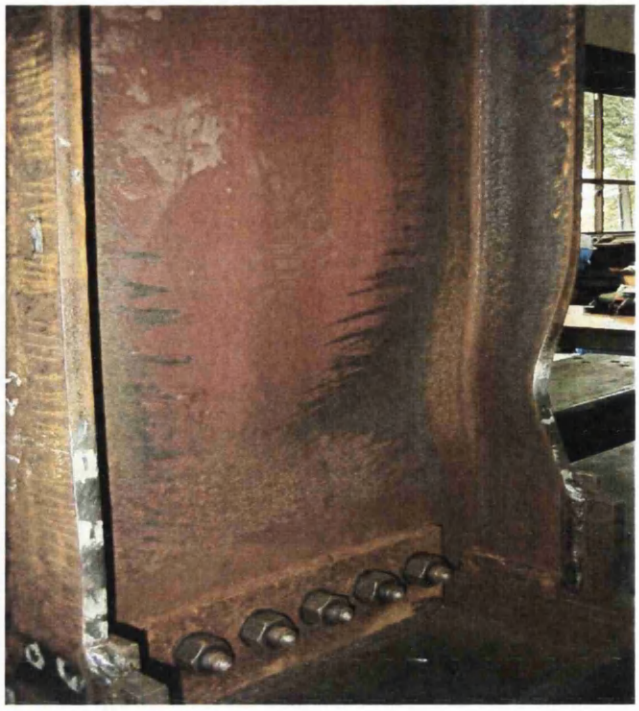

Figure 3.12 Local buckling observed in T-3

Figure 3.13 Local buckling observed in T-4

3.7 Moment-rotation Relationships

Moment-rotation relationships for specimens T-1, T-2, T-3 and T-4 are obtained from so-called skeleton curves (see Figures 3.14, 3.15, 3.16 and 3.17). The skeleton curve is constructed from a hysteretic curved by linking a portion of the curve that exceeds the maximum load in the preceding loading cycle sequentially (see Figure c in Appendix 3)

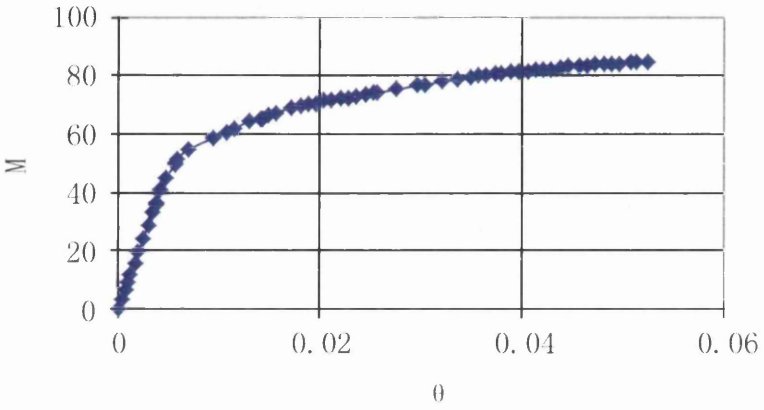

Figure 3.14 T-1 Moment-rotation relationship

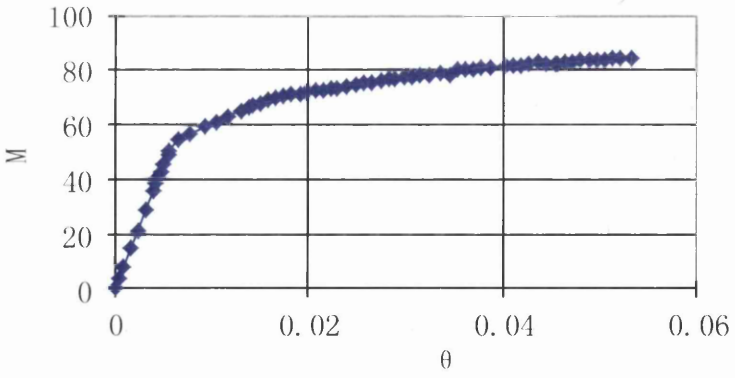

Figure 3.15 T-2 Moment-rotation relationship

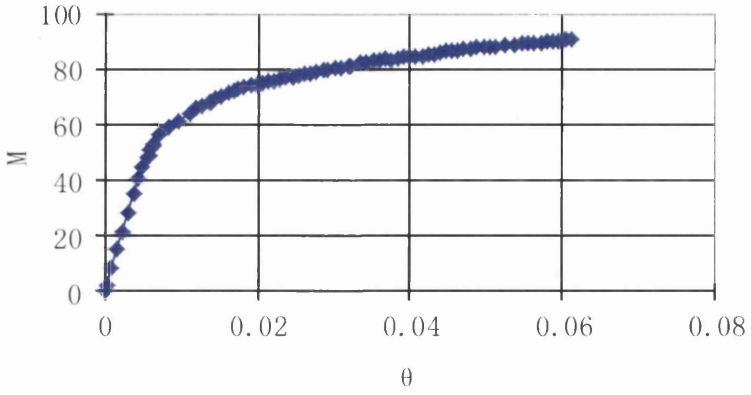

Figure 3.16 T-3 Moment-rotation relationship

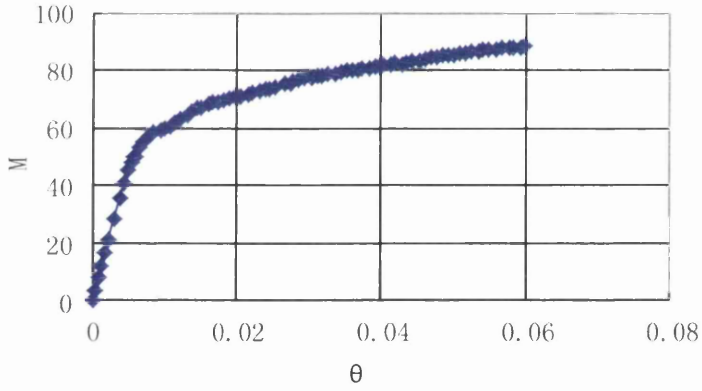

Figure 3.17 T-4 Moment-rotation relationship

The experimental tests have completed in this Chapter, this can now be used test data to validate the finite element method and develop more new connections in the following Chapters.

Chapter 4

Non-linear continuum mechanics

This chapter introduces some basic concepts of continuum mechanics. The definitions and notations introduced will be employed throughout the subsequent finite element simulations. The theory described is taken mainly from Billington and Tate, 1981; Bonet and Wood, 1997; Ciarlet, 1988; Gurtin, 1981; Lemaitre and Chaboche, 1990; Ogden, 1984; Spencer, 1980; Truesdell and Noll, 1965.

There are four types of notation which are used in this Chapter and the following Chapter: indicial notation, tensor notation, matrix notation and voigt notation. To illustrate the various notations, the quadratic form associated with **A** and the strain energy in the four notations are given as follows:

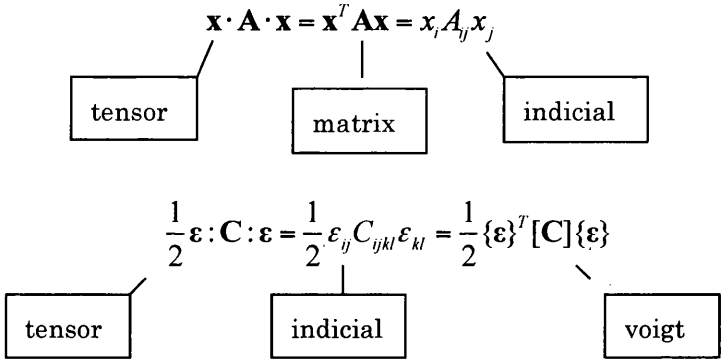

4.1 Kinematics of Deformation

4.1.1 Motion

Figure4.1 shows a general continuum body, **B**, which is arranged in an initial configuration at a time t=0 occupying the domain Ω_0, has changed its position

and shape to the current configuration and occupies the region Ω, after undergoing some motion and deformation.

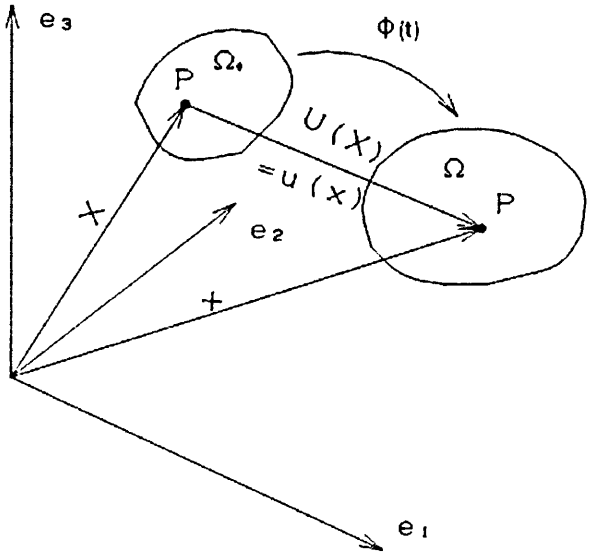

Figure 4.1 General motion of a deformable body

The motion can be mathematically described by a mapping between the initial and current particle positions as follows:

$$\mathbf{x} = \varphi(\mathbf{X}, t) \tag{4.1}$$

where **X** represents a material field and x is a spatial field. The material position of a given particle is its location in the initial configuration. Its spatial position is its location in the current configuration.

4.1.2 Material and Spatial Descriptions

Any field variable associated with the continuum body may be referred either to the initial/material configuration or to the current/spatial configuration. A field variable that is defined as a function of the initial position, **X**, represents a material field. A material field takes $\Omega_0 \times \mathbf{T}$ as its domain, where **T** is the time interval over which the motion is defined. Such a field must be distinguished from a spatial field which is defined on the current position **x** and has $\Omega \times \mathbf{T}$ as its domain. The expression can be given as follows:

$$F = F(\mathbf{X}, t) \tag{4.2}$$

Which is a material field, or

$$f = f(\mathbf{x}, t) \tag{4.3}$$

which is a spatial field.

In equations (4.2) and (4.3), F and f are generic fields which may be scalar, vector or tensor valued.

A material description can be easily obtained from a spatial description by using motion equation as follow:

$$f(\mathbf{x}, t) = f(\varphi(\mathbf{X}, t), t) \tag{4.4}$$

4.1.3 Derivatives

Temporal derivative

Given a field variable F that is defined as a function of the initial position, X, represents a material field. The time derivative of F (**X**,t) is denoted by the operator D (•)/Dt, and the expression can be given as:

$$\dot{F}(\mathbf{X},t) = \frac{DF(\mathbf{X},t)}{Dt} = \frac{\partial F(\mathbf{X},t)}{\partial t} \tag{4.5}$$

This expression measures the change in F associated with a specific particle initially located at **X**, and is known as the material or total time derivative of F. The other type of derivative is known as the spatial or local time derivative. This is the partial derivative with respect to time with the spatial position held fixed. The expression can be given as:

$$\dot{f}(\mathbf{x},t) = \frac{Df(\mathbf{x},t)}{Dt} = \frac{\partial f(\mathbf{x},t)}{\partial t} \tag{4.6}$$

An important example of this derivative is the velocity field. This is the material time derivative of the spatial position:

$$\mathbf{V}(\mathbf{X},t) = \dot{\varphi}(\mathbf{X},t) = \frac{D\varphi(\mathbf{X},t)}{Dt} \tag{4.7}$$

Equation (4.7) is often expressed in the Eulerian form as:

$$\mathbf{v}(\mathbf{x},t) = \mathbf{V}(\varphi(\mathbf{X},t),t) \tag{4.8}$$

Spatial and material gradients

The material and spatial gradients of a field variable F are denoted as $\nabla_0 F(\mathbf{X},t)$ and $\nabla f(\mathbf{x},t)$ respectively. For a material field, the Lagrangian description is used

$$\nabla_0 F(\mathbf{X},t) = GradF(\mathbf{X},t) = \frac{\partial F(\mathbf{X},t)}{\partial \mathbf{X}} \tag{4.9}$$

while for a spatial field, the Eulerian description is used:

$$\nabla f(\mathbf{x},t) = gradf(\mathbf{x},t) = \frac{\partial f(\mathbf{x},t)}{\partial \mathbf{x}} \tag{4.10}$$

Note the capitalisation of the material gradient, 'Grad', to be distinct from the spatial gradient 'grad'.

4.1.4 The Deformation Gradient

A very important variable in finite deformation analyses is the deformation gradient **F**. Consider one material particles A_1 in the neighbourhood of a material particle Q (see Figure 4.2). The position of A_1 relative to Q is given by element vectors $d\mathbf{X}_1$ as follows:

$$d\mathbf{X}_1 = \mathbf{X}_{A_1} - \mathbf{X}_P \tag{4.11}$$

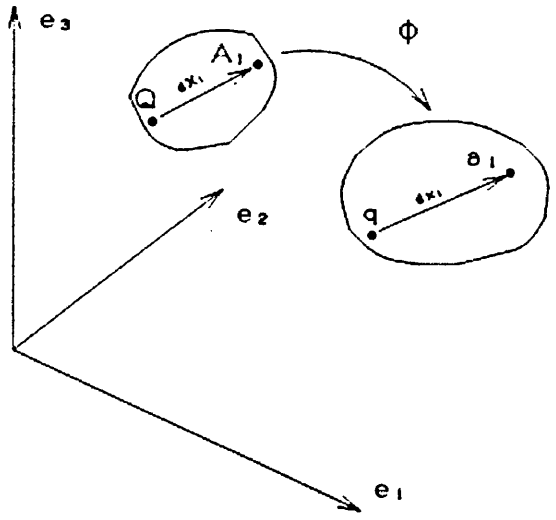

Figure 4.2 Deformation of infinitesimal position vector

After deformation, the material particles P and A_1 have moved to the current spatial positions:

$$\mathbf{x}_q = \varphi(\mathbf{X}_Q, t) \tag{4.12}$$

and

$$\mathbf{x}_{a_1} = \varphi(\mathbf{X}_{A_1}, t) \tag{4.13}$$

The corresponding element vectors become

$$d\mathbf{x}_1 = \mathbf{x}_{a_1} - \mathbf{x}_q = \varphi(\mathbf{X}_Q + d\mathbf{X}_1, t) - \varphi(\mathbf{X}_Q, t) \tag{4.14}$$

Thus, the deformation gradient tensor $\mathbf{F}$ is given as:

$$\mathbf{F}(\mathbf{X}, t) = \frac{\partial \varphi(\mathbf{X}, t)}{\partial \mathbf{X}} = \nabla_0 \varphi(\mathbf{X}, t) \tag{4.15}$$

The element vectors $d\mathbf{x}_1$ can be obtained in terms of $d\mathbf{X}_1$ as:

$$d\mathbf{x}_1 = \mathbf{F} d\mathbf{X}_1 \tag{4.16}$$

4.1.5 Velocity Gradient and Rates of Deformation

The material velocity gradient is defined as $\mathbf{L}$

$$\mathbf{L}(\mathbf{X}, t) = \nabla_0 \mathbf{V}(\mathbf{X}, t) \tag{4.17}$$

where $\mathbf{V}$ is the material expression of velocity.

This can be related to a time derivative of the deformation gradient:

$$\nabla_0 \mathbf{V}(X, t) = \frac{\partial \mathbf{V}(\mathbf{X}, t)}{\partial \mathbf{X}} = \frac{\partial}{\partial \mathbf{X}} \left(\frac{\partial \varphi(\mathbf{X}, t)}{\partial t} \right) = \dot{\mathbf{F}}(\mathbf{X}, t) \tag{4.18}$$

The spatial velocity gradient, which is defined as the spatial gradient of the velocity field, is expressed as $\mathbf{M}$:

$$\mathbf{M}(\mathbf{x}, t) = \nabla \mathbf{v}(\mathbf{x}, t) = \frac{\partial \mathbf{v}(\mathbf{x}, t)}{\partial \mathbf{x}} \tag{4.19}$$

Applying the chain rule, we can obtain an important relation:

$$\mathbf{M} = \nabla \mathbf{v} = \dot{\mathbf{F}}\mathbf{F}^{-1} \tag{4.20}$$

Two further tensor fields are derived from the spatial velocity field. These are the rate of deformation tensor:

$$\mathbf{d} = \frac{1}{2}(\mathbf{M} + \mathbf{M}^T) \tag{4.21}$$

and the spin tensor:

$$\mathbf{w} = \frac{1}{2}(\mathbf{M} - \mathbf{M}^T) \tag{4.22}$$

Clearly, by construction,

$$\mathbf{d} = \mathbf{d}^T \quad \text{and} \quad \mathbf{w} = -\mathbf{w}^T \tag{4.23}$$

and also

$$\mathbf{M} = \mathbf{d} + \mathbf{w} \tag{4.24}$$

Equation (4.22) expresses that **d** and **w** represent the decomposition of **M** into symmetric and anti-symmetric parts respectively.

4.1.6 Change in Volume

Consider the infinitesimal cube dV with edges parallel to the Cartesian axes in Figure4.3. Three edges of the cube are $d\mathbf{X}_1$, $d\mathbf{X}_2$, and $d\mathbf{X}_3$. Its volume is given by the vector triple product of the edge vectors thus:

$$dV = d\mathbf{X}_1 \cdot (d\mathbf{X}_2 \times d\mathbf{X}_3) \tag{4.25}$$

As $d\mathbf{X}_1$, $d\mathbf{X}_2$, $d\mathbf{X}_3$ are mutually orthogonal, this simplifies to:

$$dV = dX_1 dX_2 dX_3 \tag{4.26}$$

where $dX_1 = |\, d\mathbf{X}_1 \,|$

At some given time after deformation, the cube will change shape by the vectors $\mathbf{F}d\mathbf{X}_1$, $\mathbf{F}d\mathbf{X}_2$, and $\mathbf{F}d\mathbf{X}_3$. The volume of the cube is given as:

$$dv = \mathbf{F}d\mathbf{X}_1 \cdot (\mathbf{F}d\mathbf{X}_2 \times \mathbf{F}d\mathbf{X}_3) \tag{4.27}$$

Noting that the above triple product is the determinant of $\mathbf{F}$ which gives the volume change in terms of Jacobian J as

$$dv = JdV \qquad \text{and} \qquad J = \det F \tag{4.28}$$

This is known as Nanson's Formula and provides a simple and highly useful expression of the local change in volume between the reference and current configurations.

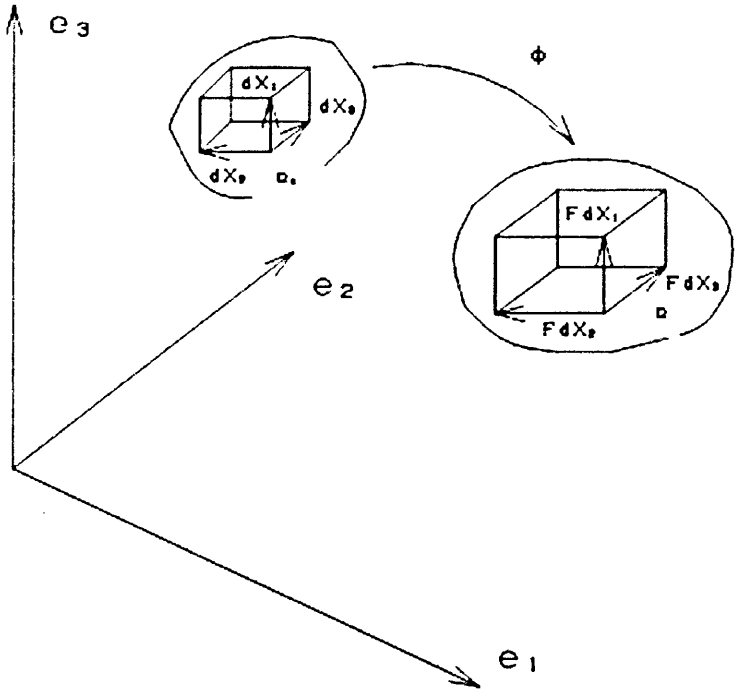

Figure 4.3 Deformation of an infinitesimal cube

4.1.7 Polar Decomposition of the Deformation Gradient

The deformation gradient can be expressed as the product of a rotation tensor R times a symmetric positive definite tensor **U** or **V**:

$$\mathbf{F} = \mathbf{RU} = \mathbf{VR} \tag{4.29}$$

in which **U** and **V** are two positive definite symmetric tensors, termed the right and left stretch tensors respectively. The right and left stretch tensors are related by the rotation

$$\mathbf{V} = \mathbf{RUR}^{T} \tag{4.30}$$

The stretch tensors **U** and **V** can be calculated as follows:

$$\mathbf{U} = \sqrt{\mathbf{C}} \quad \text{and} \quad \mathbf{V} = \sqrt{\mathbf{B}} \tag{4.31}$$

where **B** and **C** denote the right and left Cauchy-Green strain tensor:

$$\mathbf{C} = \mathbf{U}^2 = \mathbf{F}^{T}\mathbf{F} \quad \text{and} \quad \mathbf{B} = \mathbf{V}^2 = \mathbf{F}\mathbf{F}^{T} \tag{4.32}$$

Figure 4.4 describes the polar decomposition.

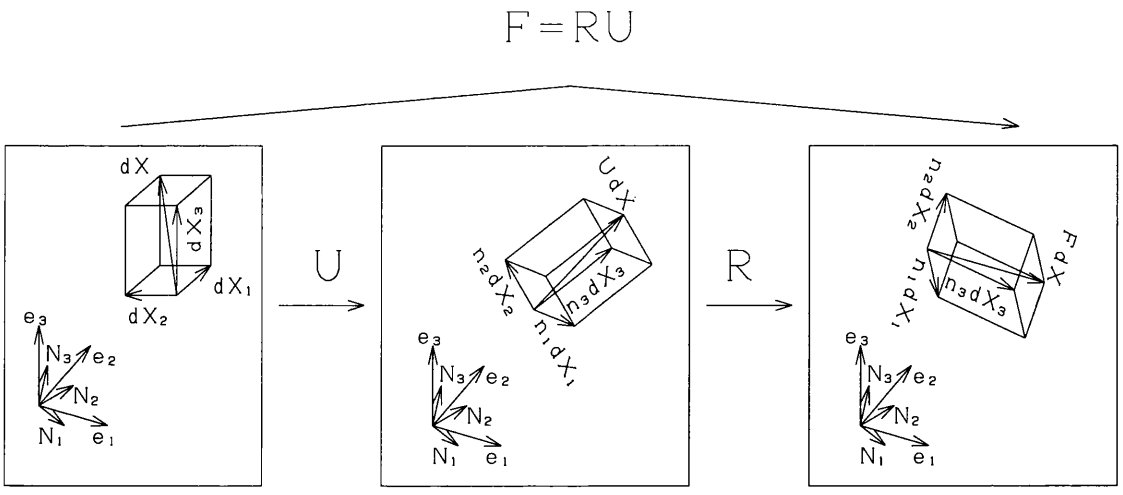

Figure 4.4 Polar decomposition of F (Note: n_i are the eigenvalues)

4.1.8 Strain

Consider the change in the variable product of the elemental vector dX_1 shown in Figure 4.2 to dx_1. This change will involve both in length and angle. The Lagrange or Green strain tensor $\mathbf{E}$ is defined as follow:

$$\frac{1}{2}(dx_1 dx_1 - dX_1 dX_1) = d\mathbf{X}_1 \cdot \mathbf{E} d\mathbf{X}_1 \tag{4.33}$$

in which, the material tensor $\mathbf{E}$ is given as follow:

$$\mathbf{E} = \frac{1}{2}(\mathbf{C} - \mathbf{M}) = \frac{1}{2}(\mathbf{F}^T\mathbf{F} - \mathbf{M}) \tag{4.34}$$

The Eulerian or Almansi strain tensor $\mathbf{e}$ is defined as follow:

$$\frac{1}{2}(dx_1 dx_1 - dX_1 dX_1) = d\mathbf{x}_1 \cdot \mathbf{e} d\mathbf{x}_1 \tag{4.35}$$

In equation (4.33), the spatial tensor $\mathbf{e}$ is given as:

$$\mathbf{e} = \frac{1}{2}(\mathbf{M} - \mathbf{B}^{-1}) = \frac{1}{2}(\mathbf{M} - \mathbf{F}^{-T}\mathbf{F}^{-1}) \tag{4.36}$$

4.2 Forces and Stresses

The previous section has introduced the mathematical concepts describing the kinematics of deformation, such as the deformation gradient, rotations, etc. In this section, we introduce the concept of distributed forces. These are forces acting on a continuum body which, like the matter in the continuum, are smoothly distributed in space.

4.2.1 The Cauchy Traction

For a general continuum body, $\mathbf{B}$, in the current position, we consider an infinitesimal patch of surface, of area Δs, within the body's domain Ω. In order to

study the action of the forces, we cut the body into two parts, H and G, to conceptually expose the surface patch. The patch of area Δs with normal **n** in the neighbourhood of spatial point **x** is shown in Figure 4.5.

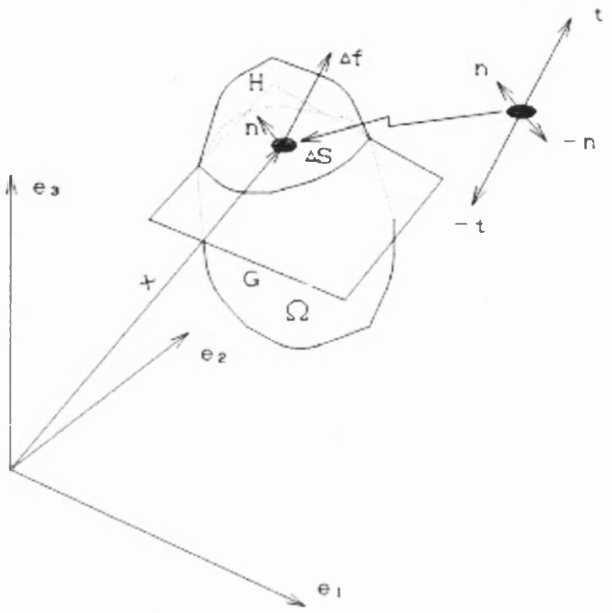

Figure 4.5 Traction on an infinitesimal surface element

If the resultant force on this area is Δ**f**, the traction vector t corresponding to the normal **n** at **x** is defined as:

$$\mathbf{t}(\mathbf{n}) = \lim_{\Delta s \to 0} \frac{\Delta \mathbf{f}}{\Delta s} \tag{4.37}$$

where the relationship between and **n** must satisfies Newton's third law of action and reaction:

$$\mathbf{t}(-\mathbf{n}) = -\mathbf{t}(\mathbf{n}) \tag{4.38}$$

The Cauchy traction is the force per unit area measured in the current configuration. It is also possible to define a similar vector, **T**, based on the area of

the surface element in the reference configuration corresponding to Δs. This is known as the first Piola-kirchhoff traction vector and is expressed by:

$$\mathbf{T}(\mathbf{X}, t, \mathbf{N}) = \lim_{\Delta s \to 0} \frac{\Delta \mathbf{f}}{\Delta s} \tag{4.39}$$

in which, $\Delta \mathbf{f}$ represents the force acting on that surface element in the current configuration onto which the material surface element about material position $\mathbf{X}$, and with area Δs and normal $\mathbf{N}$, is mapped by the motion at time t.

Body forces

Consider an elemental volume Δv around the point $\mathbf{x}$ in the current configuration within the body, $\mathbf{B}$. Let $\Delta \mathbf{f}$ be the net resultant sum of all the forces acting on the particles within Δv. The body force at point $\mathbf{x}$ is defined as:

$$\mathbf{b}(\mathbf{x}, t) = \lim_{\Delta s \to 0} \frac{\Delta \mathbf{f}}{\Delta s} \tag{4.40}$$

Internal and external forces

It is important to make a further distinction between the actions influencing a continuum:

1) Internal forces are the forces exerted on particles within the body from other particles elsewhere in the body.

2) External forces are forces acting on particles within the body that arise from influences outside the body.

4.2.2 The Cauchy Stress Tensor

By studying the translational equilibrium of the elemental tetrahedron (see Figure 4.6), we can obtain the Cauchy stress tensor σ_{ij}. Let f be the force per unit volume acting on the body at point x. The equilibrium of the tetrahedron is given by:

$$\mathbf{t}(\mathbf{n})\,da + \sum_{i=1}^{3} \mathbf{t}(-\mathbf{e}_i)\,da_i + \mathbf{f}\,dv = \mathbf{0} \tag{4.41}$$

where $da_i=(\mathbf{n}\cdot\mathbf{e}_i)da$ is the projection of the area da onto the plane orthogonal to the Caresian direction i (see Figure 4.6) and dv is the volume of the tetrahedron. Dividing equation (4.41) by da, recalling Newton's third law and noting that $dv/da \to 0$ gives,

$$\mathbf{t}(\mathbf{n}) = -\sum_{j=1}^{3} \mathbf{t}(-\mathbf{e}_j)\frac{da_j}{da} - \mathbf{f}\frac{dv}{da} = \sum_{j=1}^{3} \mathbf{t}(\mathbf{e}_j)(\mathbf{n}\cdot\mathbf{e}_j) = \sum_{i,j=1}^{3} \sigma_{ij}(\mathbf{e}_j\cdot\mathbf{n})\mathbf{e}_i \tag{4.42}$$

The $(\mathbf{e}_j\cdot\mathbf{n})\mathbf{e}_i$ can be rewritten in terms of the tensor product as $(\mathbf{e}_j\otimes\mathbf{e}_i)\mathbf{n}$ gives,

$$\mathbf{t}(\mathbf{n}) = \sum_{i,j=1}^{3} \sigma_{ij}(\mathbf{e}_j\cdot\mathbf{n})\mathbf{e}_i = \sum_{i,j=1}^{3} \sigma_{ij}(\mathbf{e}_i\otimes\mathbf{e}_j)\,\mathbf{n} = \left[\sum_{i,j=1}^{3} \sigma_{ij}(\mathbf{e}_i\otimes\mathbf{e}_j)\right]\mathbf{n} \tag{4.43}$$

The components σ_{ij} define the Cauchy or true stress tensor. The relation between the normal vector $\mathbf{n}$ and the traction vector $\mathbf{t}$ is given as follow:

$$t_i = \sigma_{ij} n_j \tag{4.44}$$

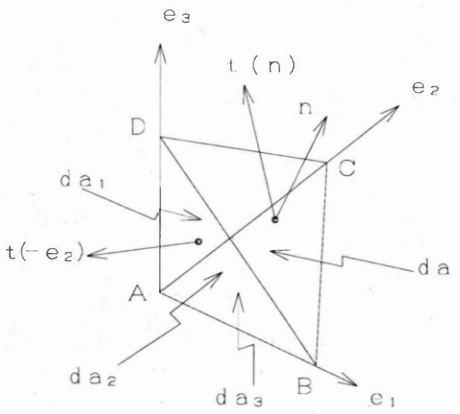

Figure 4.6 Elementary tetrahedron within body

4.2.3 The First Piola-Kirchhoff Stress Tensor

In 4.2.1, we introduce the first Piola-Kirchhoff traction vector, $\mathbf{T}(\mathbf{X},t,\mathbf{N})$, which measures the force across an Eulerian surface element per unit area of the corresponding Lagrangian surface element at material position $\mathbf{X}$.

Thus, the resultant force on an infinitesimal spatial surface Δs to normal $\mathbf{n}$ can be expressed either in terms of the Cauchy traction or in terms of the first Piola-Kirchhoff traction:

$$\Delta s\, \mathbf{t}(\mathbf{n}) = \Delta S \mathbf{T}(\mathbf{N}) \tag{4.45}$$

in which, ΔS represents the area of the corresponding elemental Lagrangian surface and $\mathbf{N}$ denotes its normal in the reference configuration.

By introducing the tensorial expression of the Cauchy traction into equation (4.45), the new equation can be given as follow:

$$\Delta S \mathbf{T}(\mathbf{N}) = \Delta s \boldsymbol{\sigma}\, \mathbf{n} \tag{4.46}$$

Taking the Nansons formula (Equation 4.28) gives the following relationship:

$$ds = J F^{-T} dS \tag{4.47}$$

which relates the area vectors in the Lagrangian and Eulerian configurations.

The relation between the areas and normals in the current configuration and their material counterparts can be given as follows:

$$\Delta s\, \mathbf{n} = \Delta S\, J\, \mathbf{F}^{-T}\, \mathbf{N} \tag{4.48}$$

Substituting into the right hand side of Equation (4.46) leads to:

$$\Delta S\, \mathbf{T}(\mathbf{N}) = \Delta S\, J\, \boldsymbol{\sigma}\, \mathbf{F}^{-T}\, \mathbf{N} \tag{4.49}$$

Then,

$$\mathbf{T}(\mathbf{N}) = [J\,\boldsymbol{\sigma}\,\mathbf{F}^{-T}]\,\mathbf{N} \tag{4.50}$$

Thus the first Piola-Kirchhoff traction has a linear dependence on N.

Then, we define the first Piola-Kirchhoff stress tensor, p, from:

$$\mathbf{P} = J\,\boldsymbol{\sigma}\,\mathbf{F}^{-T} \tag{4.51}$$

Thus

$$\mathbf{T}(\mathbf{N}) = \mathbf{P}\,\mathbf{N} \tag{4.52}$$

4.2.4 Other Stress Tensors

Other stresses are used in the nonlinear theory of continuum mechanics. Two of commonly used stresses are defined in this section.

1) The second Piola-Kirchhoff stress tensor

$$\mathbf{S} = J\,\mathbf{F}^{-1}\,\boldsymbol{\sigma}\,\mathbf{F}^{-T} \tag{4.53}$$

This definite may be inverted to give the Cauchy stress in terms of $\mathbf{S}$:

$$\boldsymbol{\sigma} = J^{-1}\,\mathbf{F}\,\mathbf{S}\,\mathbf{F}^{T} \tag{4.54}$$

2) The Kirchhoff stress tensor

$$\boldsymbol{\tau} = J\,\boldsymbol{\sigma} \tag{4.55}$$

Definition equation (4.55) may easily be inverted to give the Cauchy stress in terms of $\mathbf{S}$:

$$\boldsymbol{\sigma} = J^{-1}\,\boldsymbol{\tau} \tag{4.56}$$

4.3 Conservation Principles

In this section we seek to express some of fundamental equation of continuum mechanics which arise from the conservation principles. These equations must always be satisfied by physical systems.

4.3.1 Mass Conservation

The Lagrangian mass density at point **X** in the material configuration is denoted ρ_0 and defined by:

$$\rho_0 = \lim_{\Delta V} \frac{\Delta M}{\Delta V} \tag{4.57}$$

where ΔM represents the mass of a material element of volume ΔV at X.

The corresponding Eulerian mass density at point $\mathbf{x}=\varphi(\mathbf{X}, t)$ in the spatial configuration is denoted ρ and defined by:

$$\rho = \lim_{\Delta v} \frac{\Delta m}{\Delta v} \tag{4.58}$$

in which Δm represents the mass of a spatial element of volume Δv at x.

The mass m of a material domain Ω is given by:

$$m(\Omega) = \int_{\Omega} \rho d\Omega \tag{4.59}$$

As mass conservation requires that the mass of any material domain be constant, for Lagrangian description, Equation (4.59) can be integrated in time to obtain an equation:

$$\int_{\Omega} \rho d\Omega = \text{contstant} = \int_{\Omega_0} \rho_0 d\Omega_0 \tag{4.60}$$

Transforming the left-hand integral in the above to the reference domain by equation (4.28) gives,

$$\int_{\Omega_0} (\rho J - \rho_0) d\Omega_0 = 0 \tag{4.61}$$

Thus

$$\rho J = \rho_0 \tag{4.62}$$

This is known as the mass conservation.

4.3.2 Conservation of Linear Momentum

We consider an arbitrary reference domain Ω_0 with boundary Γ_0 subjected to body forces $\rho_0 \mathbf{b}$ and to surface tractions t_0, where $\mathbf{b}$ is a force per unit mass and t_0 is a force per unit area. In a Lagrangian description, the linear momentum of a body is given in terms of an integral over the reference configuration by

$$p = \int_{\Omega_0} \rho_0 V \, d\Omega_0 \tag{4.63}$$

The total force on the body is given by integrating the body forces over the reference domain and the traction over the reference boundaries:

$$f = \int_{\Omega_0} \rho_0 b \, d\Omega_0 + \int_{\Gamma_0} t_0 \, d\Gamma_0 \tag{4.64}$$

Newton's second law then gives

$$\frac{dp}{dt} = f \tag{4.65}$$

Substituting equation (4.63) and equation (4.64) into equation (4.65)

$$\frac{\mathrm{d}}{\mathrm{dt}}\int_{\Omega_0}\rho_0 \mathrm{V}\,\mathrm{d}\Omega_0 = \int_{\Omega_0}\rho_0 \mathrm{b}\,\mathrm{d}\,\Omega_0 + \int_{\Gamma_0} t_0\,\mathrm{d}\Gamma_0 \tag{4.66}$$

On the LHS, the material derivative can be taken inside the integral because the reference domain is constant in time, so

$$\frac{\mathrm{d}}{\mathrm{dt}}\int_{\Omega_0}\rho_0 \mathrm{V}\,\mathrm{d}\Omega_0 = \int_{\Omega_0}\rho_0 \frac{\partial V}{\partial t} d\Omega_0 \tag{4.67}$$

Using Cauchy' law and Gauss's theorem in sequence gives

$$\int_{\Gamma_0} \mathrm{t}_0\ \mathrm{d}\,\Gamma_0 = \int_{\Gamma_0} n \cdot P d\Gamma_0 = \int_{\Omega_0} div_0 \cdot P d\Omega_0 \tag{4.68}$$

Substituting equation (4.67) and equation (4.68) into equation (4.66) gives

$$\int_{\Omega_0}(\rho_0 \frac{\partial V}{\partial t} - \rho_0 b - div_0 P) d\Omega_0 = 0 \tag{4.69}$$

which, because of the arbitrariness of Ω_0, gives

$$\rho_0 \frac{\partial V}{\partial t} = div_0 \cdot P + \rho_0 b \tag{4.70}$$

It can be shown that the spatial formulation of the momentum balance is

$$\rho \frac{\partial v}{\partial t} = div \cdot \sigma + \rho b \tag{4.71}$$

This is known as the Cauchy's first equation of motion.

4.4 Principle of Virtual Work

Equation (4.69) expresses the strong form of the linear momentum balance, however, the weak form of momentum conservation provides the basis of most finite element method solutions to problem in solid mechanics.

Virtual work in the spatial description

We consider an arbitrary spatial vector field, $\xi(x)$, with the dimensions of distance. These virtual displacements are independent of time. Taking the dot product of equation (4.71) with ξ and integrating over the volume of the body's domain Ω with boundary $\partial\Omega$ gives:

$$\int_{\Omega} (\operatorname{div}\sigma + \rho b - \rho \frac{Dv}{Dt}) \cdot \xi dv = 0 \qquad \text{for arbitrary } \xi \qquad (4.72)$$

Equation (4.72) can be expressed as follow:

$$\int_{\Omega} [\operatorname{div}\sigma \cdot \xi + (\rho b - \rho \frac{Dv}{Dt}) \cdot \xi] dv = 0 \qquad \text{for arbitrary } \xi \qquad (4.73)$$

Considering the first term of the integrand, we have:

$$\operatorname{div}\sigma \cdot \xi = \frac{\partial \sigma_{i,j}}{\partial x_j} = \frac{\partial}{\partial x_j}(\sigma_{i,j}\xi_i) - \sigma_{i,j}\frac{\partial \xi_i}{\partial x_j} = div(\sigma\xi) - \sigma : \nabla\xi \qquad (4.74)$$

Substituting into equation (4.73)

$$\int_{\Omega} [div(\sigma\xi) - \sigma : \nabla\xi + (\rho b - \rho \frac{Dv}{Dt})\xi] dv = 0 \qquad \text{for arbitrary } \xi \qquad (4.75)$$

Application of the divergence theorem to the first term of the integrand yields:

$$\int_{\partial\Omega} (\sigma\xi) \cdot n \, ds - \int_{\Omega} [\sigma : \nabla\xi - (\rho b - \rho \frac{Dv}{Dt}) \cdot \xi] dv = 0 \qquad \text{for arbitrary } \xi \qquad (4.76)$$

The first integrand may be rewritten as:

$$(\sigma\xi) \cdot n = \sigma_{ij}\xi_j n_i = \sigma_{ji} n_i \xi_j = (\sigma n) \cdot \xi \qquad (4.77)$$

so that equation (4.76) becomes:

$$\int_{\partial\Omega} (\sigma n)\cdot\xi ds - \int_{\Omega} [\sigma : \nabla\xi - (\rho b - \rho\frac{Dv}{Dt})\cdot\xi] dv = 0 \qquad \text{for arbitrary } \xi \qquad (4.78)$$

On the boundary $\boldsymbol{\sigma}\cdot\mathbf{n}=\mathbf{t}$, where $\mathbf{t}$ is the applied boundary traction. Thus we obtain the virtual work equation in the spatial description:

$$\int_{\partial\Omega} t\cdot\xi ds - \int_{\Omega} [\sigma : \nabla\xi - (\rho b - \rho\frac{Dv}{Dt})\cdot\xi] dv = 0 \qquad \text{for arbitrary } \xi \qquad (4.79)$$

Virtual work in the material description

The principle of virtual work may also be expressed in terms of material quantities as follow:

$$\int_{\partial\Omega_0} t\cdot\xi dS - \int_{\Omega_0} [P : \nabla_0\xi - (\rho_0 b - \rho_0\frac{DV}{Dt})\cdot\xi] dV = 0 \qquad \text{for arbitrary } \xi \qquad (4.80)$$

4.5 Lagrangian Meshes

In the Lagrangian meshes, the nodes and elements move with the material. Boundaries and interfaces remain coincident with element edges, so that their treatment is simplified. Quadrature points also move with the material, so constitutive equations are always evaluated at the same material point, which is advantageous for history-dependent materials. For these reasons, Lagrangian meshes are widely used for solid mechanics.

Finite element discretisation with Lagrangian meshes are commonly classified as updated Lagrangian formulations and total Lagrangian formulations. Both formulations use Lagrangian descriptions. In the updated Lagrangian

formulation, the derivatives are with respect to the spatial (Eulerian) coordinates, and the weak form involves integrals over the deformed (current) configuration. In the total Lagrangian formulation, the weak form involves integrals over the initial (reference) configuration and derivatives are taken with respect to the material coordinates. We will take the updated Lagrangian finite element formulation as examples to explain discretisation.

4.5.1 Principle of Virtual Power for the Updated Lagrangian Formulation.

The principle of virtual power is the weak form of the momentum equation, the traction boundary conditions and the interior traction continuity conditions. These three are collectively called generalized momentum balance. The relationship of the principle of virtual power to the momentum equation will be described below.

We first define the spaces for the test functions and trial functions:

1) The space of test functions is defined by:

$$\delta v_j(X) \in \mu_0 \ , \ \mu_0 = \{\delta v_i \mid \delta v_i \in C^0(X),\ \delta v_i = 0 \text{ on } \Gamma_{v_i}\} \tag{4.81}$$

2) The trial function is given by:

$$v_i(X,t) \in \mu \ , \ \mu = \{v_i \mid v_i \in C^0(X),\ v_i = \bar{v}_i \text{ on } \Gamma_{vi}\} \tag{4.82}$$

Note that in the equation discretization introduced in the next Chapter, the continuity of the dependent variables must be considered. We will describe the continuity of a function as follows: a function is C^n if the n^{th} derivative is a

continuous function. Thus a C^1 function is continuously differentiable (its first derivative exists and is continuous everywhere). In a C^0 function, the derivative is only piecewise differentiable; discontinuities in the function occur at points or a one dimensional function. For a two dimensional C^0 function, discontinuities occur on lines, for a C^0 three dimensional function on surfaces. A C^{-1} function is itself discontinuous, but we assume that between the points of discontinuity the function is continuously differentiable as many times as we like.

Recalling equation (4.71), the strong form, or generalized momentum balance, consists of the momentum equation, the traction boundary conditions and the traction continuity conditions, which are given as follows:

$$\frac{\partial \sigma_{ji}}{\partial x_j} + \rho b_i = \rho \dot{v}_i \quad \text{in} \quad \Omega \tag{4.83}$$

$$n_j \sigma_{ji} = t_i \qquad \text{on} \quad \Gamma_{t_i} \tag{4.84}$$

$$[n_j \sigma_{ji}] = 0 \qquad \text{on} \quad \Gamma_{int} \tag{4.85}$$

where Γ_{int} is the union of all surfaces.

The first step in the development of the weak form consists of taking the product of a test function δv_i with the momentum equation and integrating over the current configuration:

$$\int_\Omega \delta v_i \left(\frac{\partial \sigma_{ji}}{\partial x_j} + \rho b_i - \rho \dot{v}_i\right) d\Omega = 0 \tag{4.86}$$

The first term in equation (4.86) is next expanded by the product rule, which gives

$$\int_{\Omega} \delta v_i \frac{\partial \sigma_{ji}}{\partial x_j} d\Omega = \int_{\Omega} \left[\frac{\partial}{\partial x_j}(\delta v_i \sigma_{ji}) - \frac{\partial(\partial v_i)}{\partial x_j} \sigma_{ji} \right] d\Omega \tag{4.87}$$

The first term in equation (4.87) is then expanded by Gauss's theorem, which gives,

$$\int_{\Omega} \frac{\partial}{\partial x_j}(\delta v_i \sigma_{ji}) d\Omega = \int_{\Gamma_{int}} \delta v_i [n_j \sigma_{ji}] d\Gamma + \int_{\Gamma} \delta v_i n_j \sigma_{ji} d\Gamma \tag{4.88}$$

From traction continuity equation (4.85), the first integral on the RHS vanishes. For the second integral on the RHS we use the traction boundary conditions equation (4.84). Since the test function vanishes on the complement of the traction boundaries, Equation (4.88) becomes

$$\int_{\Omega} \frac{\partial}{\partial x_j}(\delta v_j \sigma_{ji}) d\Omega = \sum_{i=1}^{n_{SD}} \int_{\Gamma_{t_i}} \delta v_i t_i d\Gamma \tag{4.89}$$

When equation (4.89) is substituted into equation (4.87) we obtain

$$\int_{\Omega} \delta v_i \frac{\partial \sigma_{ji}}{\partial x_j} d\Omega = \sum_{i=1}^{n_{SD}} \int_{\Gamma_{t_i}} \delta v_i t_i d\Gamma - \int_{\Omega} \frac{\partial(\partial v_i)}{\partial x_j} \sigma_{ji} d\Omega \tag{4.90}$$

If equation (4.90) is then substituted into equation (4.86), we obtain

$$\int_{\Omega} \frac{\partial(\delta v_i)}{\partial x_j} \sigma_{ji} d\Omega - \sum_{i=1}^{n_{SD}} \int_{\Gamma_{t_i}} \delta v_i t_i d\Gamma - \int_{\Omega} \delta v_i \rho b_i d\Omega + \int_{\Omega} \delta v_i \rho \dot{v}_i d\Omega = 0 \tag{4.91}$$

The above is the weak form for the momentum equation, the traction boundary conditions and the interior continuity conditions. It is known as the principle of virtual power (Malvern, 1969)

Chapter 5

Introduction to finite element methods

Finite element methods are a computer-based numerical technique, and can be used to calculate deflection, stress, vibration, buckling and many other phenomena of many structural engineering problems. The methods can also be used to analyse either small or large-scale deflection under loading or applied displacement; and can reduce costs in physical tests. Thus, finite element methods have been extensively used in steel structure analyses.

In the finite element method, a structure is divided into many small simple blocks or elements (finite element discretization). The behaviour of an individual element can be described with a relatively simple set of equations. The equations, describing individual element behaviour, are joined into a large set of equations that describe the behaviour of the whole structure. The computer can solve this large set of simultaneous equations. From the solution, the computer extracts the behaviour of individual elements, and obtains the stress and deflection of every part of the structure. The stresses will be compared to the allowed value of stress for materials to be used, to check if the structure is sufficiently strong.

However, the most difficult part of finite element analyses from the practice point of view is to develop an accurate model which can correctly represent the whole structural system. Thus, the creation of a reliable finite element model is a primary aim for any structure analysis.

5.1 Finite Element Discretisation and Formulations

An appropriate element should be selected so that it can best predict the deformation mode of bolted connection elements and can develop the excessive deformation behaviour in steel connections. Consequently, the best appropriate solid element which can describe bolt connections is the three-dimensional brick element that has eight nodes with three degrees of freedom along the x, y, and z axis. This type of element is easily adapted to model interfaces between the connecting surfaces.

A typical 3D brick element is showed in Figure 5.1, with 3 translational degrees of freedom (DOF) per node along the x, y and z axes. A consistent scheme must be followed in node numbering for connectivity definition.

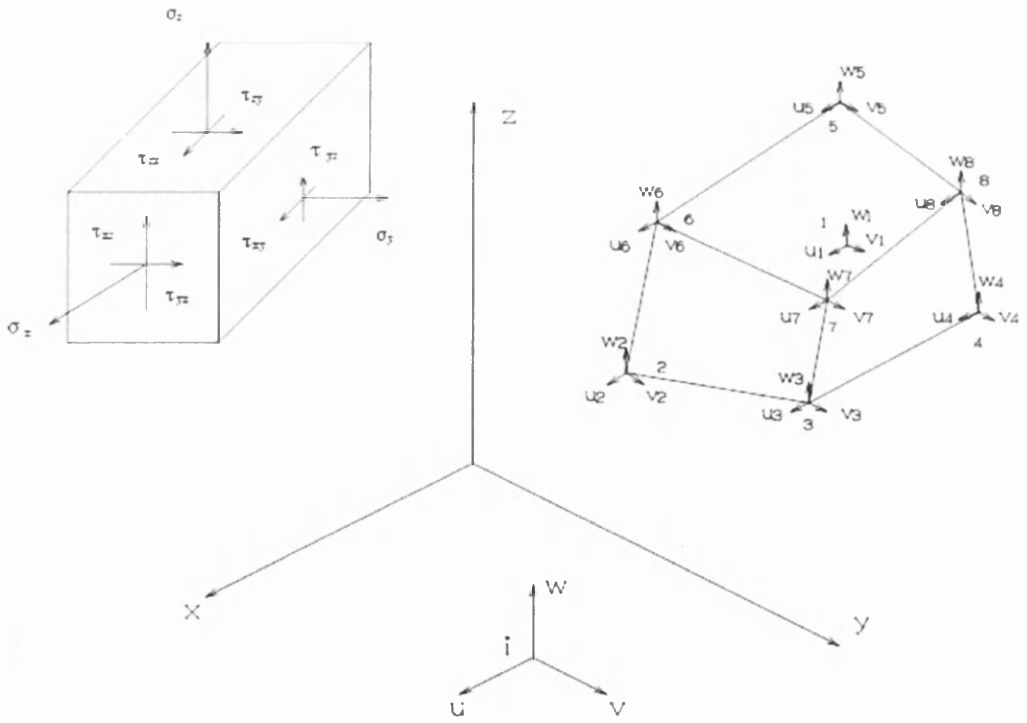

Figure 5.1 8 nodes brick element

The nodal displacement vectors are given by:

$$\mathbf{d} = \left[u_1, v_1, w_1, ..., u_8, v_8, w_8\right]^T \tag{5.1}$$

The strain and stress can be written as:

$$\boldsymbol{\sigma} = \left[\sigma_x, \sigma_y, \sigma_z, \tau_{yz}, \tau_{xz}, \tau_{xy}\right]^T \tag{5.2}$$

$$\boldsymbol{\varepsilon} = \left[\varepsilon_x, \varepsilon_y, \varepsilon_z, \gamma_{yz}, \gamma_{xz}, \gamma_{xy}\right]^T \tag{5.3}$$

For linear elastic materials, the stress-strain relationship can be expressed as:

$$\boldsymbol{\sigma} = \mathbf{E}\boldsymbol{\varepsilon} \tag{5.4}$$

where $\mathbf{E}$ is a (6×6) symmetric matrix. For isotropic material $\mathbf{E}$ is given as following,

$$\mathbf{E} = \frac{E}{(1+\nu)}\begin{bmatrix} 1-\nu & \nu & \nu & 0 & 0 & 0 \\ \nu & 1-\nu & \nu & 0 & 0 & 0 \\ \nu & \nu & 1-\nu & 0 & 0 & 0 \\ 0 & 0 & 0 & 0.5-\nu & 0 & 0 \\ 0 & 0 & 0 & 0 & 0.5-\nu & 0 \\ 0 & 0 & 0 & 0 & 0 & 0.5-\nu \end{bmatrix} \tag{5.5}$$

The strain $\boldsymbol{\varepsilon}$ can be related to the displacement by the strain-displacement relationship (for small deformation):

$$\boldsymbol{\varepsilon} = \begin{bmatrix} \frac{\partial}{\partial x} & 0 & 0 \\ 0 & \frac{\partial}{\partial y} & 0 \\ 0 & 0 & \frac{\partial}{\partial z} \\ 0 & \frac{\partial}{\partial z} & \frac{\partial}{\partial y} \\ \frac{\partial}{\partial z} & 0 & \frac{\partial}{\partial x} \\ \frac{\partial}{\partial y} & \frac{\partial}{\partial x} & 0 \end{bmatrix} \begin{Bmatrix} u \\ v \\ w \end{Bmatrix} \tag{5.6}$$

or

$$\varepsilon = \left[\left(\frac{\partial u}{\partial x}\right),\left(\frac{\partial v}{\partial y}\right),\left(\frac{\partial w}{\partial z}\right),\left(\frac{\partial v}{\partial z}+\frac{\partial w}{\partial y}\right),\left(\frac{\partial u}{\partial z}+\frac{\partial w}{\partial x}\right),\left(\frac{\partial u}{\partial y}+\frac{\partial v}{\partial x}\right)\right]^T \tag{5.7}$$

In order to define the displacement inside the element, the shape function is introduced to express the displacement at any point with its nodal values.

$$uu = N_1u_1 + N_2u_2 + ... + N_8u_8 \tag{5.8}$$

$$vv = N_1v_1 + N_2v_2 + ... + N_8v_8 \tag{5.9}$$

$$ww = N_1w_1 + N_2w_2 + ... + N_8w_3 \tag{5.10}$$

The displacement can be given the following equation:

$$\mathbf{u} = \mathbf{Nd} \tag{5.11}$$

where **N** is the matrix of the shape functions:

$$\mathbf{N} = \begin{bmatrix} N_1 & 0 & 0 & N_2 & 0 & 0 & ... & N_8 & 0 & 0 \\ 0 & N_1 & 0 & 0 & N_2 & 0 & ... & 0 & N_8 & 0 \\ 0 & 0 & N_1 & 0 & 0 & N_2 & ... & 0 & 0 & N_8 \end{bmatrix} \tag{5.12}$$

in which N_i can be compactly described for an eight-node brick element as follows:

$$N_i = \frac{1}{8}(1+\xi_i\xi)(1+\eta_i\eta)(1+\zeta_i\zeta) \qquad (i=1,2,...,8) \tag{5.13}$$

where η, ξ and ζ are the local coordinate system of the element (see Figure 5.2). For node 1 for instance, the corresponding natural coordinates ξ_1 ,η_1 and ζ_1 on are (-1,-1,-1). Therefore the shape function for node 1 will be as following:

$$N_1 = \frac{1}{8}(1+(-1)\xi)(1+(-1)\eta)(1+(-1)\zeta) \tag{5.14}$$

or

$$N_1 = \frac{1}{8}(1+\xi)(1+\eta)(1+\zeta) \tag{5.15}$$

Therefore, by using the iso-parametric concept, the coordinates of a point within

the element can also be expressed as

$$x = N_1x_1 + N_2x_2 + ... + N_8x_8 \tag{5.16}$$

$$y = N_1y_1 + N_2y_2 + ... + N_8y_8 \tag{5.17}$$

$$z = N_1z_1 + N_2z_2 + ... + N_8z_8 \tag{5.18}$$

where x_i, y_i, and z_i are the nodal coordinates.

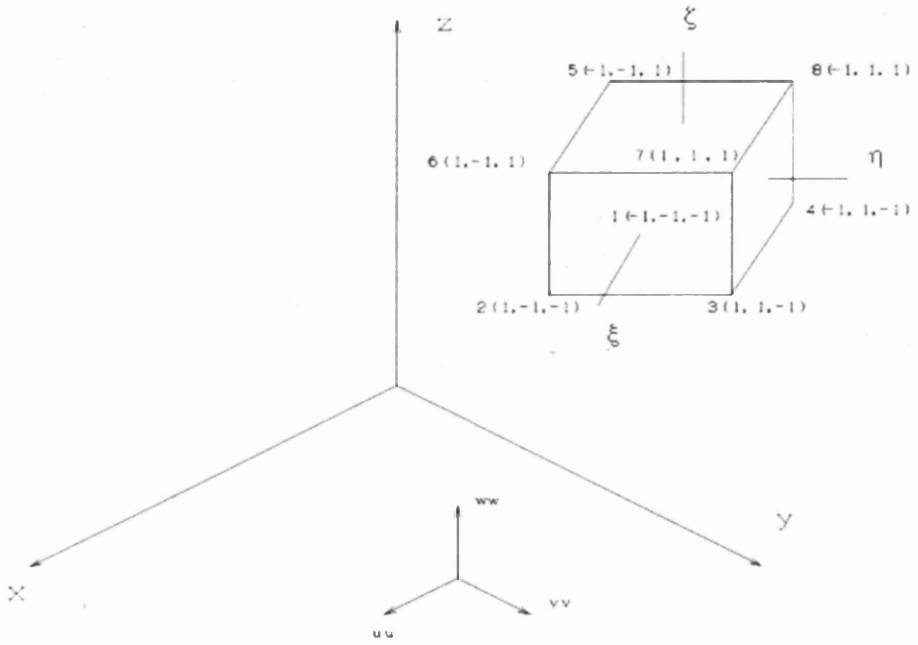

Figure 5.2 The brick element in ξ, η and ζ space

The Jacobian matrix (3×3) for the brick element is defined as:

$$\mathbf{J} = \begin{bmatrix} \frac{\partial x}{\partial \xi} & \frac{\partial y}{\partial \xi} & \frac{\partial z}{\partial \xi} \\ \frac{\partial x}{\partial \eta} & \frac{\partial y}{\partial \eta} & \frac{\partial z}{\partial \eta} \\ \frac{\partial x}{\partial \varsigma} & \frac{\partial y}{\partial \varsigma} & \frac{\partial z}{\partial \varsigma} \end{bmatrix} \tag{5.19}$$

By introducing a new tensor,

$$\Psi = \mathbf{J}^{-1} \tag{5.20}$$

the strain displacement tensor matrix can be given by the following equation:

$$\mathbf{B} = \Psi \mathbf{N} \tag{5.21}$$

The assembled strain energy can be expressed as the following equation:

$$U_e = \frac{1}{2}\mathbf{d}^{eT}\mathbf{k}\mathbf{d}^e \tag{5.22}$$

The dimension of the strain displacement tensor depends on the number of node. For the 8-noded element, it is (24×6). Then the element stiffness matrix for the brick element can be derived to be

$$\mathbf{k} = \int_{-1}^{1}\int_{-1}^{1}\int_{-1}^{1} \mathbf{B}^{\mathrm{T}}\mathbf{E}\mathbf{B}\left|\det \mathbf{J}\right| d\xi d\eta d\zeta \tag{5.23}$$

which det **J** represents the ratio of the volume dx, dy and dz to d ξ ,d η and d ζ .

The potential term of the body force can be given as the following:

$$\int_v \mathbf{u}^T \mathbf{f} dv = q^T \int_{-1}^{1}\int_{-1}^{1}\int_{-1}^{1} \mathbf{N}^T \mathbf{f} \det \mathbf{J} d\xi d\eta d\zeta \tag{5.24}$$

The potential term of the external traction force can be given as the following:

$$\int_s \mathbf{u}^T \mathbf{T} ds = q^T \int_s \mathbf{N}^T \mathbf{T} ds \tag{5.25}$$

Recalling Equation (4.91), finite element equations for the updated Lagrangian formulation are developed by means of the principle of virtual power. Thus, after some manipulation, the weak form of the momentum equation is given as follows:

$$\int_\Omega \frac{\partial N_I}{\partial x_j}\sigma_{ji} d\Omega - \sum_{i=1}^{n_{SD}} \int_{\Gamma_{t_i}} N_I t_i d\Gamma - \int_\Omega N_I \rho b_i d\Omega + \int_\Omega N_I \rho \dot{v}_i d\Omega = 0 \tag{5.26}$$

Internal and external nodal forces

From equation (5.26), it can be seen that the internal nodal forces are given as:

$$f_{iI}^{int} = \int_{\Omega} \frac{\partial N_I}{\partial x_j} \sigma_{ji} d\Omega \tag{5.27}$$

The external nodal forces are expressed as follows:

$$f_{iI}^{ext} = \int_{\Omega} N_I \rho \, b \, d\Omega + \int_{\Gamma_{t_i}} N_I \, t \, d\Gamma \tag{5.28}$$

Inertial forces and mass matrix

The inertial forces are expressed as follows:

$$f_I^{kin} = M_{IJ} \dot{v}_J \tag{5.29}$$

The mass matrix is given as follows:

$$M_{ijIJ} = \delta_{ij} \int_{\Omega} \rho N_I \, N_J d\Omega \tag{5.30}$$

Discrete equations

The discrete momentum equations are expressed as follows:

$$Ma + f^{int} = f^{ext} \tag{5.31}$$

where, a is the array of element nodal displacement adjustments and element stiffness matrix; and M is the mass matrix for the unconstrained degrees of freedom.

Thus, by finite element discretization, the complicated structure can be described with a relatively simple set of equations. Combining these set of equations, the behaviour of the whole structure can be solved by numerical techniques.

5.2 Modelling the Plasticity Behaviour of Steel

Plasticity theory has three parts: a yield criterion, a flow rule, and a hardening rule. The general theory and its various special forms are contrived to fit experimental data. A brief introduction of plasticity behaviour of steel is given below, which is mainly based on Mechanics of solid materials (J. Lemaitre and J. –L. Chaboche 1990).

Basis of plasticity

When materials reach yield state, an irreversible deformation occurs. The total strain can be decomposed into two parts: the elastic and plastic components:

$$\varepsilon_{ij} = \varepsilon_{ij}^{el} + \varepsilon_{ij}^{pl} \tag{5.32}$$

Yield criterion

The yield criterion is used to define the material yielding, and can be expressed as the following equation:

$$f(\sigma_{ij}) \leq 0 \tag{5.33}$$

Therefore, the yield function can be given as the following equation:

$$f\left(\sigma_{ij}, \sigma_y\right) = \sigma^* - \sigma_y \tag{5.34}$$

In perfect plasticity, σ^* expresses the equivalent stress and σ_y expresses the yield stress, respectively. If the equivalent stress σ^* is equal to the material yield stress value σ_y, then the material plastic strain will be developed. However, if the

equivalent stress σ^* is less than the material yield stress value, then the strain will be developed in the elastic behaviour of the stress-strain relationships.

Flow Rule

The rate of plastic flow is expressed as:

$$\left\{d\varepsilon^p\right\} = \left\{\frac{\partial Q}{\partial \boldsymbol{\sigma}}\right\} d\lambda, \quad d\lambda \geq 0 \tag{5.35}$$

where Q denotes the plastic potential, which has units of stress and is a function of the stress, Q=Q (σ); $d\lambda$ represents the plastic multiplicator, which equals to zero at elastic loading and is greater than zero at plastic loading. The flow rule is called associated if Q=f and non-associated otherwise. Associated flow rules are commonly used for ductile metals, but non-associated rules are better suited to soil and rock.

Hardening rule

In the case of perfect plasticity, the yield surface is unchanged during plastic deformation. However, this is not the case for most materials. The yield loci can be moved (kinematic hardening) or grow (isotropic hardening). Figure 5.3 shows the hardening rule in isotropic hardening behaviour.

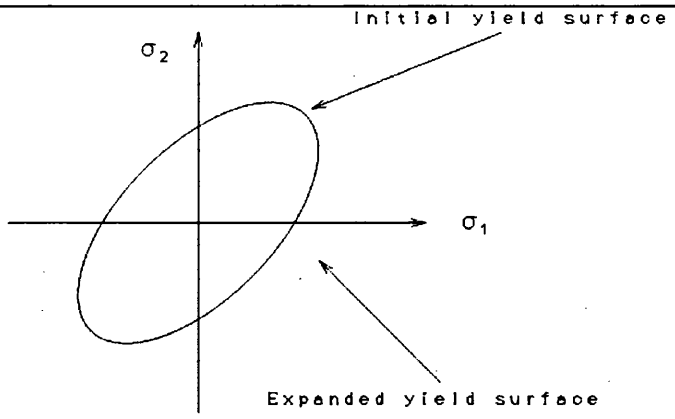

Figure 5.3 The hardening rule in isotropic hardening behaviour

For kinematic hardening, the effective stress is a function of overstress $\boldsymbol{\sigma}$ which is given as the following equation:

$$\sum = \boldsymbol{\sigma} - \mathbf{b} \tag{5.36}$$

in which $\mathbf{b}$ represents the back stress, and can be used to measure how much the yield locus moves.

The yield stress is also the function of history variables $\mathbf{r}$, and can be defined as:

$$\sigma_y = \sigma_y(\mathbf{r}) \tag{5.37}$$

Thus, the yield function equation (5.34) can be rewritten as:

$$f(\sum, \sigma_y) = \sigma^*(\boldsymbol{\sigma} - \mathbf{b}) + \sigma_y(\mathbf{r}) \tag{5.38}$$

which shows that the shape of yield locus can also be changed.

Figure 5.4 shows the stress-strain relationship (σ^y-ε^y), where the dotted line represents perfect plasticity, and solid line represents linear hardening with hardening parameter H.

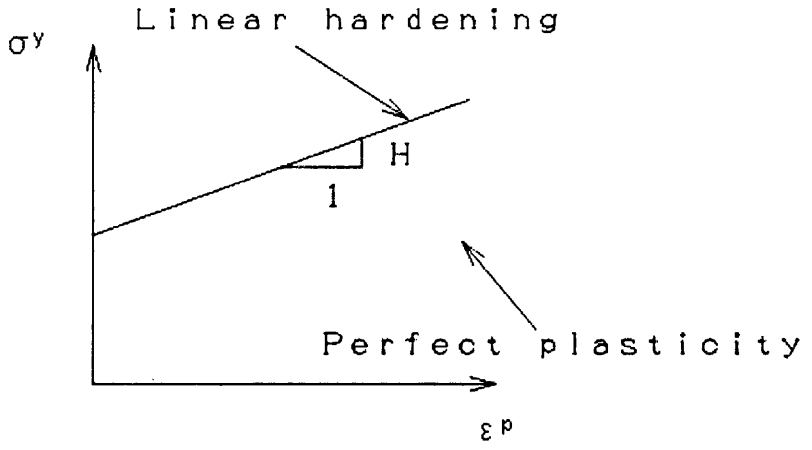

Figure 5.4 Perfect plasticity and linear hardening

The following equation can show this relationship:

$$\sigma^y = \sigma_0^y + K\varepsilon^n \tag{5.39}$$

in which, n and K represent material parameters, and $\sigma^y{}_0$ denotes the initial yield stress. Thus, by the aforementioned theory, the yield equation can be given as follow:

$$f\left(\boldsymbol{\sigma}, \boldsymbol{\alpha}, \mathbf{W}_p\right) = 0 \tag{5.40}$$

in which, $\boldsymbol{\alpha}$ and $\mathbf{W}_p$ denote the stress state variables: $\mathbf{W}_p$ denotes the plastic work per unit volume, and $\boldsymbol{\alpha}$ represents the shift of the yield surface, and both can be expressed as:

$$\mathbf{W}_p = \int \{\boldsymbol{\sigma}\}^T \left\{d\boldsymbol{\varepsilon}^p\right\} \tag{5.41}$$

$$\{\boldsymbol{\alpha}\} = \int C\left\{d\boldsymbol{\varepsilon}^p\right\} \tag{5.42}$$

where C is the material constant.

Differentiation of equations (5.41) and (5.42) yield the following equations:

$$d\mathbf{W}_p = \{\boldsymbol{\sigma}\}^T \{d\boldsymbol{\varepsilon}^p\} \tag{5.43}$$

$$\{d\boldsymbol{\lambda}\} = C\{d\boldsymbol{\varepsilon}^p\} \tag{5.44}$$

while differentiation of equation (5.40) yields the following consistency condition expression:

$$df = \left\{\frac{\partial f}{\partial \boldsymbol{\sigma}}\right\}^T \{d\boldsymbol{\sigma}\} + \frac{\partial f}{\partial \mathbf{W}_p} \partial \mathbf{W}_p + \left\{\frac{\partial f}{\partial \boldsymbol{\alpha}}\right\}^T \{d\boldsymbol{\alpha}\} = 0 \tag{5.45}$$

Substituting equation (5.43) and (5.44) into equation (5.45), the following expression can be obtained:

$$\left\{\frac{\partial f}{\partial \boldsymbol{\sigma}}\right\}^T \{d\boldsymbol{\sigma}\} + \frac{\partial f}{\partial \mathbf{W}_p} \{\boldsymbol{\sigma}\}^T \{d\boldsymbol{\varepsilon}^p\} + \left\{\frac{\partial f}{\partial \boldsymbol{\sigma}}\right\}^T C\{d\boldsymbol{\varepsilon}^p\} = 0 \tag{5.46}$$

The increment of stress can be calculated by using the stress-strain relation:

$$\{d\boldsymbol{\sigma}\} = [\mathbf{E}]\{d\boldsymbol{\varepsilon}^e\} \tag{5.47}$$

where

$$\{d\boldsymbol{\varepsilon}^e\} = \{d\boldsymbol{\varepsilon}\} - \{d\boldsymbol{\varepsilon}^p\} \tag{5.48}$$

Making these substitutions into equation (5.46), using equation (5.35) to eliminate $\{d\,\varepsilon^p\}$, and solving for the plastic multiplier $d\,\lambda$, we obtain

$$d\lambda = \{\mathbf{C}_\lambda\}^T \{d\boldsymbol{\varepsilon}\} \tag{5.49}$$

where,

$$\{\mathbf{C}_\lambda\}^T = \frac{\left\{\frac{\partial f}{\partial \boldsymbol{\sigma}}\right\}^T [\mathbf{E}]}{\left\{\frac{\partial f}{\partial \boldsymbol{\sigma}}\right\}^T [\mathbf{E}]\left\{\frac{\partial Q}{\partial \boldsymbol{\sigma}}\right\} - \frac{\partial f}{\partial \mathbf{W}_p}\{\boldsymbol{\sigma}\}^T \left\{\frac{\partial Q}{\partial \boldsymbol{\sigma}}\right\} - C\left\{\frac{\partial f}{\partial \boldsymbol{\alpha}}\right\}^T \left\{\frac{\partial Q}{\partial \boldsymbol{\sigma}}\right\}} \tag{5.50}$$

Finally, substituting equation (5.35) into equation (5.47), we obtain

$$\{d\boldsymbol{\sigma}\} = [\mathbf{E}]\left(\{d\boldsymbol{\varepsilon}\} - \left\{\frac{\partial Q}{\partial \boldsymbol{\sigma}}\right\} d\lambda\right) \text{ or } \{d\boldsymbol{\sigma}\} = [\mathbf{E}_{ep}]\{d\boldsymbol{\varepsilon}\} \tag{5.51}$$

where

$$[\mathbf{E}_{ep}] = [\mathbf{E}] - [\mathbf{E}]\left\{\frac{\partial Q}{\partial \boldsymbol{\sigma}}\right\}\{\mathbf{C}_\lambda\}^T \tag{5.52}$$

Matrix $[\mathbf{E}_{ep}]$ is symmetric if f=Q. It is valid even if the material is elastic-perfectly plastic. It can be used to generate a tangent-stiffness matrix $[\mathbf{k}_t]$, which expresses the relation between increments of nodal displacement and the resulting increments of nodal load,

$$[\mathbf{k}_t] = \int_{V_e} [\mathbf{B}]^T [\mathbf{E}_{ep}][\mathbf{B}] dV \tag{5.53}$$

$[\mathbf{E}_{ep}]$ is given by equation (5.52) if f=0 and df=0, but is replaced by elastic coefficients $[\mathbf{E}]$ if f<0 or if df<0.

The von Mises Criterion

For steel materials, the von Mises yield criterion is most commonly used, and is associated flow rule.

To begin with, we must introduce the so called deviatoric stresses $\{\mathbf{s}\}$, which are associated with distortion of the shape but no volume change. By definition,

$$\{\mathbf{s}\} = \{\boldsymbol{\sigma}\} - \sigma_m [1 \quad 1 \quad 1 \quad 0 \quad 0 \quad 0]^T \tag{5.54}$$

where σ_m is the mean or average normal stress:

$$\sigma_m = \frac{1}{3}(\sigma_x + \sigma_y + \sigma_z) \tag{5.55}$$

Thus $s_x = \sigma_x - \sigma_m$,..., $s_{zx} = \tau_{zx}$. For convenience, we split $\{\mathbf{s}\}$ into two parts: $\{\mathbf{s}_\sigma\}$

$$\{\mathbf{s}\} = \begin{Bmatrix} \mathbf{s}_\sigma \\ \mathbf{s}_\tau \end{Bmatrix} \tag{5.56}$$

where

$$\{\mathbf{s}_\sigma\} = \begin{Bmatrix} s_x \\ s_y \\ s_z \end{Bmatrix} \quad \text{and} \quad \{\mathbf{s}_\tau\} = \begin{Bmatrix} \tau_{xy} \\ \tau_{yx} \\ \tau_{zx} \end{Bmatrix} \tag{5.57}$$

Similarly, $\{\alpha\}$ of equation (5.42) is split into parts $\{\alpha_\sigma\}$ and $\{\alpha_\tau\}$. With σ_y the yield strength in a uni-axial tensile test, the yield function is

$$f = [\frac{3}{2}(\{s_\sigma\} - \{\alpha_\sigma\})^T(\{s_\sigma\} - \{\alpha_\sigma\}) + 3(\{s_\tau\} - \{\alpha_\tau\})^T(\{s_\tau\} - \{\alpha_\tau\})]^{\frac{1}{2}} - \sigma_y \tag{5.58}$$

As before, σ_y is taken as the initial yield strength (unchanged by the subsequent plastic strains). For uniaxial stress σ_x, with $\{\alpha\}$ initially zero, Equation (5.58) reduces to $f = |\sigma_x| - \sigma_y$, so that $|\sigma_x| = \sigma_y$ defines the onset of yielding.

To obtain an "associated" theory, we take Q=f. Thus, after some manipulations

$$\{d\varepsilon^p\} = \left\{\frac{\partial f}{\partial \boldsymbol{\sigma}}\right\} d\lambda = \left(\frac{3}{2\sigma_y} \begin{Bmatrix} \mathbf{s}_\sigma - \boldsymbol{\alpha}_\sigma \\ \mathbf{0} \end{Bmatrix} + \frac{3}{\sigma_y} \begin{Bmatrix} \mathbf{0} \\ \mathbf{s}_\tau - \boldsymbol{\alpha}_\tau \end{Bmatrix} \right) d\lambda \tag{5.59}$$

which is known as the Prandti-Reuss relation.

If the post-yield portion of the stress-strain relation is not to be idealized as a straight line, one must store the following data for an isotropic material: E, ν, σ_y, and a functional representation of H. ε^p_{ef} is an effective plastic strain defined by

$$\varepsilon^p_{ef} = \frac{\sqrt{2}}{3}\left[(\varepsilon^p_x - \varepsilon^p_y)^2 + (\varepsilon^p_y - \varepsilon^p_z)^2 + (\varepsilon^p_z - \varepsilon^p_x)^2 + \frac{3}{2}\{(\gamma^p_{xy})^2 + (\gamma^p_{yz})^2 + (\gamma^p_{zx})^2\}\right]^{\frac{1}{2}} \tag{5.60}$$

5.3 Solution Equations

Incremental method

Consider the tapered bar depicted in Figure 5.5.

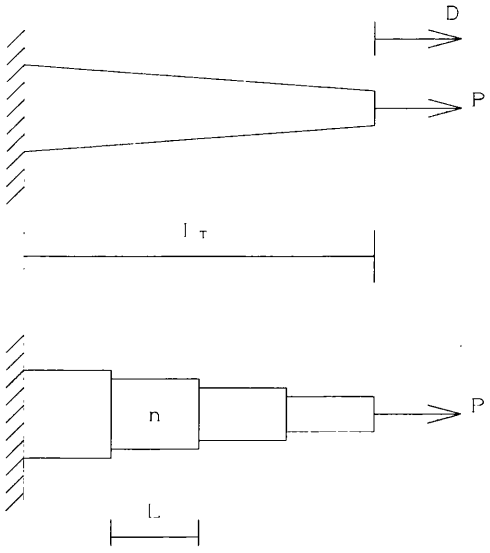

Figure 5.5 A finite element model of a tapered bar

It is desired to trace the static load versus displacement curve and determine element stresses by means of a finite element model and load increments $\triangle P$. Increments are small but not infinitesimal, so that $d\varepsilon$ becomes $\triangle\varepsilon$, and the numerical solution is not exact.

Material properties of this bar are depicted in Figure 5.6.

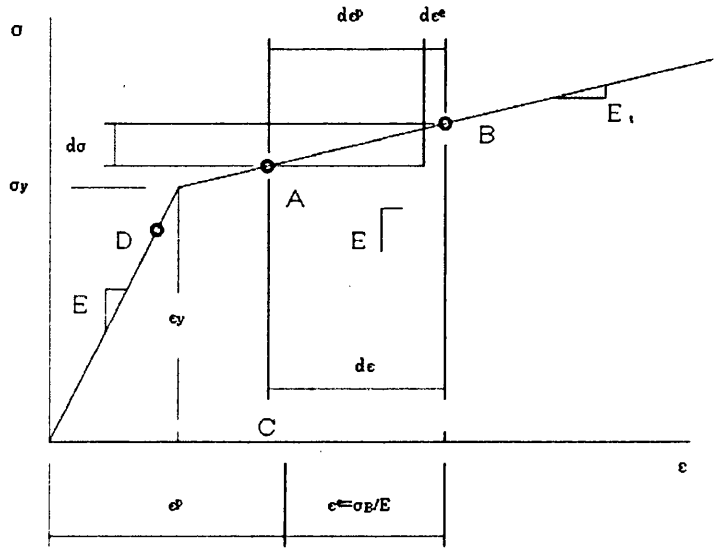

Figure 5.6 Stress-strain plot in uniaxial stress

For elastic conditions, the element stiffness matrix is given as follows:

$$[\mathbf{k}_e]=\frac{AE}{L}\begin{bmatrix}1 & -1\\ -1 & 1\end{bmatrix} \tag{5.61}$$

In which, $E=d\sigma/d\varepsilon$ when $|\sigma|<\sigma_y$, A is the cross-section area.

Upon yielding, the stress-strain relation becomes $E_t=d\sigma/d\varepsilon$. Accordingly, letting E_{ep} represent the "elastic-plastic" stiffness, we write the element tangent-stiffness matrix as

$$[\mathbf{k}_t] = \frac{AE_{ep}}{L}\begin{bmatrix} 1 & -1 \\ -1 & 1 \end{bmatrix} \tag{5.62}$$

In which, $E_{ep}=E$ if the yield criterion is not exceeded or if unloading is taking place, and $E_{ep}=E_t$, if plastic flow is involved, where E_t is the tangent modulus.

In order to obtain σ ,E, E_t for any ε , a numerical representation of the stress-strain algorithm must be stored. The algorithm outline below requires that we also store, and update after each computational cycle, the nodal displacements $\{\mathbf{D}\}$, element strains ε , and element stresses σ .

1. For the first computational cycle (i=1), assume $E_{ep}=E$ for all elements. Apply the first load increment, $\{\triangle\mathbf{R}\}_1$.

2. Using the current strains, determine the current E_{ep} in each element. Use equation (5.62) to obtain $[\mathbf{K}_t]_{i-1}=\sum[\mathbf{k}_t]_n$. Solve $[\mathbf{K}_t]_{i-1}\{\triangle\mathbf{D}\}=\{\triangle\mathbf{R}\}_i$ for $\{\triangle\mathbf{D}\}_i$. From $\{\triangle\mathbf{D}\}_i$, obtain current strain increments $\triangle\varepsilon_i$ for each element.

3. Update: $\{\mathbf{D}\}_i=\{\mathbf{D}\}_{i-1}+\{\triangle\mathbf{D}\}_i$, and for each element, $\varepsilon_i=\varepsilon_{i-1}+\triangle\varepsilon_i$ and $\sigma_i=\sigma_{i-1}+\triangle\sigma_i$, where $\triangle\sigma_i=(E_{ep})_i\triangle\varepsilon_i$.For the first cycle (i=1), initial values [subscript (i-1)] of displacement, strain and stress are typically all zero if one starts from the unloaded configuration, but are nonzero if one starts from a state in which phastic action impends.

4. Apply the next load increment and reture to step 2.

5. Stop when $\sum\{\triangle\mathbf{R}\}_i$ reaches the total applied load.

Three cycles of the foregoing algorithm are depicted in Figure 5.7

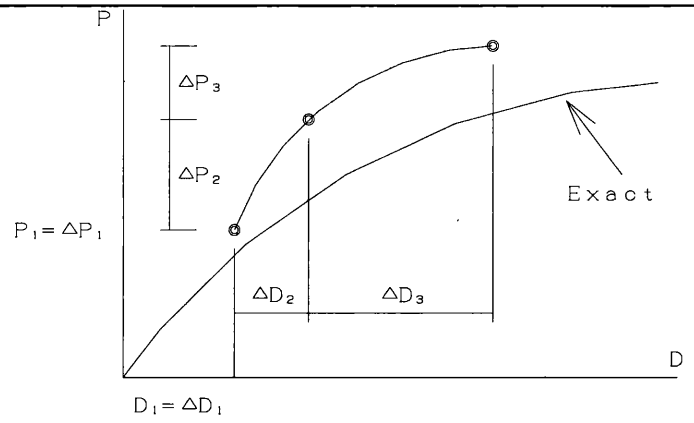

Figure 5.7 An example of progress of a Newton-Raphson method (step 3)

Analysis procedures

We assume that a tensile test of the material has been performed, and a numerical representation of its stress-strain curve is stored. We also assume that specific choices of yield criterion, flow rule, and hardening rule have been made. For steel column-beam connection structures, we choose the von Mises yield criterion, the Prandtl-Reuss flow relationship, iso-tropic hardening, and a bilinear stress-strain relation, then we need to store only E, ν, σ_y, and H for an isotropic material. Alternatively, to represent a more general stress-strain relation, H may be defined as a function of ε^p_{ef} [see Equation (5.60)]. Then, in computation, we must record and update the value of ε^p_{ef} at each sampling point, and use it to obtain the current value H.

Suppose that a load $\{\mathbf{R}\}$ on the structure is applied in increments $\{\Delta\mathbf{R}\}_1$, $\{\Delta\mathbf{R}\}_2$, ... so that $\{\mathbf{R}\}=\sum\{\mathbf{R}\}_i$. The first load increment might be contrived to place the most highly stressed sampling point on the verge of yield. The computational steps are as follows:

1. At the outset, $\{\boldsymbol{\varepsilon}\}=\{\boldsymbol{\sigma}\}=\{\boldsymbol{\alpha}\}=\{\mathbf{0}\}$, $W_p=0$, and $[\mathbf{E}_{ep}]=[\mathbf{E}]$ for all sampling point. These values prevail in the first computational cycle (i=1). Apply the first load increment, $\{\Delta\mathbf{R}\}_1$.

2. Use the current condition $\{\boldsymbol{\sigma}\}_{i-1}$, $\{\boldsymbol{\alpha}\}_{i-1}$, and $W_{p(i-1)}$ to evaluate $[E_{ep}]_{i-1}$ for each sampling point. Note that $[\mathbf{E}_{ep}]_{i-1}=[\mathbf{E}]$ for sampling points that have yet to yield ($f<0$ for the current $\{\boldsymbol{\sigma}\}_{i-1}$, $\{\boldsymbol{\alpha}\}_{i-1}$, and $W_{p(i-1)}$) or are unloading ($df<0$ for the most recent changes in $\{\boldsymbol{\sigma}\}$, $\{\boldsymbol{\alpha}\}$ and W_p). Evaluate $[\mathbf{k}_t]$ for each element. The structure tangent-stiffness matrix is formed by the usual assembly, $[\mathbf{K}_t]_{i-1}=\sum[\mathbf{k}_t]_n$. Solve for structure displacement increments $\{\Delta\mathbf{D}\}_i$ and strain increments $\{\Delta\boldsymbol{\varepsilon}\}_i$ at element sampling points from the equations

$$[\mathbf{K}_t]_{i-1}\{\mathrm{V}\mathbf{D}\}_i=\{\mathrm{V}\mathbf{R}\}_{i-1} \qquad \text{and} \qquad \{\mathrm{V}\boldsymbol{\varepsilon}\}_i=[\mathbf{B}]\{\mathrm{V}\mathbf{d}\}_i \tag{5.63}$$

For sampling point in the plastic range, compute increments as follows,

$$\mathrm{V}\lambda_i=\int\{\mathbf{C}_\lambda\}^T\{d\boldsymbol{\varepsilon}\}\approx\{\mathbf{C}_\lambda\}_{i-1}^T\{\mathrm{V}\boldsymbol{\varepsilon}\}_i \tag{5.64}$$

$$\{\mathrm{V}\boldsymbol{\varepsilon}^p\}_i=\int\left\{\frac{\partial Q}{\partial\boldsymbol{\sigma}}\right\}d\lambda\approx\left\{\frac{\partial Q}{\partial\boldsymbol{\sigma}}\right\}_{i-1}\mathrm{V}\lambda_i \tag{5.65}$$

$$\{\mathrm{V}\boldsymbol{\sigma}\}_i=[\mathbf{E}](\{\mathrm{V}\boldsymbol{\varepsilon}\}_i-\{\mathrm{V}\boldsymbol{\varepsilon}^p\}_i) \tag{5.66}$$

$$\{\mathrm{V}\boldsymbol{\alpha}\}_i=\int C\{d\boldsymbol{\varepsilon}^p\}\approx C\{\mathrm{V}\boldsymbol{\varepsilon}^p\}_i \tag{5.67}$$

$$\mathrm{V}W_{pi}=\int\{\boldsymbol{\sigma}\}^T\{d\boldsymbol{\varepsilon}^p\}\approx\{\boldsymbol{\sigma}\}_i^T\{\mathrm{V}\boldsymbol{\varepsilon}^p\}_i \tag{5.68}$$

3. Without changing the load or recalculating $\{\Delta\mathbf{D}\}_i$, one can evaluate equations (5.64) to (5.68) more accurately by dividing the increment $\{\Delta\boldsymbol{\varepsilon}\}_i$ into

subincrements. After each such subincremental cycle, one updates $\{\boldsymbol{\sigma}\}_i$, $\{\boldsymbol{\alpha}\}_i$, and so on. Note that $\{C_\lambda\}_{i-1}$ is zero in elastic sub-increments if the sampling point makes the elastic-to-plastic transition within the current load step.

4. Update the solution:

$$\{\mathbf{D}\}_i = \{\mathbf{D}\}_{i-1} + \{\mathrm{V}\mathbf{D}\}_i \tag{5.69}$$

$$\{\boldsymbol{\sigma}\}_i = \{\boldsymbol{\sigma}\}_{i-1} + \{\mathrm{V}\boldsymbol{\sigma}\}_i \tag{5.70}$$

$$\{\boldsymbol{\alpha}\}_i = \{\boldsymbol{\alpha}\}_{i-1} + \{\mathrm{V}\boldsymbol{\alpha}\}_i \tag{5.71}$$

$$(W_p)_i = (W_p)_{i-1} + (\mathrm{V}W_p)_i \tag{5.72}$$

5. Apply the next load increment and return to step 2

6. Stop when $\sum\{\mathbf{R}\}_i$ reaches the total applied load.

CHAPTER 6

FEM modelling and validation

In the past century, hundreds of thousands of tests have been conducted on steel structures that include beams, columns, and connections. This has led to many improvements in the behaviours and designs of steel beam-to-column connections. Over the last several decades, finite element modelling techniques have been applied to simulate the behaviour of various steel connections. For the current problem concerned, after the validation against available test data, the finite element method will provide the opportunity for wider parametric investigation and eliminates some of limitations associated with experimental investigations. Consequently, the finite element method provides the main source of information and will be of great benefit when examining the influence of the connection parameters on the overall behaviours by allowing a wide ranging parametric study to be conducted which will be difficult to achieve in experimental environment.

6.1 Finite Element Models

A three-dimensional finite element model of the RHS column-to I beam connection is carried out using the HYPERMESH (Altair) pre-processor. The connections are analyzed using the finite element software package, ABAQUS.

The finite element mesh used in the analysis is shown in Figure 6.1. The mesh

contains 36481 nodes, and 25569 elements. In the process of the mesh generation, the connection is divided into six individual components. These components are showed in Figures 6.2 and 6.3, and are referred to as the column, beam, fin plate, diaphragm, bolt, and weld.

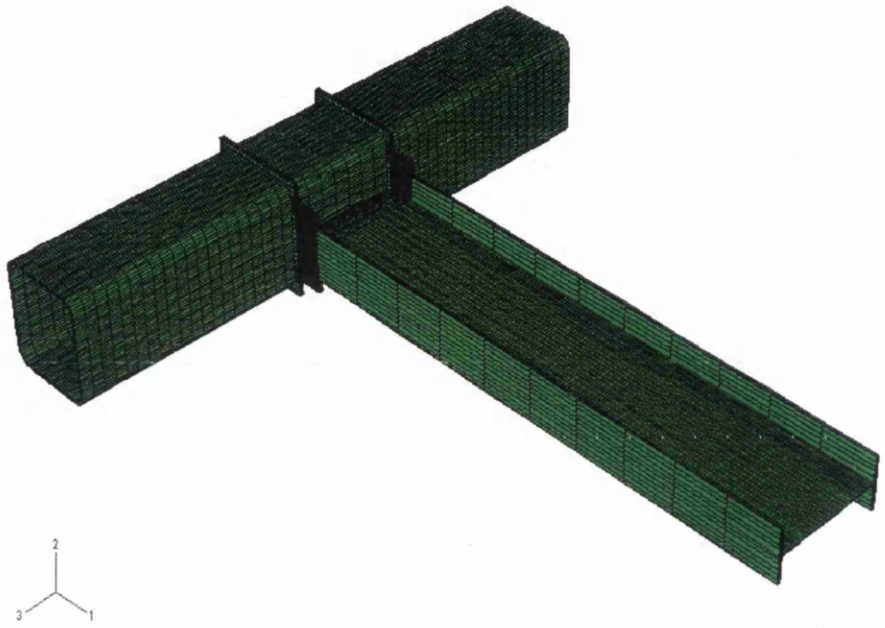

Figure 6.1 Finite element mesh of RHS column-to I beam connection

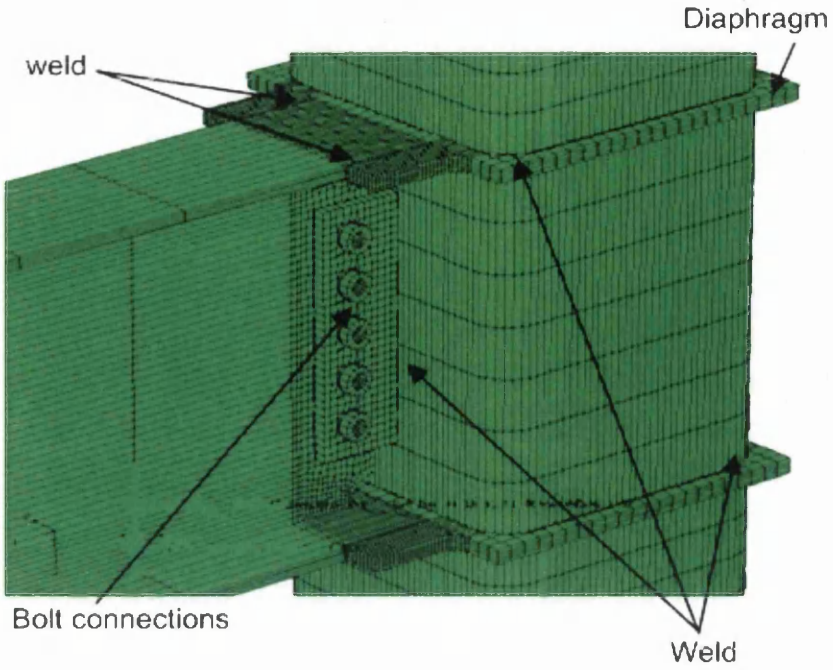

Figure 6.2 Mode component (T-2, 3)

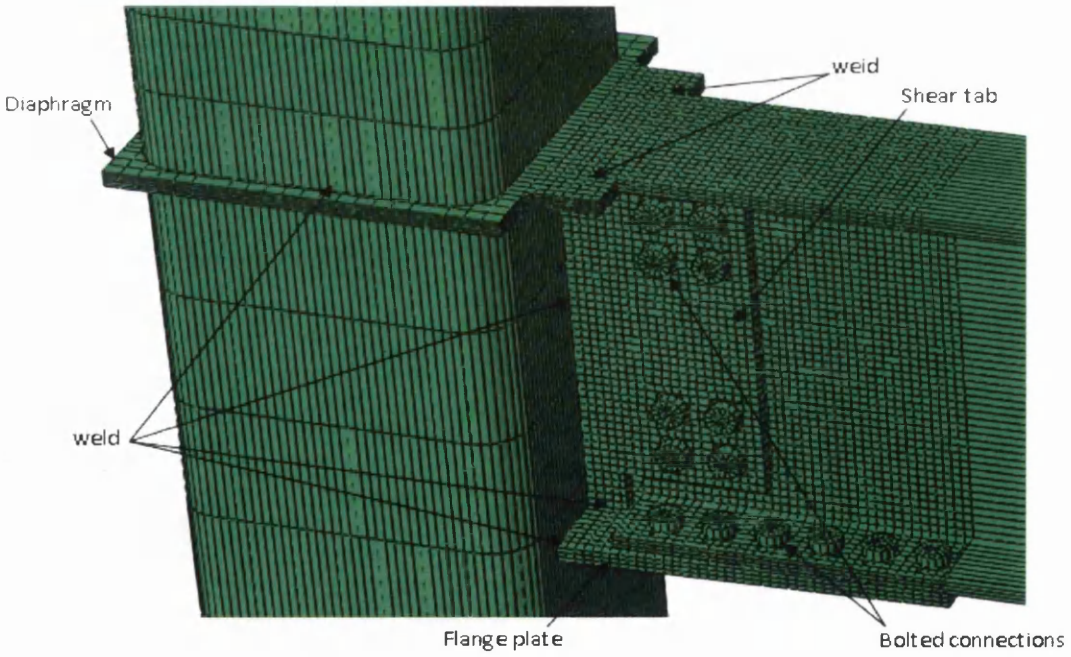

Figure 6.3 Mode component (T-4)

1) Column, beam, diaphragm and fin plate

The column, beam, diaphragm and fin plate are modeled using 3-D 8-node brick elements. Linear hybrid elements are selected to prevent the possible problem of volume strain locking. Following a convergence study, four elements through the thickness of the diaphragm and beam flange are used. Furthermore, to reduce the number of elements and nodes in the FE model, only one element is used for the column, beam web and fin plate through their thickness.

2) Weld

There are two types of welding. One type is the filled weld, including fin plate-to-column. The other is groove weld, including diaphragm-to-column and beam-to-diaphragm. In the finite element model, the weld is assumed to be an extension of the diaphragm sections, column sections and fin plate section, therefore have the same material properties. Consequently, the weld is modeled as an individual component in the connection model using 8-node brick elements.

3) Bolt

The model of bolt constructed using 8-node brick elements and 6-node triangular prism elements is shown in Figure6.4.

The bolt connections include three main parts, beam, fin plate and bolts. To capture the accurate stress behavior, an intensive mapped mesh is made around the boltholes. The hexagon bolt heads are modeled as cylinders.

The small sliding interaction behavior between surfaces is considered for all the contact surfaces in order to fully transfer the load from the beam web to the fin plate, and finally, to the column.

The following contact interactions for bolt connection are considered: 1) Contact between the bolt shank and the bolt hole. 2) Contact between the bolt head and the beam web. 3) Contact between the nut and the fin plate. 4) Contact the fin

plate and the beam web. Pre-tension is not applied to the bolts during the analysis in T-2 and 3, but in T-4, the bolts are pre-loaded by a tensile stress of 520 N/mm^2 according to Japan industrial standard (AIJ) and a friction coefficient μ=0.45 is used for all the contact surfaces.

Although two cycles of loading are applied at each displacement increment in the experiments, in the numerical analyses, only one cycle for each displacement increment is exerted to the beam to save computational time.

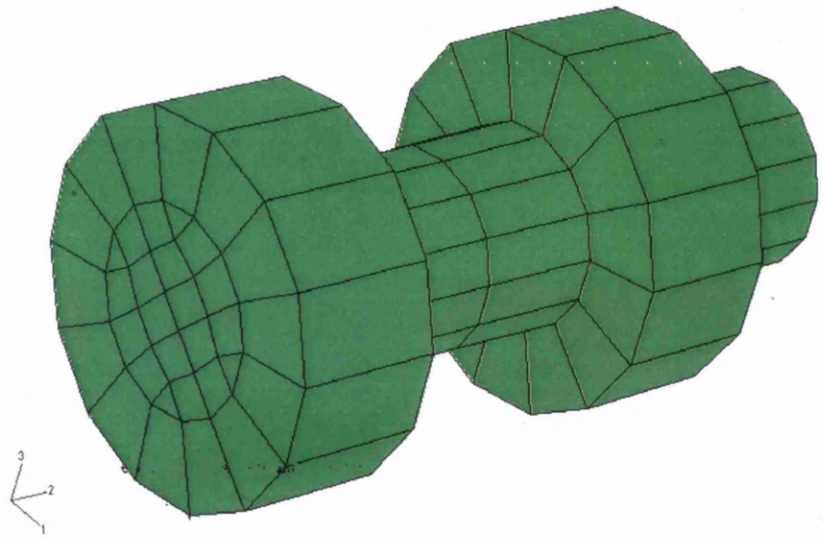

Figure 6.4 Finite element mode of bolt

For the ABAQUS simulation, the nominal engineering stress-strain relation obtained from steel tensile coupon test (see Table 3.1) is converted to the true stress-strain relationship, according to: $\sigma_{tru} = \sigma_{nom}(1+\varepsilon_{nom})$ and $\varepsilon_{tru} = \ln(1+\varepsilon_{nom})$, in which σ_{tru} and ε_{tru} represent the true stress and strain; and σ_{nom} and ε_{nom} are the nominal stress and strain respectively.

Both ends of the column are fully constrained.

6.2 Validation

The numerical analyses of specimens are finished when the connections fail with the maximal rotation $6\theta_p$. Figures 6.5~6.8 show both the simulated and experimental results, and they reveal that when the beam tip rotation is between $4\theta_p$ and $-4\theta_p$, the experimental and numerical loops match well. However, when the rotation is over $4\theta_p$ and $-4\theta_p$, the numerical loops overestimate the stiffness of the specimens. The difference between the experimental and numerical loops is likely caused by the difference between the nominal and measured material properties and inaccurate measurement of the specimen dimensions in this study.

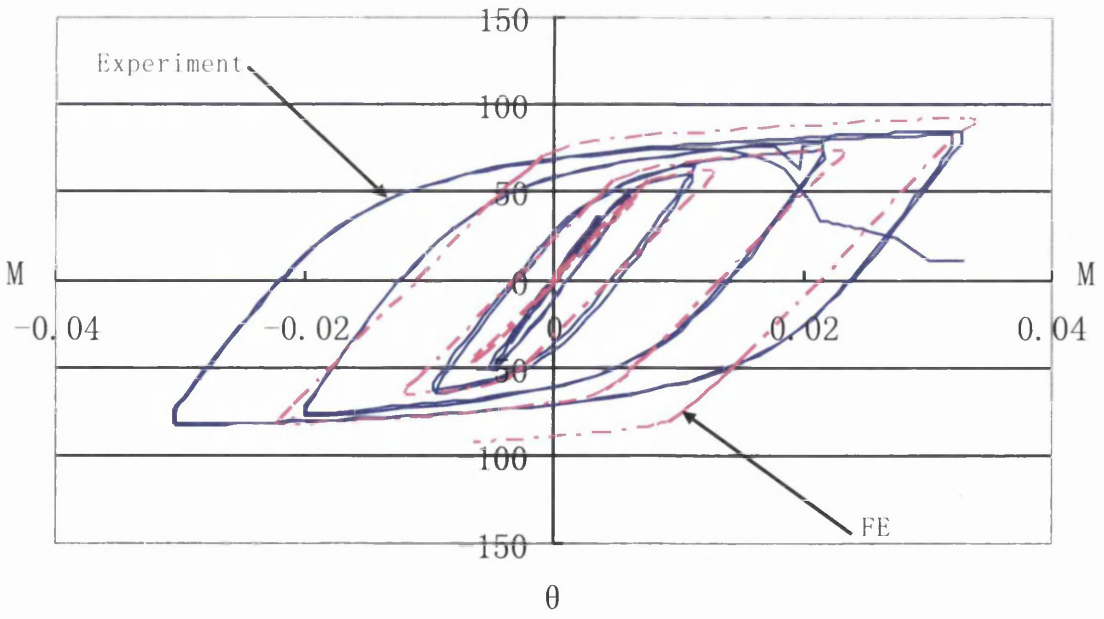

Figure 6.5 Hysteresis curve (T-1)

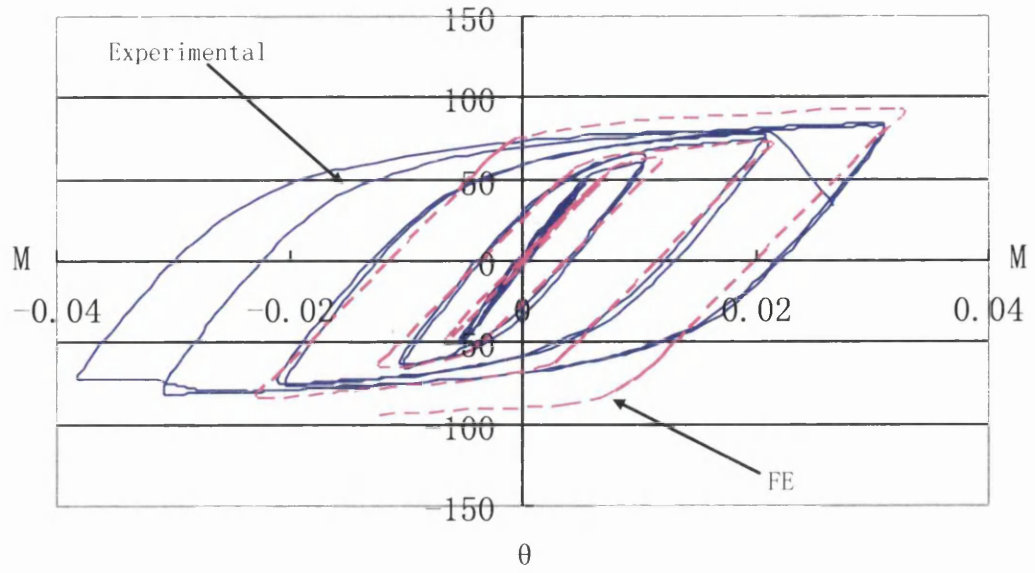

Figure 6.6 Hysteresis curve (T-2)

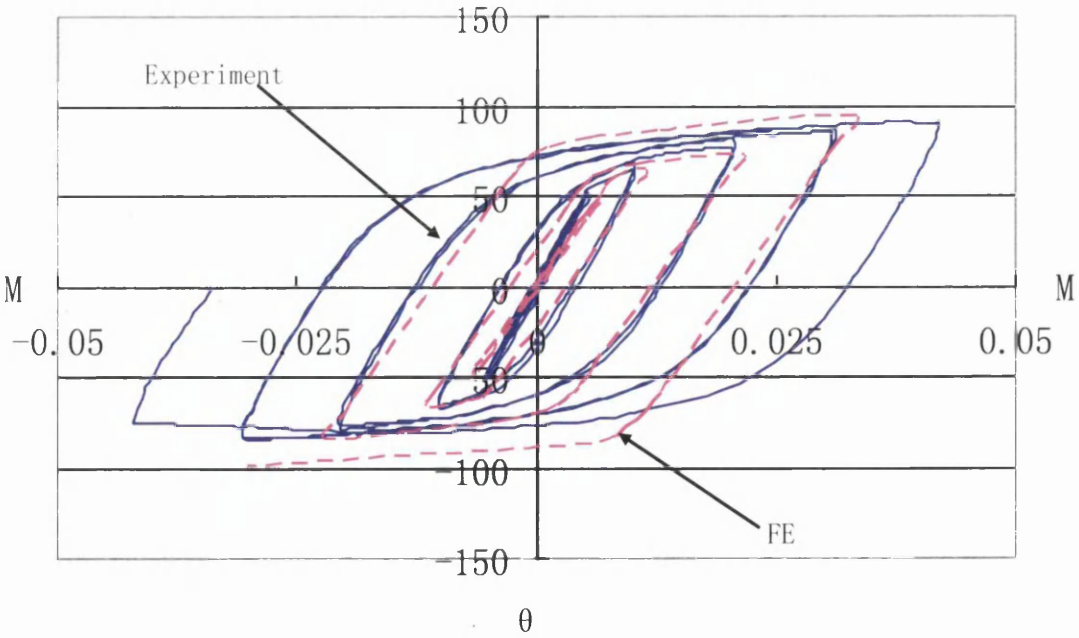

Figure 6.7 Hysteresis curve (T-3)

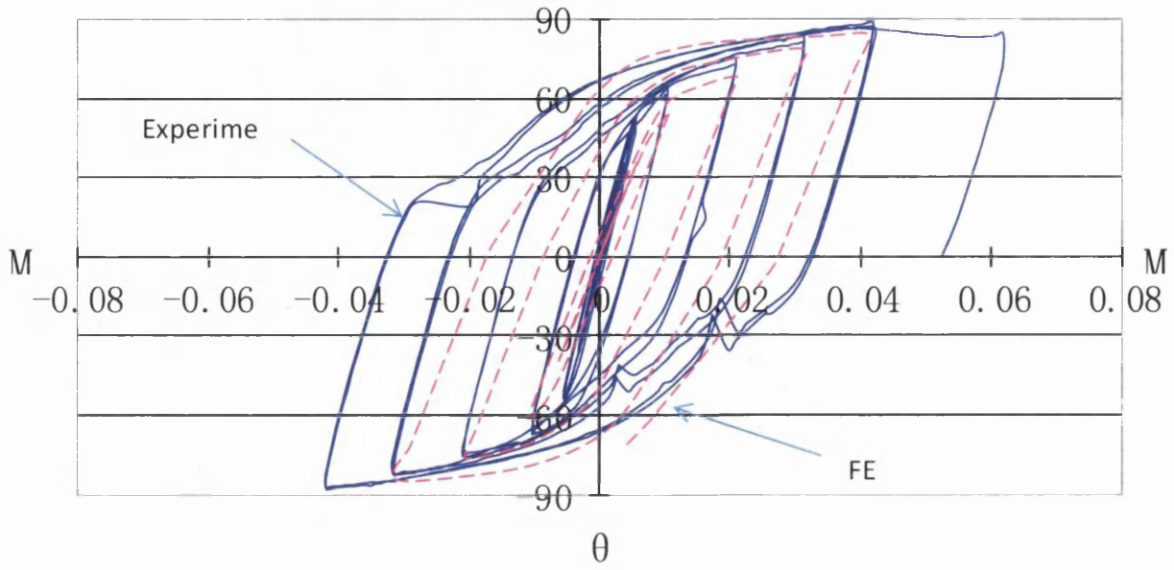

Figure 6.8 Hysteresis curve (T-4)

The moment-rotation relationships for specimens T-1, T-2 , T-3 and T-4 analyzed by FEM are shown in Figure 6.9, in which the curves, test1-1 (FE), test2-1 (FE), test3-1 (FE), test4-1 (FE) are obtained from FE analyses, and test1, test2, test3, test4 are obtained from the so-called skeleton curves. The skeleton curve is constructed from a hysteretic curve by linking a portion of the curve that exceeds the maximum load in the preceding loading cycle sequentially (see Appendix 3). Comparison of the finite element results with the experimental moment-rotation curve (see Figures 6.10~6.13) shows good agreement in terms of general behaviour and the maximum values with a difference around 10%. An observation of finite element failure mode shows a similarity to the test results (see Figures 3.11 and 6.14, Figures 3.13 and 6.15).

This proves that the finite element method is capable of accurately predicting RHS column-to-I beam connection behaviour.

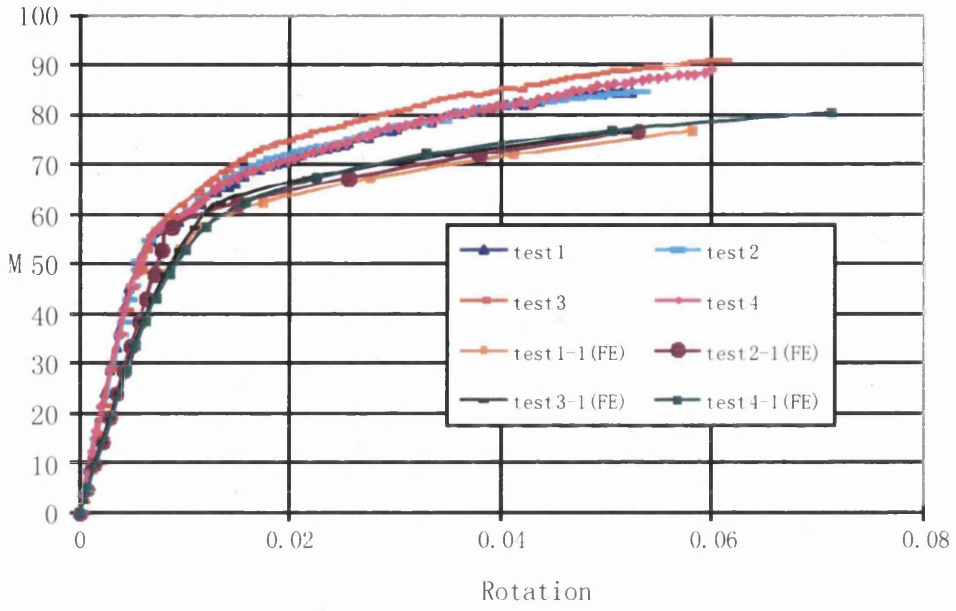

Figure 6.9 Moment-rotation relationships

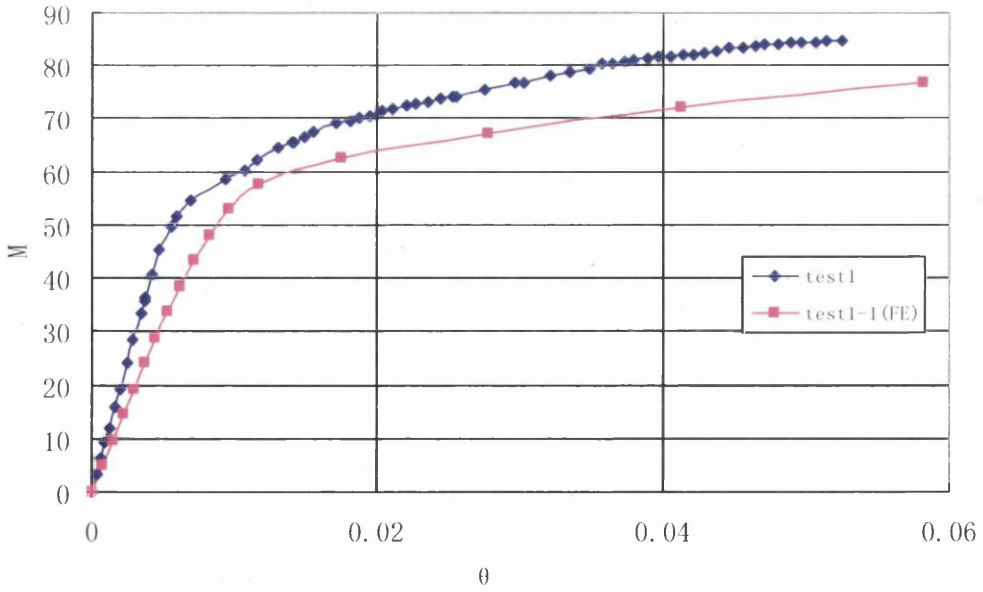

Figure 6.10 Moment-rotation relationships (T-1)

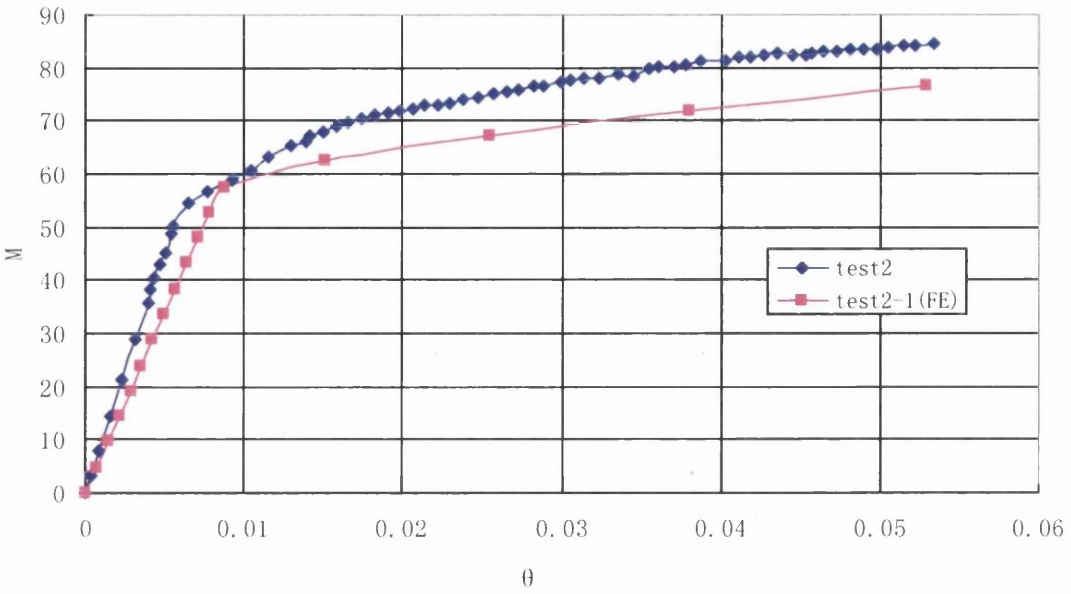

Figure 6.11 Moment-rotation relationships (T-2)

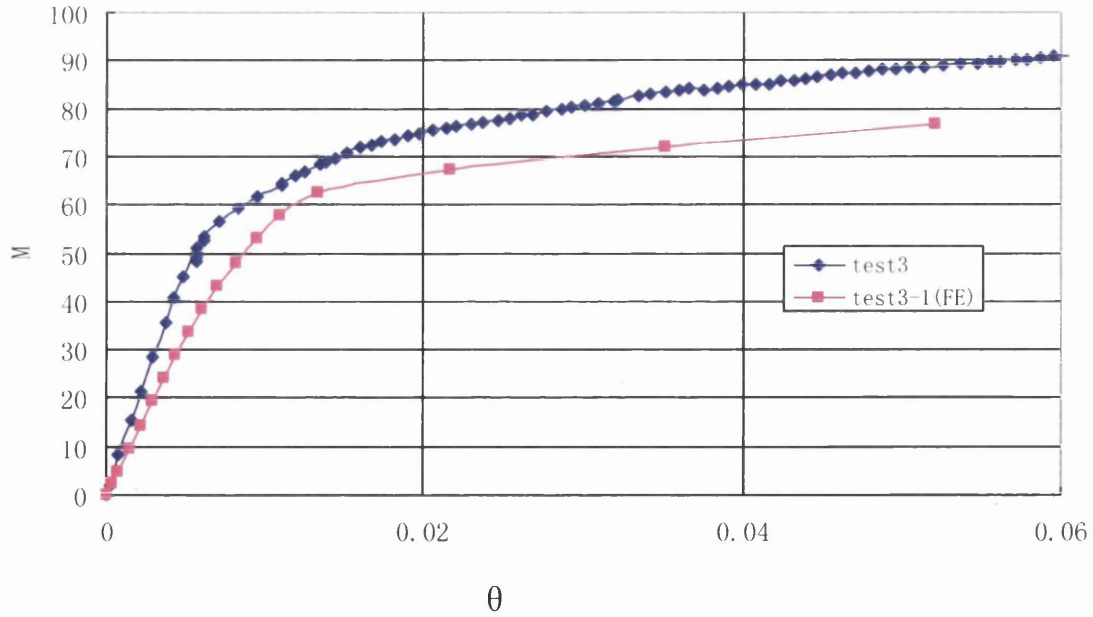

Figure 6.12 Moment-rotation relationships (T-3)

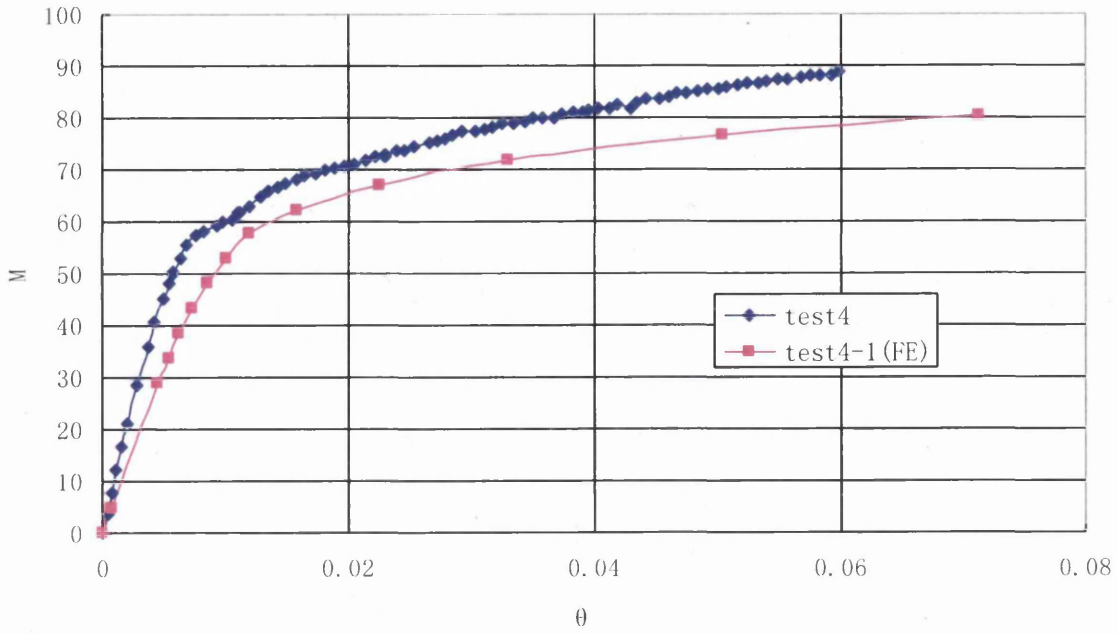

Figure 6.13 Moment-rotation relationships (T-4)

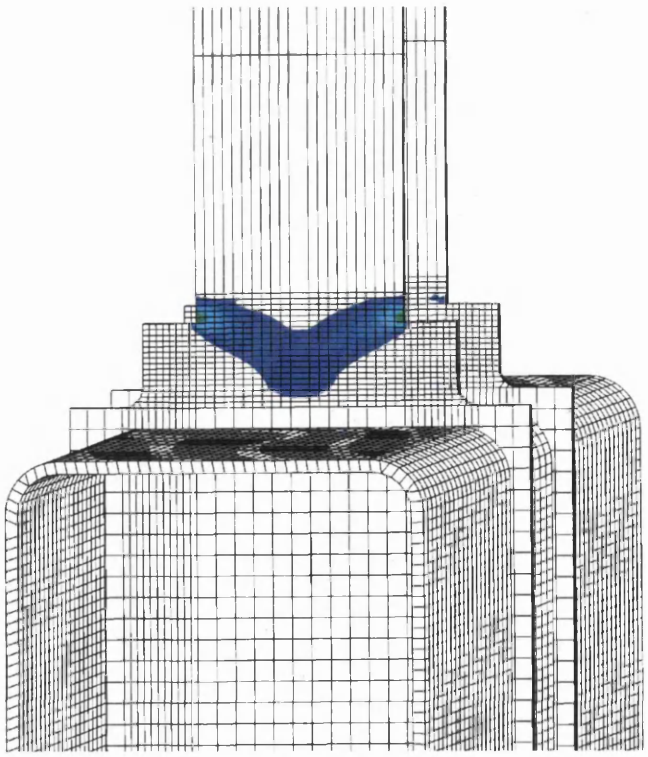

Figure 6.14 T-1 plastic strain distribution

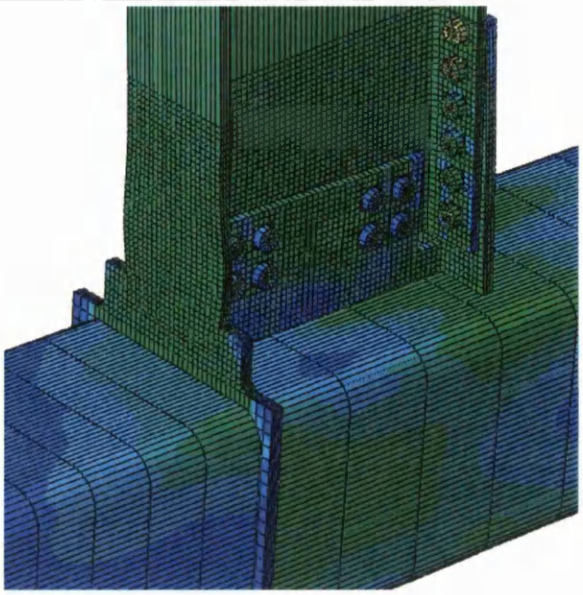

Figure 6.15 FE analyses result of the beam top flange buckling (T-4)

Chapter 7

Parametric studies and Optimization

As stated in Introduction, by weakening the beam section, connection assemblages are found to show excellent plastic deformation capacity. This approach can be done either by cutting a portion of the beam flange (reduced beam section, RBS) or reduce beam web (RBW) connections. Among these methods, the RBS is known to be better. However, this type of connection is relatively costly due to the cutting of flanges at four locations at each end, especially in the presence of floor slabs for rehabilitation purpose. Moreover, in these connections, the cutting of flanges reduces the beam stability and increases the probability of beam lateral torsional buckling. On the other hand, the RBW connections, in which the reductions are made in the beam web, are much less prone to such a problem. Based on these reasons, therefore, the numerical study described in herein is concentrated on RBW connections.

7.1. Introduction

In RBW connections proposed by Aschheim (2000), the beam web was penetrated by a single or multi circular spaces (see Figures 7.1 and 7.2). Although the study showed that the connection can reach the desired ductility (4 percent total rotation) when a relative big space is created at the beam web, this will cause a remarkable reduction in the connection strength. Thus, the purpose of this project is to propose new beam end configurations to increase the RHS column-to-I beam connection strength and ductility. This new beam end configurations are

based on the weakening of the beam section method. In this method, instead of creating a big space at the beam web, numbers of small drilled spaces were created at the beam web.

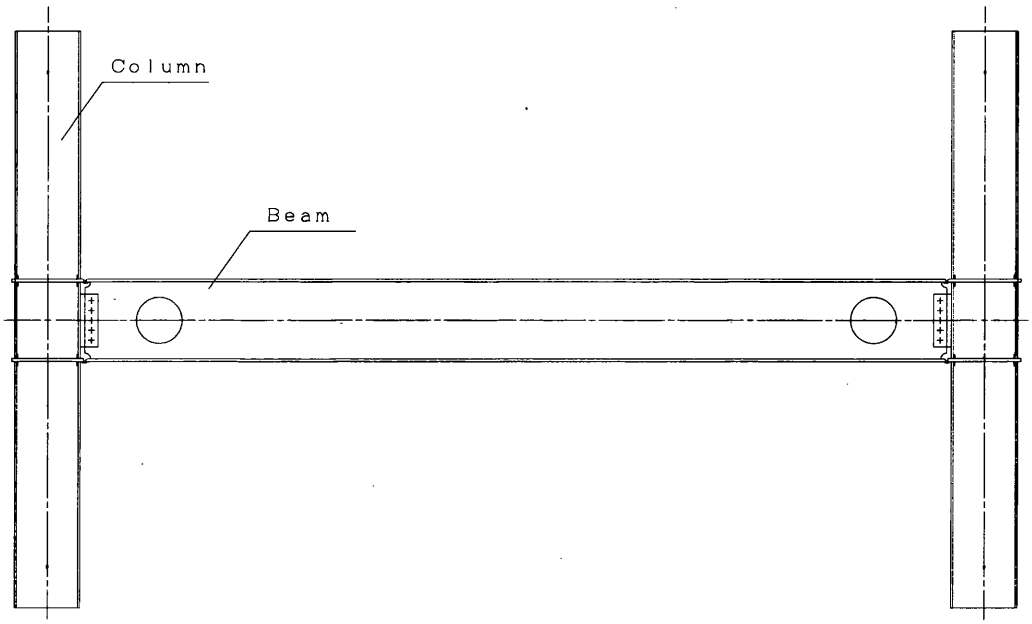

Figure 7.1 RBW connection with single circular space

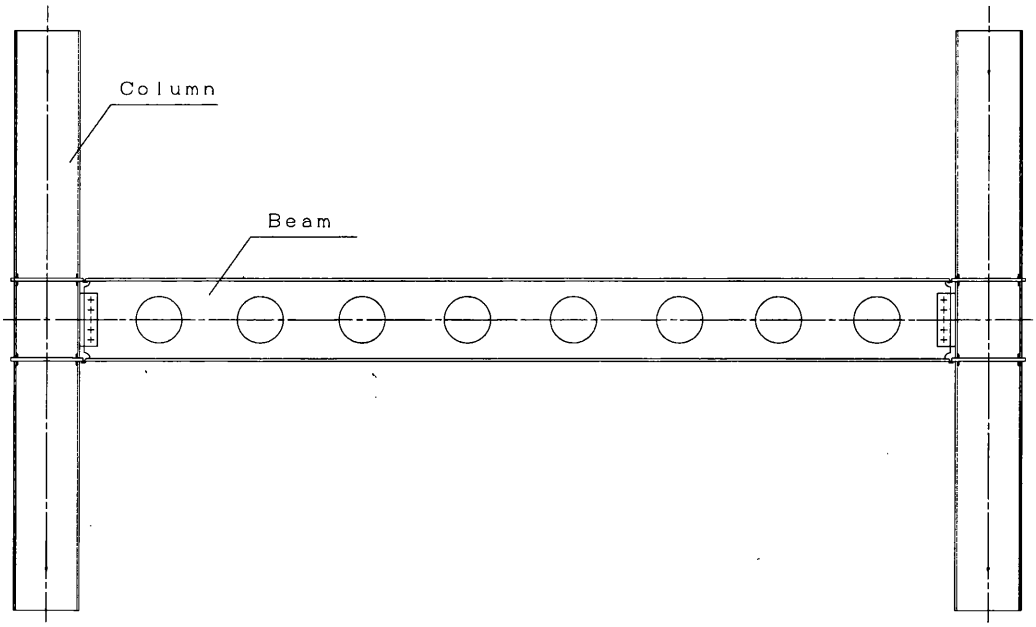

Figure 7.2 RBW connection with multi circular spaces

7.2. RBW Configuration and Variable Parameters

Figure 7.3 shows one of the configurations of RBW connection (Type 1) and Figure 7.4 shows another configuration of RBW connection (Type 2). Taking the type 1 as an example, the reason for proposing this beam end configuration can be explained as follows:

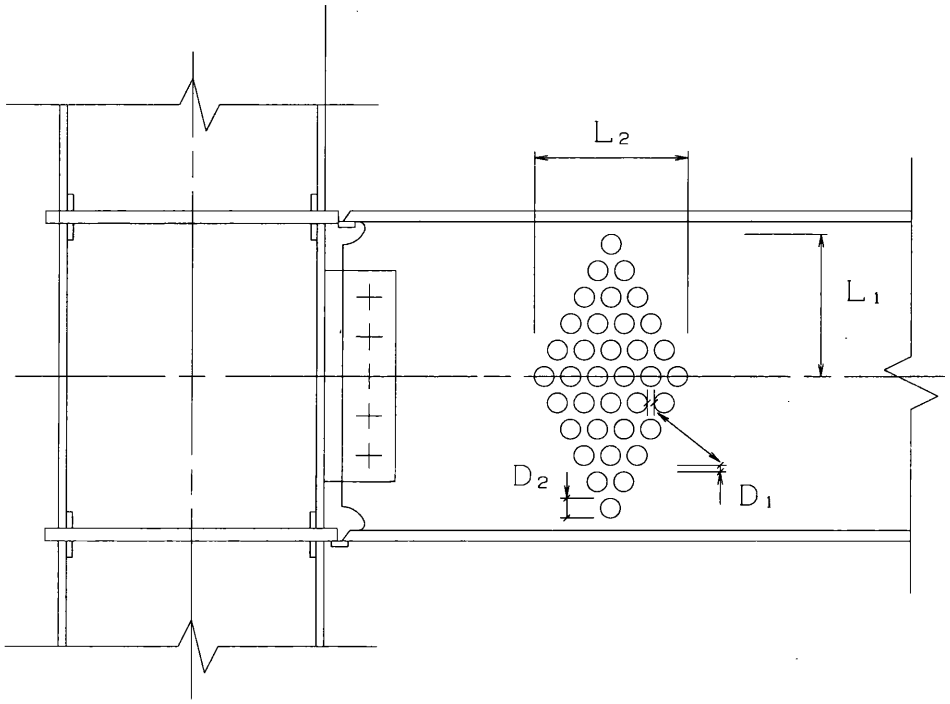

Figure 7.3 RBW connection (type 1)

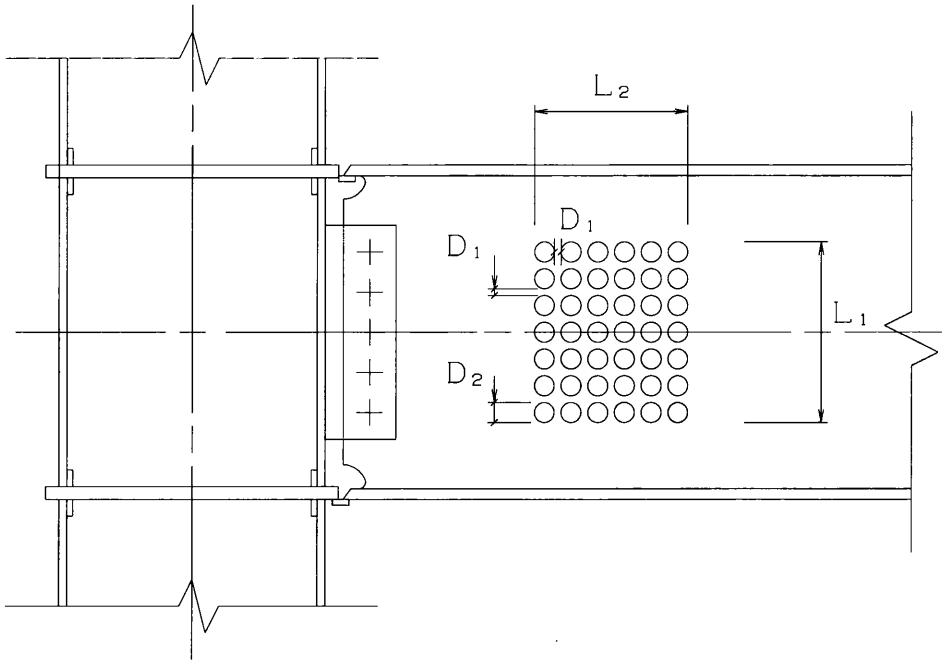

Figure 7.4 RBW connection (type 2)

Figure 7.5 shows the normal strain distribution of a typical RBW connection with a big circular space. This figure clearly shows that for the first part of the beam which is located between the beam tip and the circular space center, there is only one neutral axis. However, for the second part of the beam which is located between the circular space center and the column face, the neutral axis diffuse. This indicates that creating a circular space at the beam web may divide the beam into two beams.

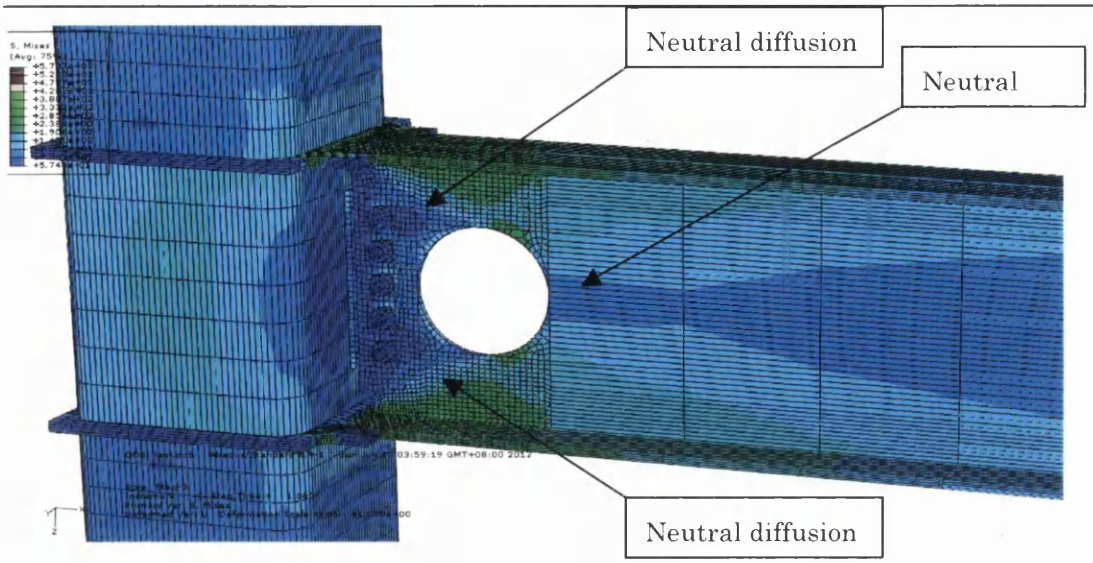

Figure 7.5 Neutral axis of the RBW connection with a big circular space

It might be one of the reasons for why early beam flange fracture appears at the beam flanges at the space area and why this type of connections has low connection rotational stiffness. Therefore, in order to have proper transformation of shear forces from the top beam flange to the bottom flange at the space area, a drilled beam web connection was proposed. Figure 7.6 shows the shear strain distribution along the beam web height of a proposed RBS connection. The figure shows signification shear strain concentration at the beam web between the drilled spaces.

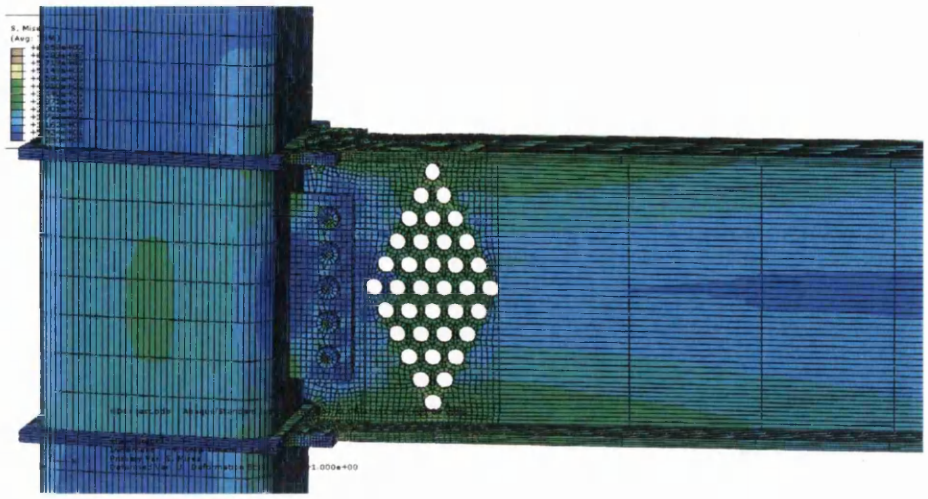

Figure 7.6 Shear strain distribution in proposed RBW connection

Therefore, the diameter, number and clear distance between the drilled spaces can play an important role on connection strength and ductility.

1) Type 1

Figure 7.3 shows the parameters of type 1. A clear distance between drilled spaces was kept as a constant (D_1=10mm). Drilled space diameter was selected as a variable. Totally two parameters were defined, α and ß. The distance between the first and last drilled spaces in horizontal, L_2, was selected to be proportional to the distance between the first and last drilled spaces in the vertical direction, L_1 ($L_1=\alpha \cdot L_2$). See Figure 7.3 for the illustration. Parameter ß is the ratio of the drilled space diameter, D_2, to the clear distance between drilled spaces, D_1 ($\beta=D_2/D_1$). Table.7.1 summarizes all parameters used in this study.

Table.7.1 Summary of parameters (type 1)

Specimens	α	ß	D_1 (mm)	D_2 (mm)	L_1 (mm)	L_2 (mm)
T-2-1	0.79	3	10	30	55	70
T-2-2	0.9	3	10	30	135	150

T-2-3	0.92	3	10	30	175	190

2) Type 2

Figure 7.4 shows the variable parameters of type 2. A clear distance between drilled spaces was kept as a constant (D_1=10mm). Drilled space diameter was selected as a variable. Totally two parameters were defined, α and ß. The distance between the first and last drilled spaces in horizontal, L_2, was selected to be proportional to the distance between the first and last drilled spaces in the vertical direction, L_1 ($L_1=\alpha \cdot L_2$). See Figure 7.4 for detail. Parameter ß is the ratio of the drilled space diameter, D_2, to the clear distance between drilled spaces, D_1 ($ß=D_2/D_1$). Table 7.2 summarizes all parameters used in this study.

Table 7.2 Summary of parameters (type 2)

Specimens	α	ß	D_1 (mm)	D_2 (mm)	L_1 (mm)	L_2 (mm)
T-2-4	0.16	3	10	30	190	30
T-2-5	0.58	3	10	30	190	110
T-2-6	1	3	10	30	190	190
T-2-7	0.11	2	10	20	190	20
T-2-8	0.42	2	10	20	190	80
T-2-9	0.9	2	10	20	190	170

7.3. Finite Element Results and Discussion

7.3.1. Failure Modes

One of the important failure modes analyzed in FEM is the beam flange fracture. The location of beam flange fracture depends on the parameters α and ß. By increasing parameters α and ß, a larger energy dissipation capacity can be

achieved, resulting in the strain concentration decrease at the weld access hole (beam cope). As a result, it makes the beam flange fracture away from the column face which is a desirable failure mode. The drilled spaces in the beam web (RBW connection) cause the plastic strain to move into the beam span and the plastic hinges form away from the column face (see Figures 7.7, 7.8 and 7.9).

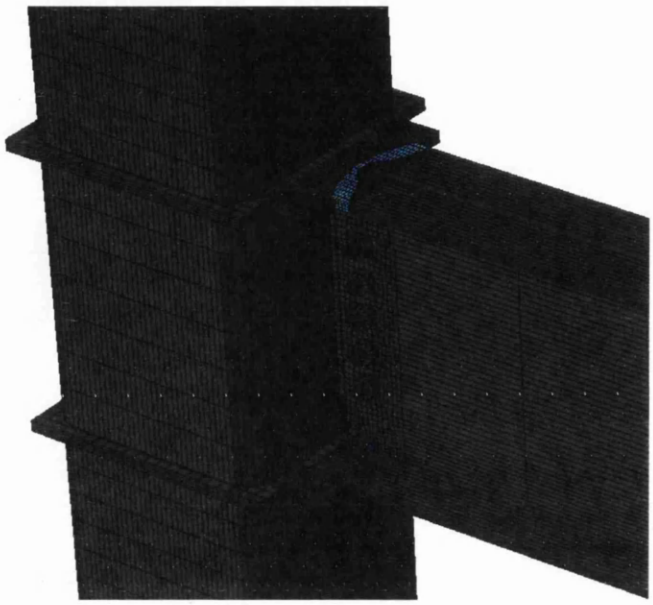

Figure 7.7 Failure mode in weld access hole area (without RBW connection)

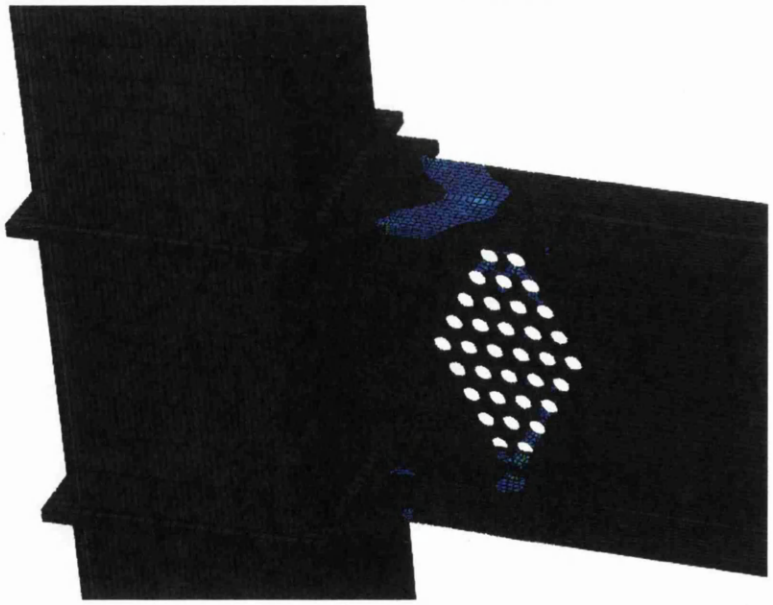

Figure 7.8 The beam flange fracture at beam span area (RBW connection, type1)

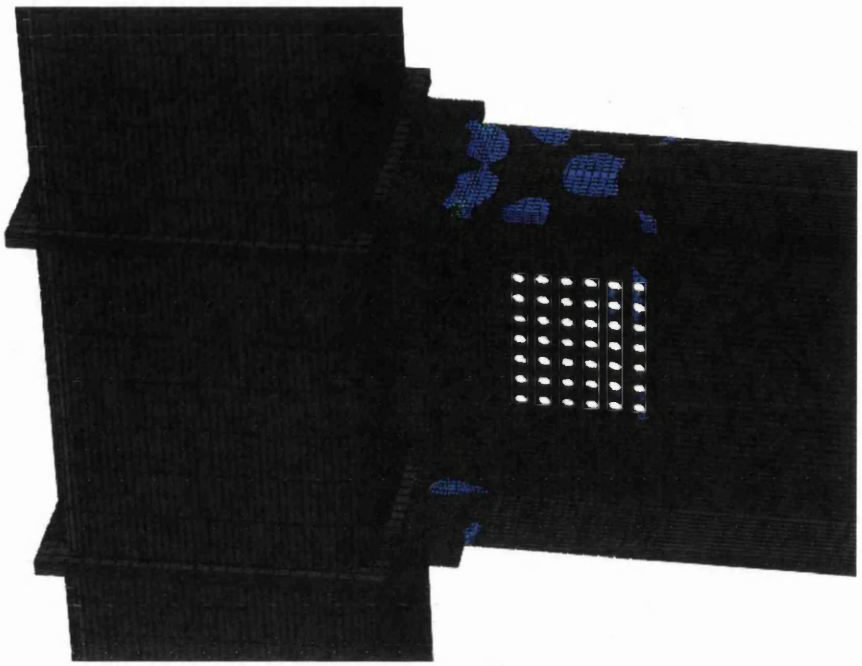

Figure7.9 The beam flange fracture at beam span area (RBW connection, type2)

7.3.2. Effect of Drilled Space and Parameters

The ductility of connection can be represented by the sum of rotation caused by moment at the column face (see Figures 7.10 to 7.12). Based on the most of seismic codes, the minimum required value for this parameter is 0.04. For the configuration type1, Figure 7.10 shows that the ductility of connection increases as the parameter α increases. The rotations for specimens are presented in Table.7.1, where parameters (α) are 0.79, 0.9 and 0.92, are 0.059, 0.063 and 0.069 respectively.

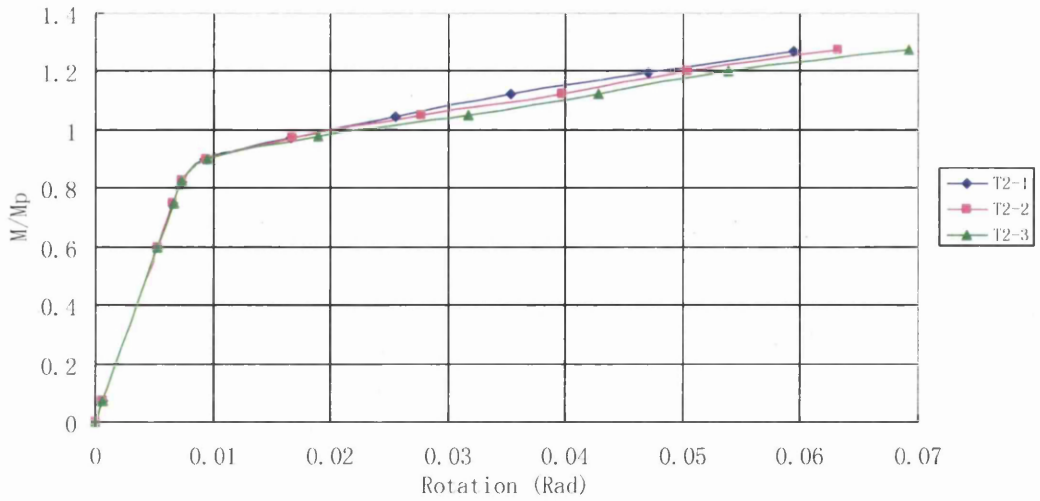

Figure7.10 Moment-rotation curves (type 1)

For the configuration type2, Figures 7.11 and 7.12 show that the ductility of connection becomes increase as the parameter α increases. The rotations for specimens are presented in Table 7.2, where parameters β =3 and α are 0.16, 0.58 and 1, are 0.068, 0.07 and 0.073 respectively; and β =2 and α are 0.11, 0.42 and 0.9, are 0.068, 0.069 and 0.071 respectively. Comparing between β =2 and β =3 is shown in Figure 7.13.

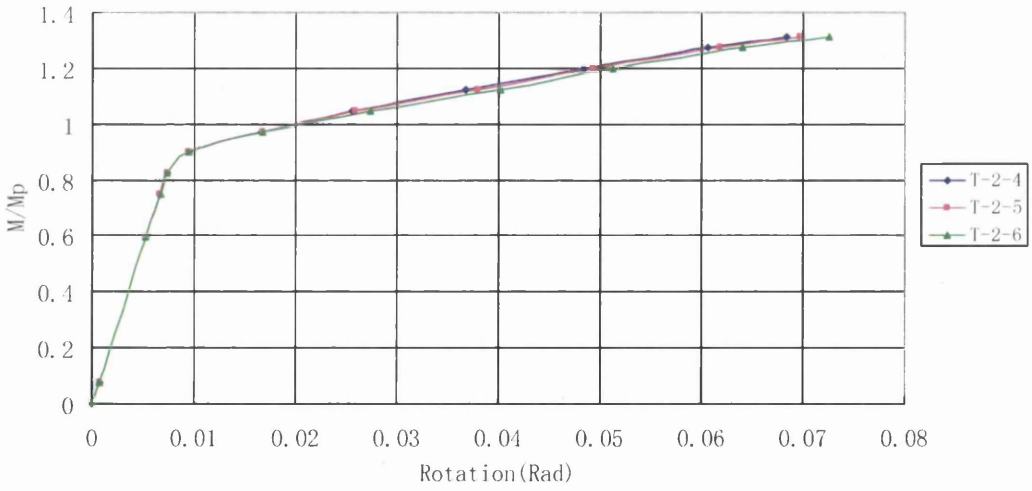

Figure 7.11 Moment-rotation curves (type 2), β =3

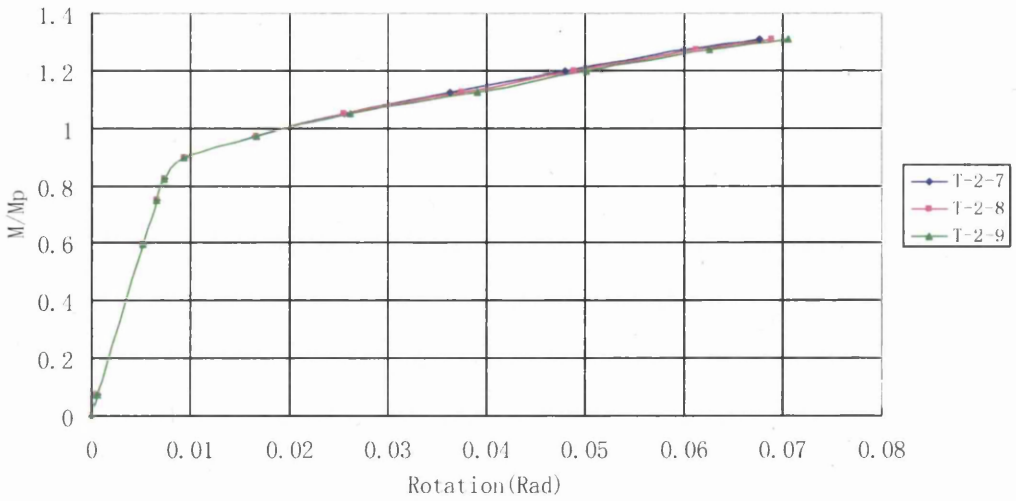

Figure 7.12 Moment-rotation curves (type 2), β =2

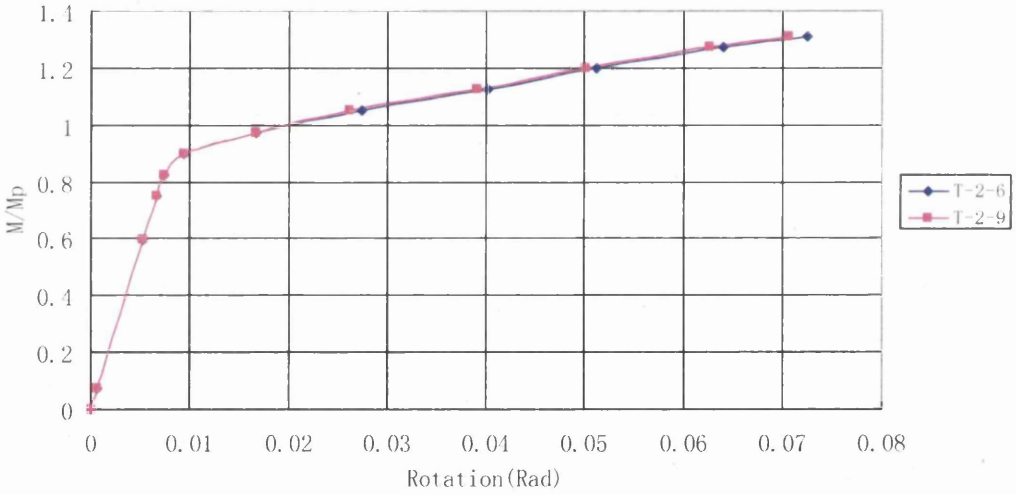

Figure 7.13 Comparing moment-rotation curves β =2 and β =3

Connection strength can be evaluated by the ratio of the connection moment at failure time to the beam plastic moment capacity (M/M_p). The ratio value specified in AIJ (Architectural institute of Japan) Recommendation (1997) is greater than 1.25 and Eurocode 3 (CEN 1994) recommends greater than 1.3. However, in all cases, the ratio of M/M_p for all specimens is greater than 1.25,

roughly 1.3, and increase as the parameters α and β increase.

As mentioned above, the proposed RBW connections have higher ductility with bigger values of the parameters α and β. From economical point of view, the biggest space size drilled by most of fabricators is around 30 mm which is corresponded to ß equal to 3. The value of parameter α is decided by the height of beam. For example, the parameter α equal to 1 means the horizontal distance L_2 equal to the vertical distance L_1. The horizontal distance L_2 can increase along the length of beam web, but the vertical distance L_1 is limited by the height of beam web. To avoid the web buckling, when L_1 takes the maximum, L_2 should be equal to L_1. This means $\alpha = 1$.

Although the two types of configuration can obtain the same results in weakening the beam section, in my opinion, the configuration type 1 is better than 2. Because the drilled spaces of beam web gradually increases toward the beam tip as shown in Figure 7.3 so that the plastic hinge forms gradually within the beam span.

7.4 Conclusion

This study was based on weaken beam section method described in Chapter 2. For this propose, a number of drilled space were created at the beam web at the vicinity of column face. Finite element results showed that the drilled space increased the connection ductility and cause plastic hinge away from the column face, moving into the beam span. Although only two configurations of RBW connections are studied in this Chapter, it provides a way to develop some new design concepts.

Chapter 8

Results and Discussions

The finite element method studies of improved welded joints have been completed in the last Chapter. In this Chapter, we will discuss how to derive design equations to evaluate ultimate strength of connections. It is found that the ultimate moment capacity of such welded joint can be predicted by simple formulas based on elementary plastic analysis. The optimum length of such welded joint for avoidance tensile failure can be decided.

8.1 Dissipated Energies of Specimens

Table 8.1 shows the cumulative plastic deformation factors for each specimen. See Appendix 2 for the definition of cumulative plastic deformation factor η.

Table 8.1 Cumulative plastic deformation factors

Specimen	T-1	T-2	T-3	T-4
η	63	63	73	120

These factors are significantly larger than the average value of the factors obtained in the past large-scale tests (AIJ Kinki 1997). Especially for specimens T-3 and T-4 that failed by local buckling, the cumulative plastic deformation factors are comparable to all the specimens. The cumulative plastic deformation factors are plotted against the beam rotation θ_m, non-dismensionalized by θ_p (θ_p : the elastic beam rotation at M_p) for the specimens in Figure 8.1.

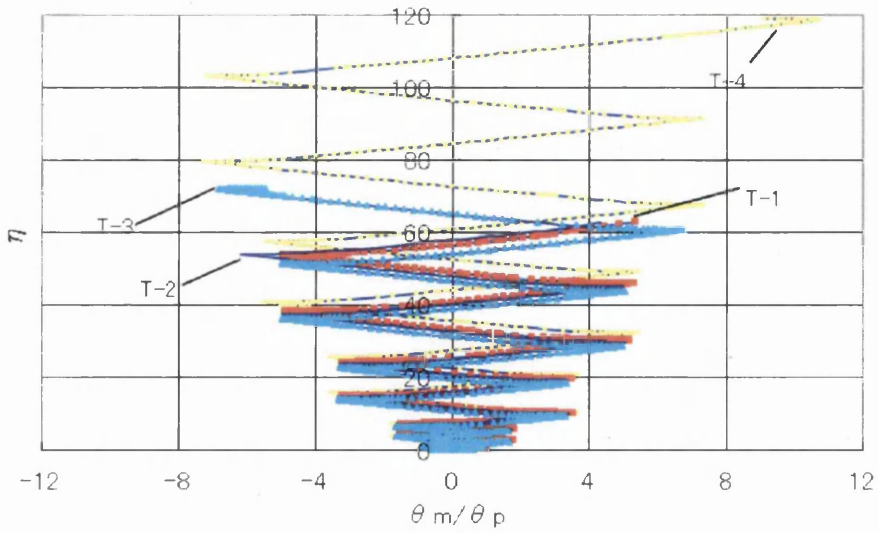

Figure 8.1 Cumulative plastic deformation factor

Specimen T-3 has welded joints at both the top and bottom flanges, while specimen T-4 has welded joint at the top flange and bolted joint at the bottom flange. Since the pattern of hysteretic loops is different between each specimen (See Chapter 3), comparison is made of the deformation capacities between the specimens in terms of dissipated energy. The definition of dissipated energy is shown in Appendix 2. The area below the hysteresis curve represents the dissipated energy. However, since the area below an elastic unloading envelope represents the energy stored in the structure, this area is regarded as the negative dissipated energy. The dissipated energies, nondimensionalized by $M_p\theta_p$ (M_p: full plastic moment of beam, θ_p: the elastic beam rotation at M_p) are plotted against the accumulated beam rotation $\Sigma\theta_m$ for the four specimens in Figure 8.2, where $\Sigma\theta_m$ denotes the sum of rotations caused by either the positive or negative moments.

It is interesting to see that dissipated energies at the same value of $\Sigma\theta_m$ are almost identical for both conventional and improved types. However, the final dissipated energies are much greater for the improved type (T-3 and T-4) than for the conventional type (T-1 and T-2).

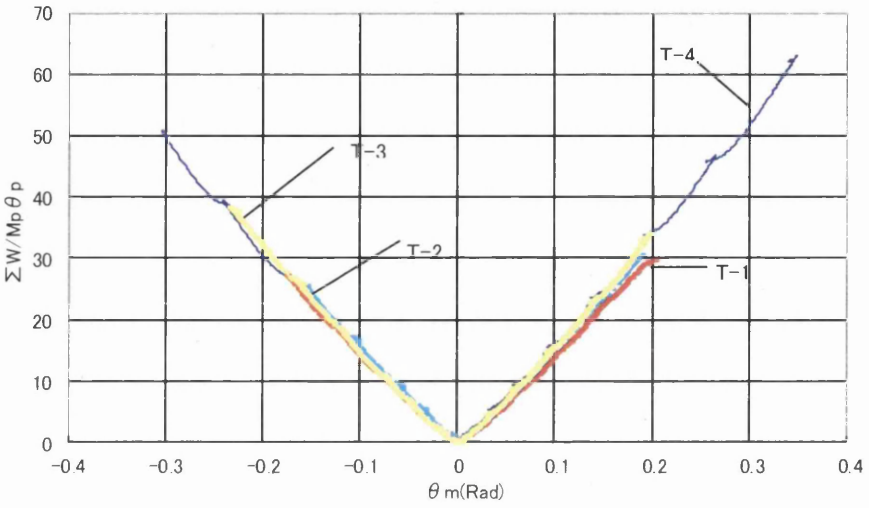

Figure 8.2 Cumulative plastic deformation factor based on dissipated energies

8.2 Evaluation of Ultimate Strength of Connections

Two failure modes were identified in the connection test described in the Chapter 3, which included the tensile failure of beam flange at the beam end and the local buckling of plate element at the beam end. Several experimental evidences and formulas are available for the evaluation of the ultimate strength of the ultimate strength of these connections corresponding to each of these failure modes.

The axial loads in the top and bottom flanges at the beam end are not equal in magnitude. The unbalanced axial load is carried by the beam web to the column flange joint. However, the ultimate moment carried by the flanges ${}_fM_u$ is

evaluated as the axial capacity of one of the beam flange-to-column flange joints multiplied by the distance between the centroids of the top and bottom flange to column joints. This simplified assumption gives lower bound solutions of simple plastic analysis. The beam web joints are in general flexible and do not carry a large axial load.

8.2.1 Tensile Strength of Welded Joints

Failure modes of specimens classified into 2 groups, which included the local buckling of plate element at the beam end and the tensile failure of beam flange at the beam end. First, cracks were found either at the tip of the weld toes or at the toe of beam copes. Then, these cracks propagated gradually with load increase and finally led to tensile failure of the beam flange. The fracture paths are shown in Figure 8.3

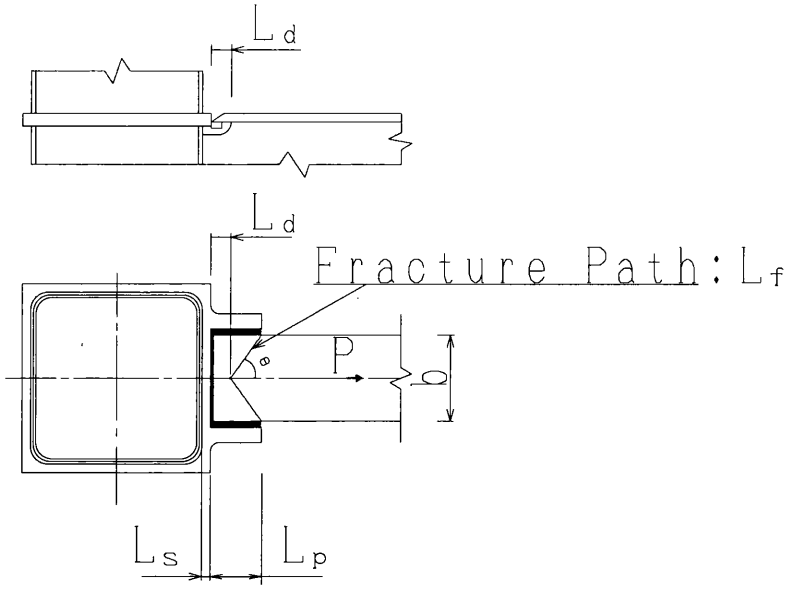

Figure 8.3 Fracture Paths at beam end

To predict the ultimate tensile strength of the welded joints, two fracture paths are proposed as follows (see Figure 8.4). L_p signifies the length of the welded joint,

L_d signifies the space between the toe of beam cope and the beam end, L_s signifies the space between the beam end and column face, b denotes the width of the beam flange and b_e denotes the width of the welded joint.

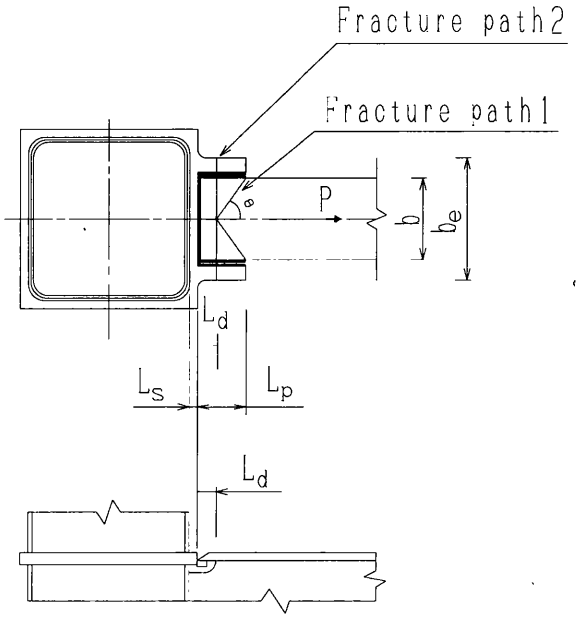

Figure 8.4 Proposed fracture paths at the beam end

The following formula is given to calculate the tensile strength of each fracture path when failure occurs by ductile tear along the fracture path (Fracture path1)

$$P_u = L_f \times t_f \times (\sin\theta + \frac{\cos\theta}{\sqrt{3}}) \times \sigma_{f,u} \tag{8.1}$$

where L_f denotes the length of fracture path and $\sigma_{f,u}$ is the beam flange ultimate tensile strength, t_f is the thickness of beam flange, and θ is the fracture angle (see Figure 8.3).

Therefore, the flexural capacity of the beam at the column face ${}_fM_u$ is given as:

$$M_{f,u} = [b \times t_f \times \sigma_{f,u} + \frac{2}{\sqrt{3}}(L_p - L_d) \times t_f \times \sigma_{f,u}] \times \frac{J^1{}_b \times L}{L_h + L_t} \tag{8.2}$$

where J^1_b is the distance between the top flange-to-column joint and the bottom flange-to-column joint, which is given by:

$$J^1_b = H_b - t_f \tag{8.3}$$

for specimens T-1, T-2 and T-3, where H_b is the height of the beam, and by

$$J^1_b = H_b - \frac{t_f}{2} + \frac{t_{pl}}{2} \tag{8.4}$$

for specimen T-4, where t_{pl} is the thickness of flange plate.

In general, the fracture path 2 is much stronger than the fracture path 1 and thus such a fracture needs not to be considered. However, to ensure a sufficient over-strength to prevent tensile failure, the optimum length of such welded joint can be calculated as

$$L_p = L_d + \frac{\sqrt{3}}{2}(b_e - b) \tag{8.5}$$

The flexural capacity of bolted web connection in specimens T-2, T-3 and T-4 can be neglected because of large flexibility of the connection due to the bolt slip and local yielding of the column flange. However, specimen T-1 has a welded web joint, and the bending moment carried by this joint is added to the moment given by equation (8.2) to evaluate the ultimate flexural capacity of connection. Tanaka,J (AIJ 1996) proposed the following formula for the flexural capacity,

$$M_{w,u} = (x - S_v)(H_b - t_f - x - S_v) f_w \tag{8.6}$$

where x is obtained by a yield line analysis and is given by

$$x = \left(\frac{t_c^2 (H_b - t_f)\sigma_{w,y}}{f_w} + S_v^2 \right)^{1/2} \tag{8.7}$$

in which t_c is the thickness of the column, S_v is the vertical space of the beam

cope (see Figure8.5), and f_w is the stress and is given as the smaller of the following two values,

$$f_w = t_w \sigma_{w,y}, \quad f_w = \frac{2}{\sqrt{3}} t_c \sigma_{c,y} \tag{8.8}$$

where t_w denotes the thickness of the beam web, $\sigma_{w,y}$ is the yield strength of the beam web, and $\sigma_{c,y}$ is the yield strength of the column.

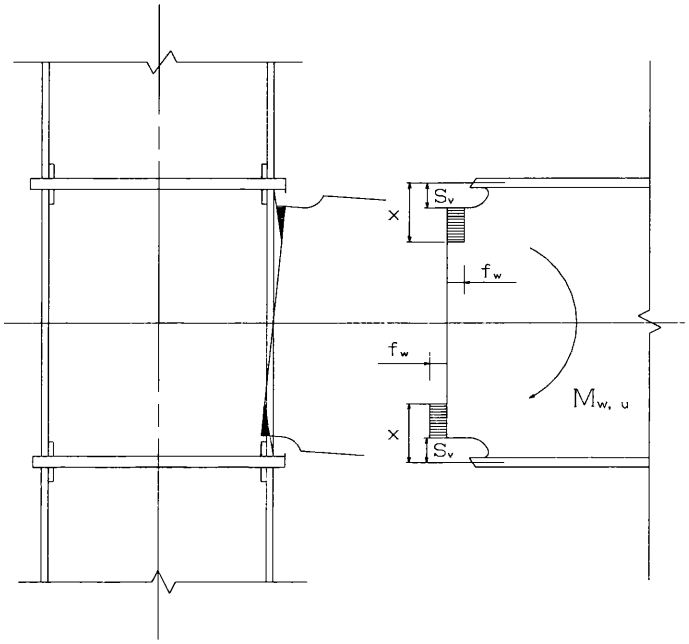

Figure 8.5 Moment carried by welded web joint

The ultimate flexural capacities $_{End}M_u=M_{f.u}$ or $_{End}M_u=M_{f.u}+M_{w,u}$ of beam-to-column connections determined by tensile capacities of the welded joints at the beam ends are summarized in Table 8.2 and compared with the test results. This table shows that the predictions agree well with the test results except for specimens T-3 and T-4, because these two specimens failed by local buckling.

Table 8.2 Ultimate moment governed by tensile capacities of welded joints at flange ends

Specimen	Test	Prediction	

	M_m (kN.m)	L_d	$M_{w,u}$ (KN-m)	End M_u(kN.m)	M_m / End M_u
T-1	830	34	55	836	0.97
T-2	830	43		854	0.99
T-3	880	43		1034	0.85
T-4	864	7		939	0.92

Note: 1) M_m is the maximum moment attained when the welded joints are under a tensile load. Specimens T-3 and T-4 failed in failure modes different form tensile failure of welded joints. 2) η denotes the cumulative plastic deformation factor.

8.2.2 Local Buckling of Plate Elements

Based on a series of stub-column tests of wide flange sections, Kato et al. (1994) proposed the following formula that gives the maximum moment M_{max} at the beam end, non-dimensionalized by the full-plastic moment M_p , when the beam end moment is governed by local buckling of place elements.

$$\frac{1}{\alpha} = \frac{0.4896}{\alpha_f} + \frac{0.0460}{\alpha_w} + 0.7606 \tag{8.9}$$

with

$$\alpha_f = \frac{E}{\sigma_{f,y}} \times \left(\frac{t_f}{b/2}\right)^2 \tag{8.10}$$

and

$$\alpha_w = \frac{E}{\sigma_{w,y}} \times \left[\frac{t_f}{(H_b - 2t_f)}\right]^2 \tag{8.11}$$

where α represents M_{max}/M_p; α_f denotes local buckling parameter of beam flange; α_w denotes local buckling parameter of beam web, E is elastic modulus; $\sigma_{f,y}$ denotes the measured yield strength of beam flange, and $\sigma_{w,y}$ denotes the measured yield strength of beam web.

The values of α are compared with the maximum moments at the section where the haunch starts in Table 8.3. The predictions based on experiment indicate that local buckling was found earlier than the ultimate limit state. The above results support the experimental observations that the welded joints of specimens T-3 and T-4 had sufficient over-strength and that these connections failed by local buckling of the flanges.

Table 8.3 Moment capacities determined by local buckling

Specimen designation	Test					Prediction
	M_{max} (kN.m)	M_p (kN.m)	M_{max}/M_p	α_f	α_w	α
T-3	827	645	1.29	16.54	13.15	1.26
T-4	833	645	1.29	17.43	13.49	1.26

Note: 1) M_{max} was determined by local buckling only for specimens T-3 and T-4. 2) M_p was calculated using the measured dimensions and material properties.

8.3 J Integral Method for Evaluation Through Crack in RHS Column-to- I Beam Connection

During the earthquake, many of steel structures are damaged due to the crack initiation and propagation. For avoiding premature occurrences of brittle fracture, a series of tests were conducted on an improved RHS column-to-I beam

connection. The aim of the tests was to find possible solutions for avoiding premature occurrences of brittle fracture in RHS column-to-I beam connections (see Chapter 3). One of the important failure modes observed in this test is tensile failure of the beam flanges. First, cracks are found either at the tip of the weld toes or at the toe of beam copes. Then, these cracks propagate gradually with load increase and finally lead to tensile failure of the beam flange. The fracture paths are shown in Figure 8.6

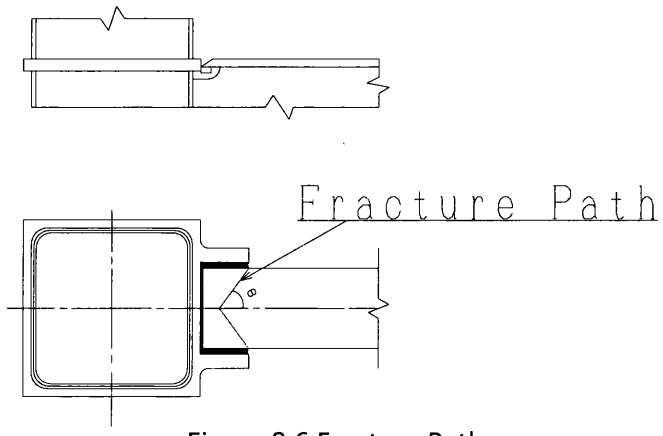

Figure 8.6 Fracture Paths

In the modified Central Electricity Generating Board (CEGB) approach (Harrison et al. 1976), the ultimate collapse load and the crack driving force of cracked structures are used as two assessment parameters. Usually, the J-integral represents the crack driving force for the crack growth. With the emergence of readily available simple J solutions for various types of structures through J estimation techniques, J-integral-based elastic-plastic fracture mechanics has become a common tool for analyzing ductile materials. In this J estimation method (Kumar et al. 1981), elastic-plastic J-integral solutions are estimated as the sum of a linear solution for an effective crack length and a fully plastic solution based on the nonlinear Ramberg-Osgood power hardening law.

The linear elastic solution for a crack in RHS column-to-I beam connection is obtained by taking the solution for the plane plate and the h_1 function in the fully plastic solution in calculated by the finite element analyses. For a through crack in the RHS Column-to I beam joint, the combined elastic-plastic J solution can be written as:

$$J = J^e(a_e) + J^p(a,n) \tag{8.12}$$

where J^e signifies the elastic solution for an effective crack length a_e, J^p is the fully plastic solution.

Equation 8.12. is derived from the deformation plasticity theory, in which a Ramberg-Osgood power hardening law is used as the material model, which is described as:

$$\frac{\varepsilon}{\varepsilon_0} = \frac{\sigma}{\sigma_0} + \alpha \times (\frac{\sigma}{\sigma_0})^n \quad \varepsilon_0 = \frac{\sigma_0}{E} \tag{8.13}$$

where σ is the Mises stress, ε is the strain, αis the material constant, n is the power hardening exponent, E is Young's modulus, and ε_0 is the reference strain, σ_0 is the initial yield stress

$J^e(a_e)$ is the elastic part of the solution, and can be obtained from the following equation

$$J^e(a_e) = \frac{K_I^2}{E} \tag{8.14}$$

where K_I is the stress intensity factor (SIF), and is described as:

$$K_I = \sigma \times \sqrt{\pi a} \times \sin^2 \theta \tag{8.15}$$

where a and θ are geometric sizes, σ is the applied stress, as shown in Figure 8.7

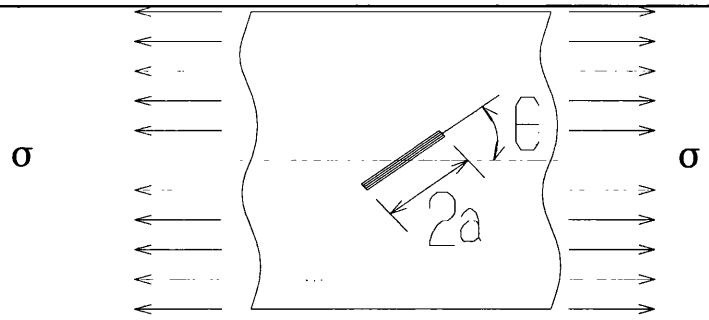

Figure 8.7 A plane plate under the uniform stress

The effective crack length was modified by Irwin, and is given by:

$$a_e = a + \phi \times r_y$$

where

$$r_y = \frac{1}{\beta\pi}\frac{n-1}{n+1}\frac{K_J^2}{\sigma_0}$$

$$\phi = \frac{1}{1+(\frac{P_1}{P_0})^2}$$

ß=2 (plane stress), or 6 (plane strain)

P_1 signifies an applied load and P_0 is the limit load for a non-cracked RHS Column to I beam connection. In this case, P_0 signifies the limit load of beam flange, given by (Kumer et al 1981)

$$P_0 = 1.071 \times \eta \times c \times t \times \sigma_0 \qquad (8.16)$$

where

$$\eta = [(\frac{2a}{c})^2 + 2\times(\frac{2a}{c}) + 2]^{\frac{1}{2}} - (\frac{2a}{c} + 1)$$

in which c is the geometric size (see Figure 8.8), t is the thickness of the beam flange.

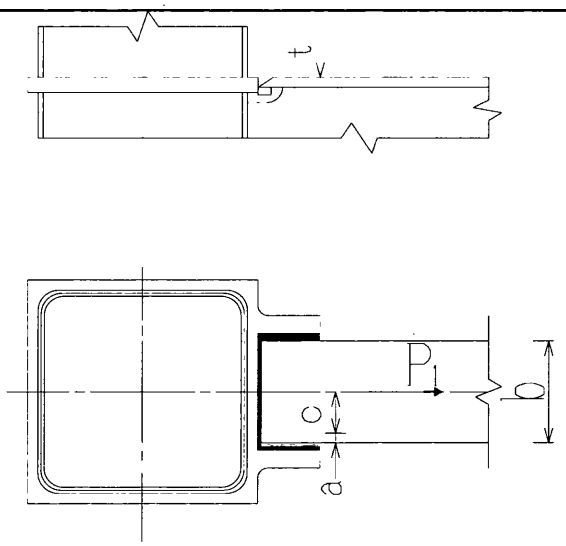

Figure 8.8 New RHS Column –to I beam Joint

The plastic part of the solution, J^p, can be obtained from the following equation

$$J^p(a,n) = \alpha \times \sigma_0 \times \varepsilon_0 \times h_1(\frac{a}{t}, n) \times (\frac{P_1}{P_0})^{n+1} \qquad (8.17)$$

where h_1 is the function of material and geometry and will be determined from the elastic-plastic J-integral in FE analyses.

Combining Equations 8.14 and 8.17, elastic-plastic J can be obtained.

Chapter 9

Conclusions and Future Work

9.1 Conclusions

• A FE analysis of the behaviour of the new RHS column-to-I beam connections has described in this thesis. Four test specimens are simulated. The model includes the individual beams, columns, diaphragms, bolts, fin plate and the complex contact surfaces. Material nonlinearity is considered for all components. These are complex models. Contacts are critical to model the bolted connection behaviour of the joint. Contact elements have been used at the bolt-hole and also at the surface between the web of the beam and fin plate, taking into consideration friction between the surfaces. Three-dimensional brick elements are used as this type of element is easily adapted to model interfaces between the connecting surfaces. The compassion shows a good correlation between the FE and experimental results of the connection behaviour. This proves that the FEM is capable of accurately predicting RHS column-to-I beam connection behaviour. For partially restrained column-to-beam connections, the moment-rotation curves are of great importance for designers, however, in the past, these curves only obtain from the experiments in combination with an analytical approach. Along with the development of finite element method, moment-rotation behaviour can be obtained from numerical methods.

• Finite element results show that RBS connections force the plastic hinge away from the column face, meanwhile, increase the connection ductility without significant reducing the connection strength. Thus, using this type of connections may be avoided premature occurrence of brittle fractures. This provides a way to develop some new design concepts. In practical application, this type of connections can be easily applied to existing building rehabilitation with no need to break of the concrete slab.

• The ultimate moment of beam to column joints with improved welded joint can be estimated by equation (8.2), so far as ductile behavior is achieved. This ultimate moment should be large enough such that the moment at the start of welded joint reaches αM_p. The value of α should be greater than the value given by equation (8.9). The value of α most frequently is 1.2~1.4. When bolted flange plate connections are used in combination with such welded joints, it is recommended that the flange plate connection have the ultimate strength equal to or slightly greater than that of the welded joints. Further, it is desirable that the flange plates be designed to be wider and thicker than the beam flanges at the welded joints to the column. The cross-sectional area of the flange plate in specimen T-4 was greater than this of the beam flange by about 36 percent. This is to provide for the lower reliability of welded joints between the internal diaphragm and the column.

• All the specimens in this study were fabricated using beam copes with conventional profiles, but the specimens did not occur the premature failure. In specimens T-1 and T-2, these cracks extended in a ductile manner and led to tensile failure at the beam ends. In specimens T-3 and T-4, in which the welded

joint are sufficiently long, these cracks extended only by 2mm, when failure occurred by local buckling of the beam flanges. The cumulative plastic deformation factors were significantly greater than the values to be achieved by conventional connections (see table 8.1). Since the improved connections (T-3 and T-4) have such a detail that fracture of beam flange is difficult to take place. This may be the reason why brittle fracture was prevented at least in the specimens tested.

9.2 Future Work

The study described herein concerns for avoidance premature occurrences of brittle fracture in RHS column-to-I beam connections under the influence of strong ground motions. One of the feasible ways to overcome these problems of the insufficient plastic deformation capacity of connections may be found in the improvements of present connection design and fabrication practices by adopting better connection details, welding procedures and material. Although this approach appears to be successful in laboratory testing, one inevitable question lies in the quality control of fabricated structures. It is therefore important to establish reasonable fitness-for-purpose criteria for welded structures so that these criteria are applied to new constructions. Along with the development of the finite element method, applicability of semi-empirical fracture mechanics approaches, such as the failure assessment diagrams, these criteria are now under study. Thus, the future works are concentrated on these aspects.

Appendix 1

Tensile uniaxial test

All the tensile uniaxial tests were taken from one section of the beam and column.

1. Specimen

According to Japanese industrial standards (JIS), the specimens were made in the following Figure

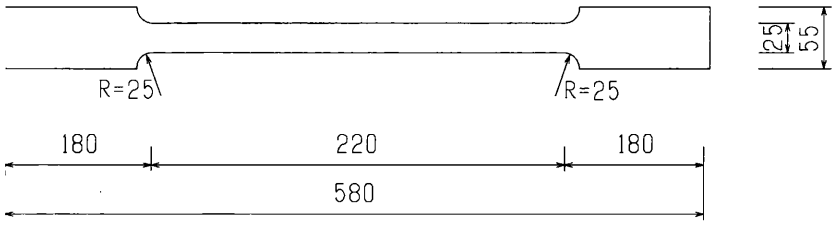

Figure 1 the detail of specimen (mm)

2. Location of specimen

Figures 2～3 show the locations of the specimen taken from the beam/column. B represents the beam, B1～B3 are the top flange of beam, B4～B6 are the beam web, and B7～B9 are the bottom flange of beam. C represents the column.

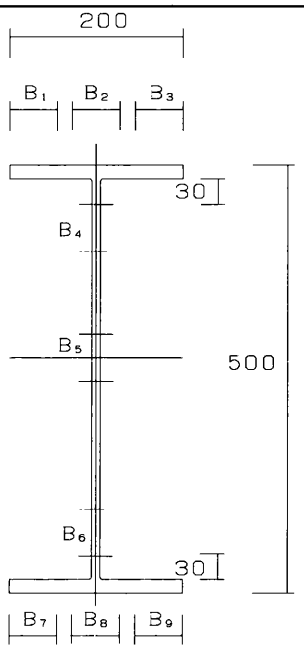

Figure 2 location of specimen (mm)

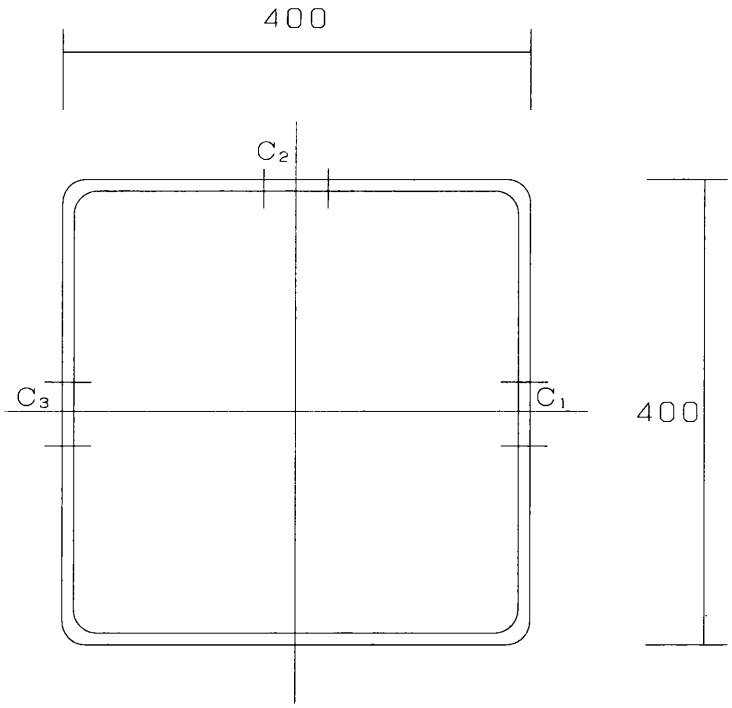

Figure 3 location of specimen (mm)

3. Test result

Table 1 shows the test results taken from the tensile unixial tests. The stress-

strain relationships for specimens are shown in Figure4~10. P16 represents the shear tab and P19 represents the flange plate.

Table 1 Mechanical properties of materials

Specimens	Width (mm)	Thickness (mm)	Cross sectional Area (mm^2)	Modulus of E (kn/mm^2)	Yield stress (n/mm^2)	Ultimate stress (n/mm^2)	Elongation (%)
C1	25	11.39	284.69	214	340	440	24
C2	25	11.44	286.04	208	339	464	20.2
C3	25	11.42	285.46	206	335	441	20
Average	25	11.42	285.40	210	338	448	21.4
B1	25	15.56	389.04	214	315	469	24.7
B3	25	15.5	387.39	212	312	457	23.3
B7	25	15.15	378.63	214	316	461	27.1
B9	25	15.58	389.56	211	309	463	23.7
Average	25	15.45	386.16	213	313	462	24.7
B2	25	15.67	391.71	212	297	457	24
B8	25	15.92	398.03	213	300	460	25
Average	25	15.79	394.87	213	298	459	24.7
B4	25	9.78	244.41	208	322	463	26.3
B5	25	9.66	241.4	211	355	482	22.4
B6	25	9.74	243.55	211	314	467	29.7
Average	25	9.72	243.12	210	331	471	26.1
P16	25	15.96	398.97	207	311	467	24.7
P19	25	18.62	465.59	212	278	406	29.3

In the following stress-strain curves, σ denotes engineering stress; μ is engineering strain (10^{-6}).

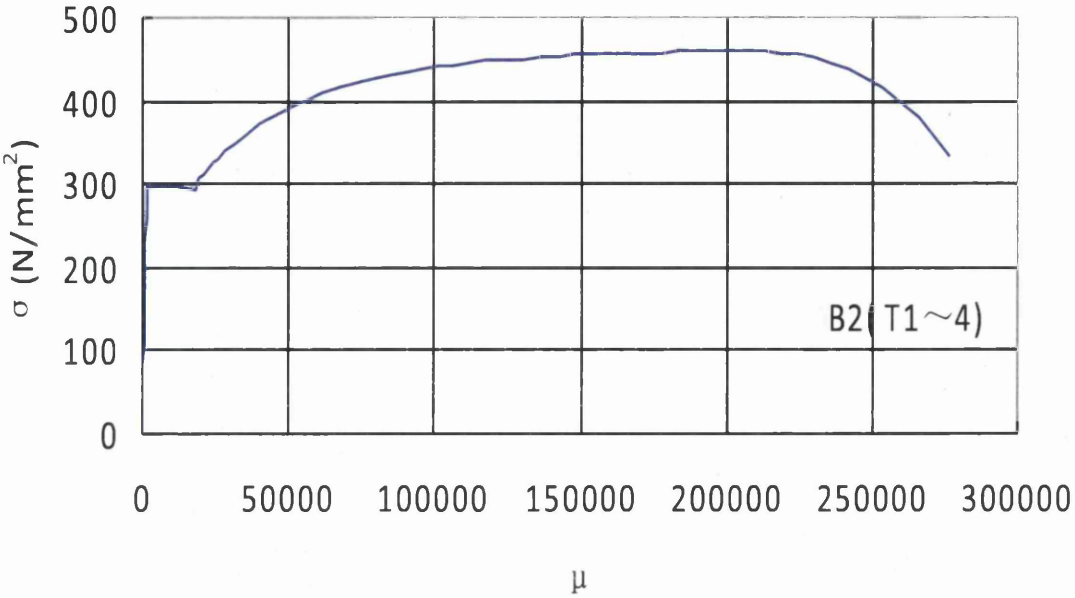
500
400
300
200
100
0
σ (N/mm²)
B2(T1～4)
0
50000
100000
150000
200000
250000
300000
μ

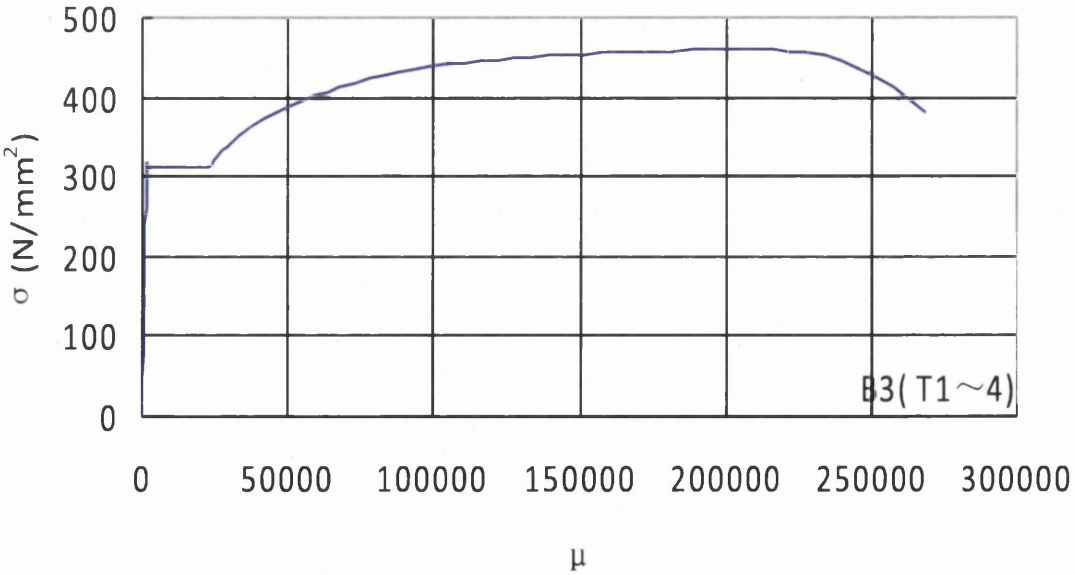
500
400
300
200
100
0
σ (N/mm²)
B3(T1～4)
0
50000
100000
150000
200000
250000
300000
μ

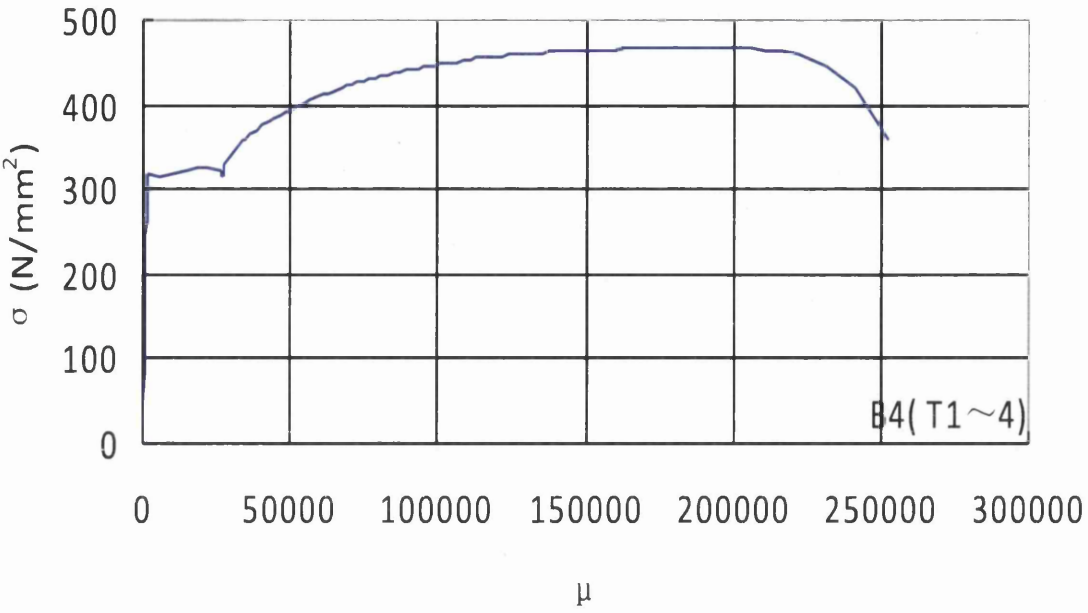
500
400
300
200
100
0
σ (N/mm²)
B4(T1～4)
0
50000
100000
150000
200000
250000
300000
μ

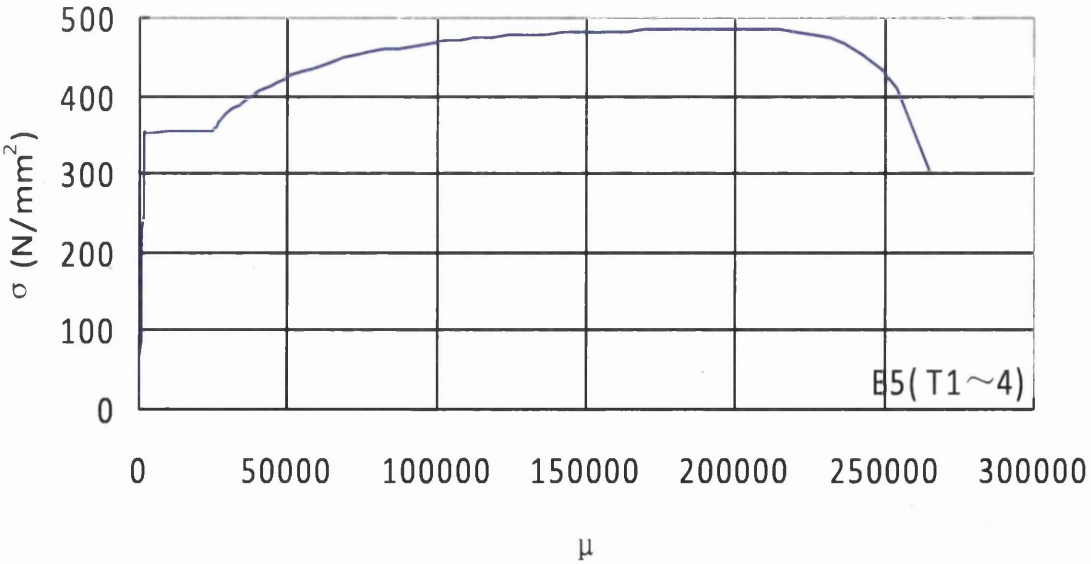
500
400
300
200
100
0
σ (N/mm²)
B5(T1～4)
0
50000
100000
150000
200000
250000
300000
μ

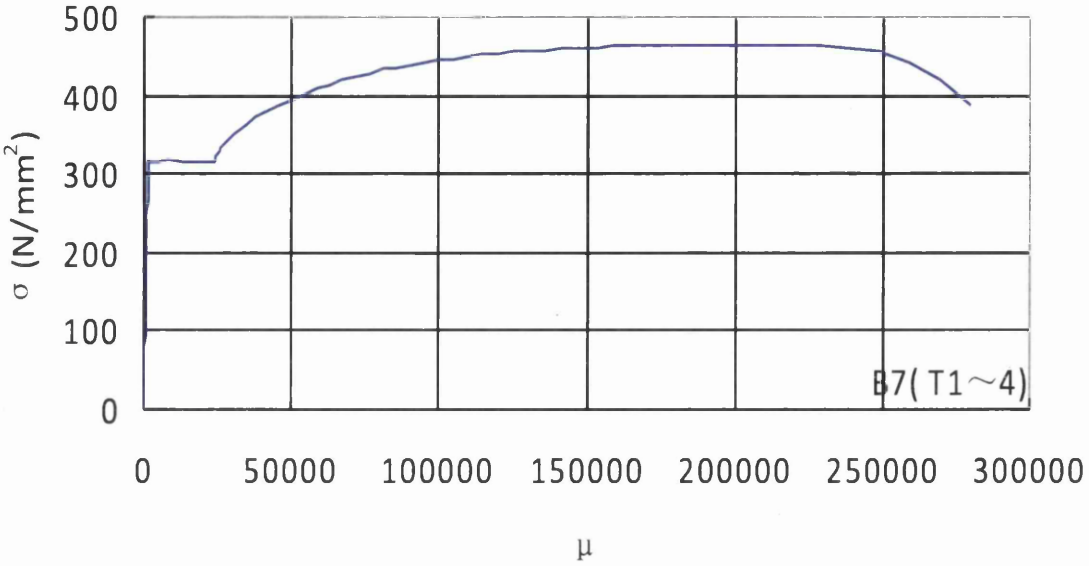
500
400
300
200
100
0
σ (N/mm²)
B7(T1～4)
0
50000
100000
150000
200000
250000
300000
μ

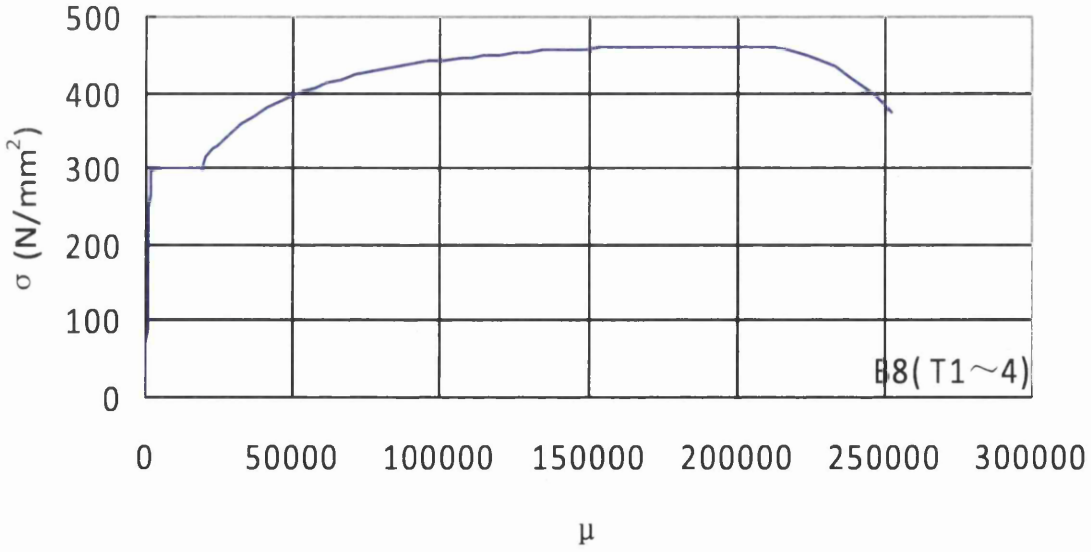
500
400
300
200
100
0
σ (N/mm²)
B8(T1～4)
0
50000
100000
150000
200000
250000
300000
μ

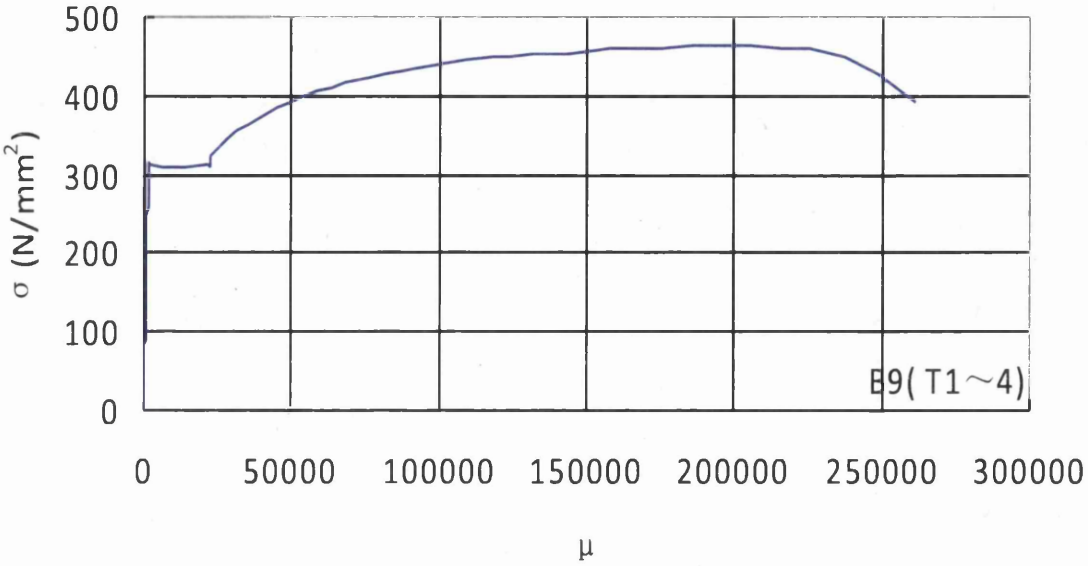
500
400
300
200
100
0
σ (N/mm²)
B9(T1～4)
0
50000
100000
150000
200000
250000
300000
μ

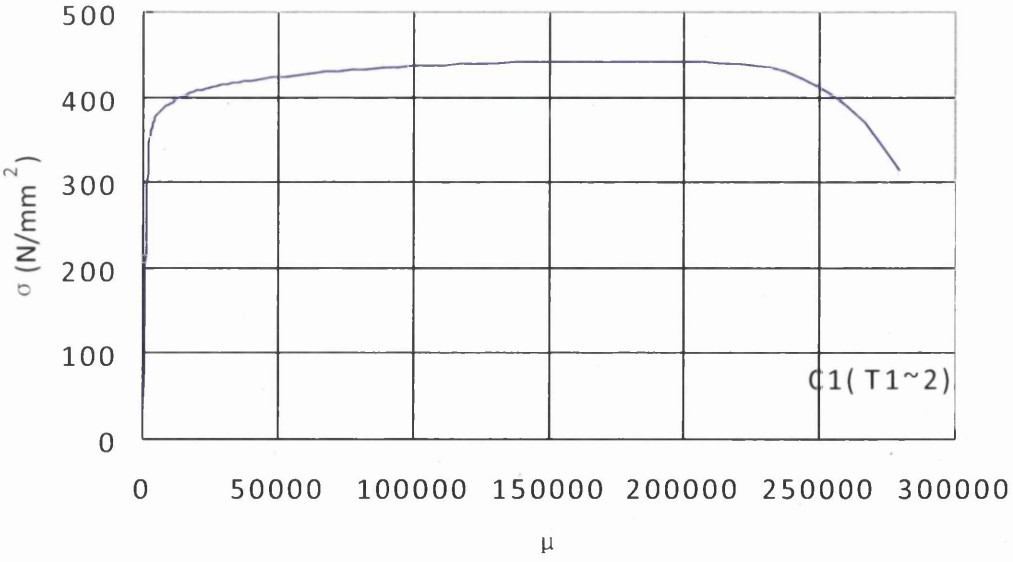
500
400
300
200
100
0
σ (N/mm²)
C1(T1~2)
0
50000
100000
150000
200000
250000
300000
μ

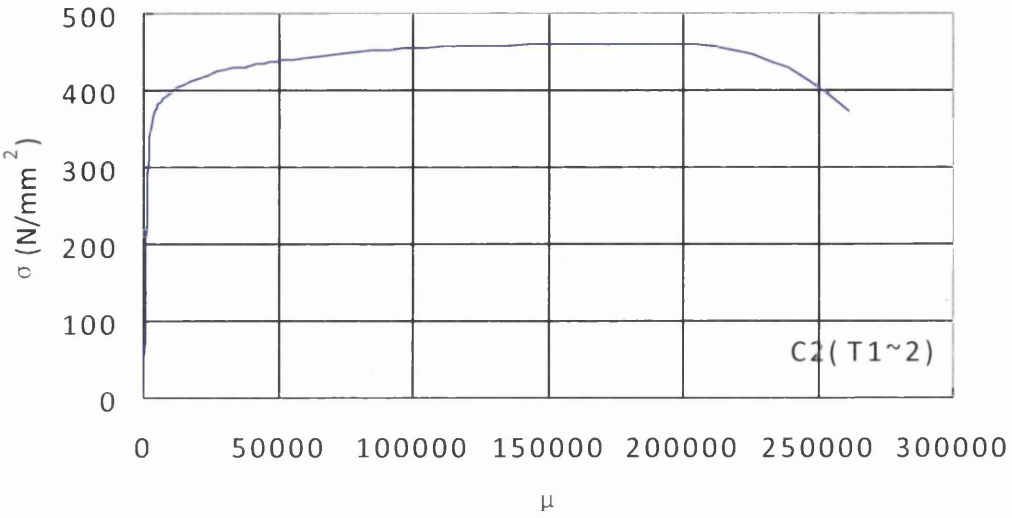
500
400
300
200
100
0
σ (N/mm 2)
C2(T1~2)
0
50000
100000
150000
200000
250000
300000
μ

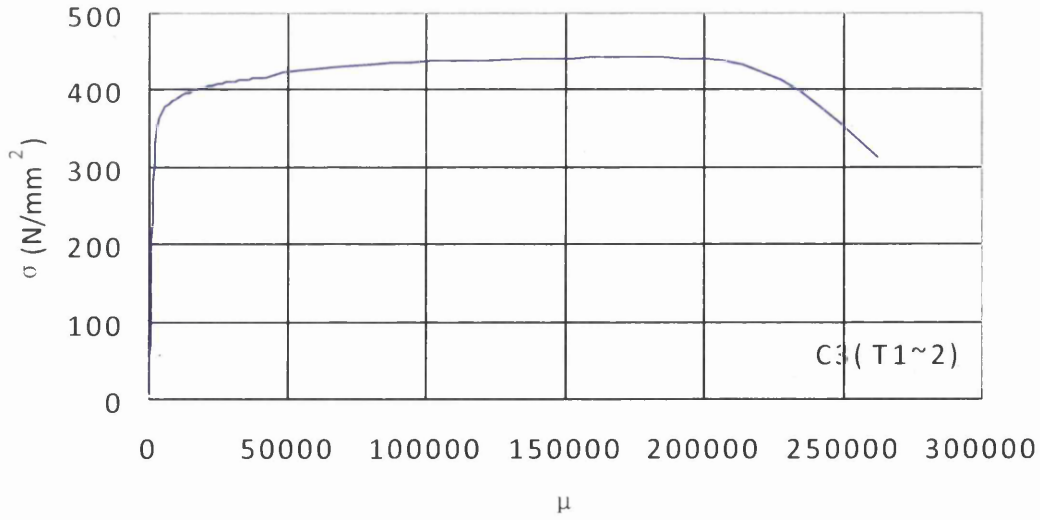
500
400
300
200
100
0
σ (N/mm 2)
C3(T1~2)
0
50000
100000
150000
200000
250000
300000
μ

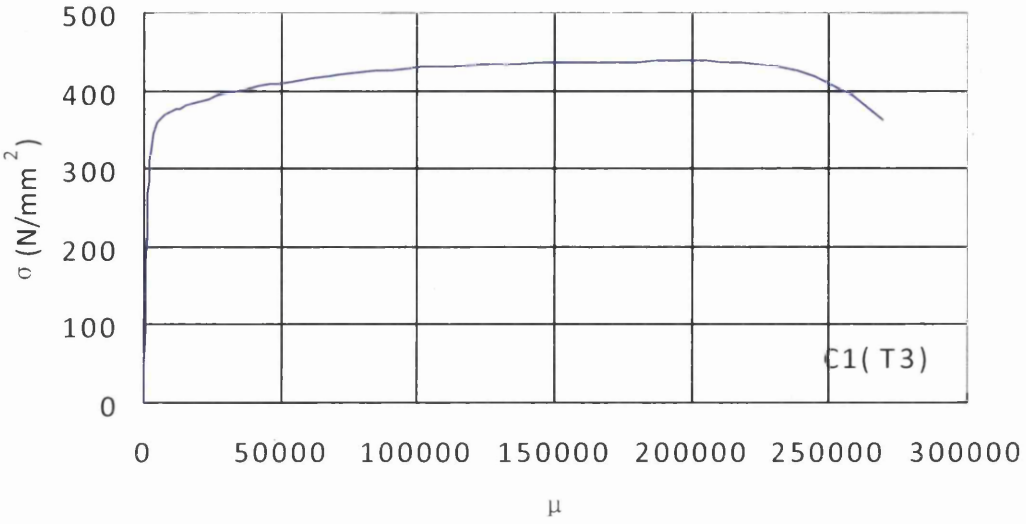
500
400
300
200
100
0
σ (N/mm 2)
C1(T3)
0
50000
100000
150000
200000
250000
300000
μ

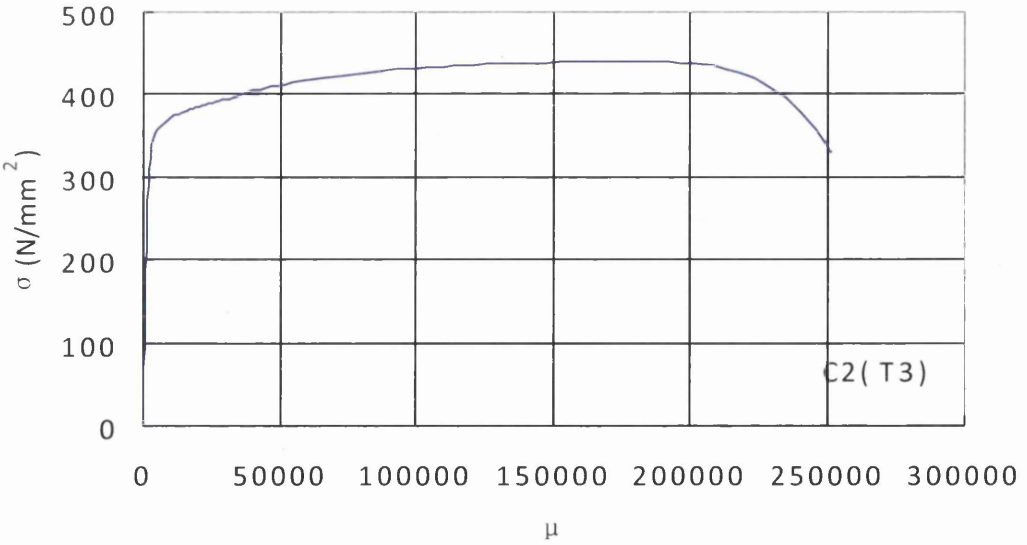
500
400
300
200
100
0
σ (N/mm 2)
C2(T3)
0
50000
100000
150000
200000
250000
300000
μ

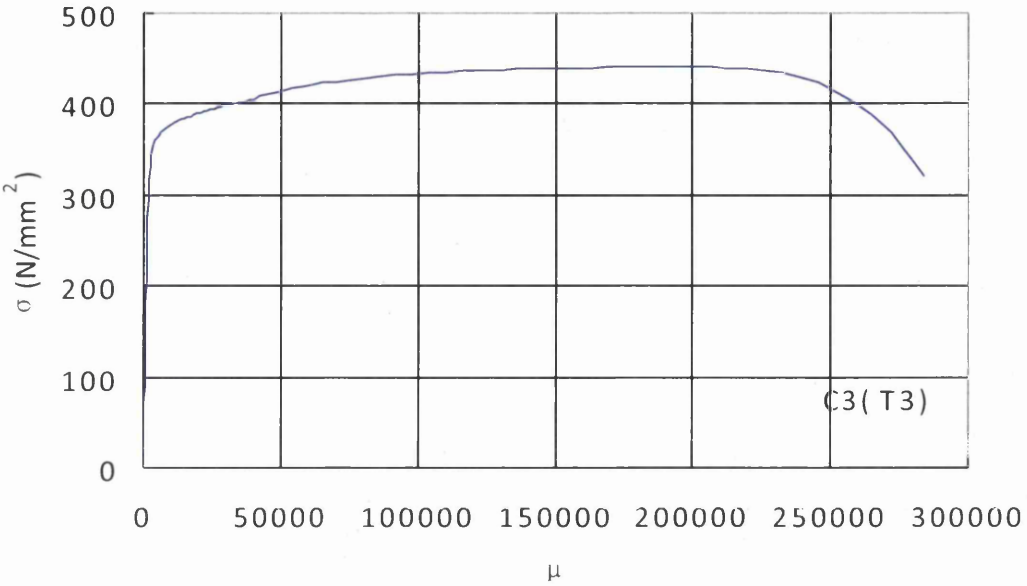
500
400
300
200
100
0
σ (N/mm 2)
C3(T3)
0
50000
100000
150000
200000
250000
300000
μ

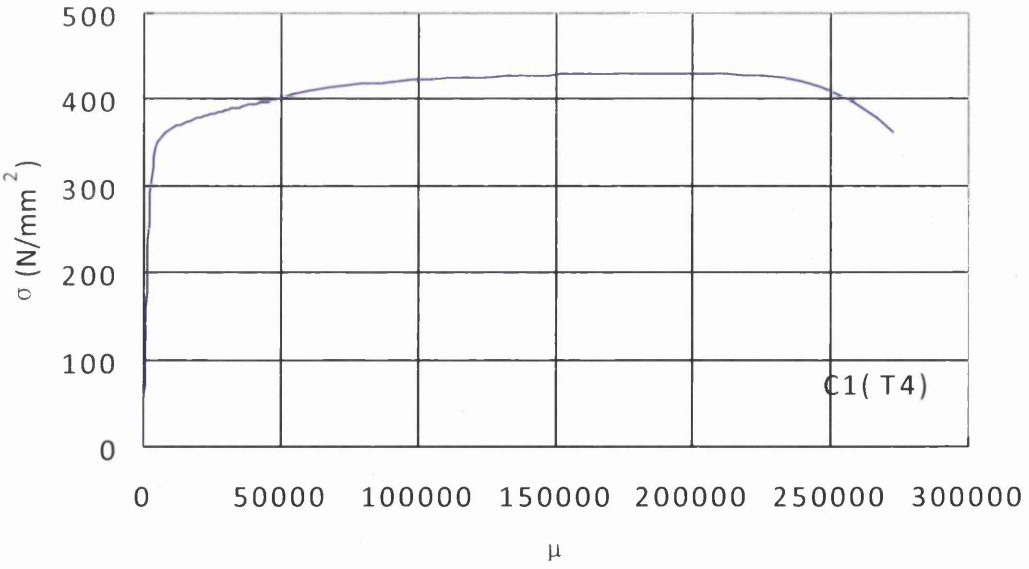
500
400
300
200
100
0
σ (N/mm 2)
C1(T4)
0
50000
100000
150000
200000
250000
300000
μ

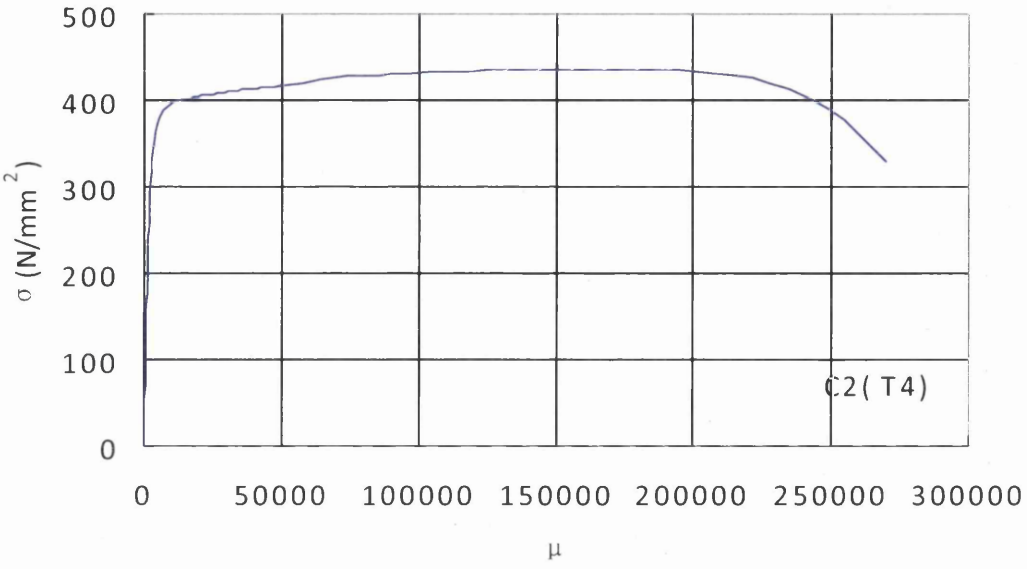
500
400
300
200
100
0
σ (N/mm 2)
C2(T4)
0
50000
100000
150000
200000
250000
300000
μ

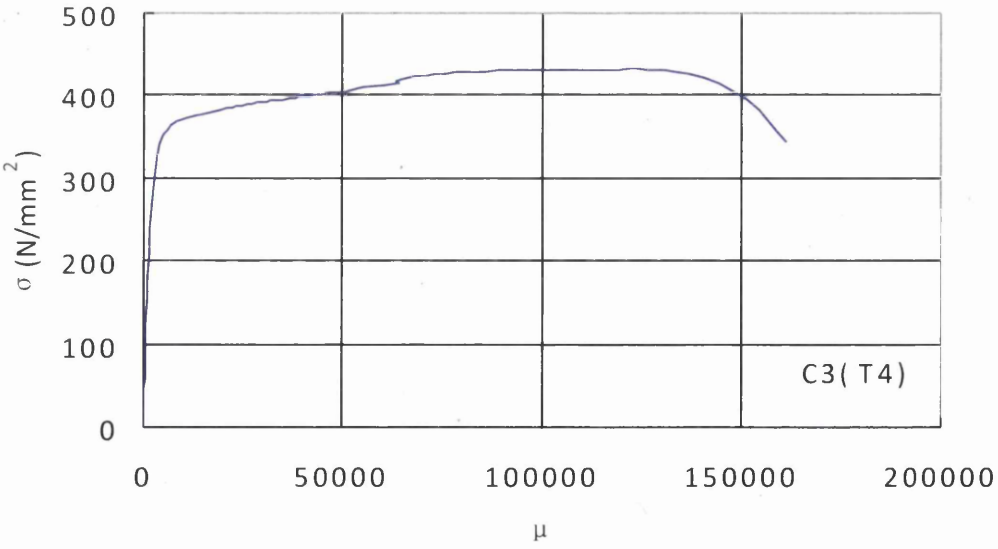
500
400
300
200
100
0
σ (N/mm 2)
C3(T4)
0
50000
100000
150000
200000
μ

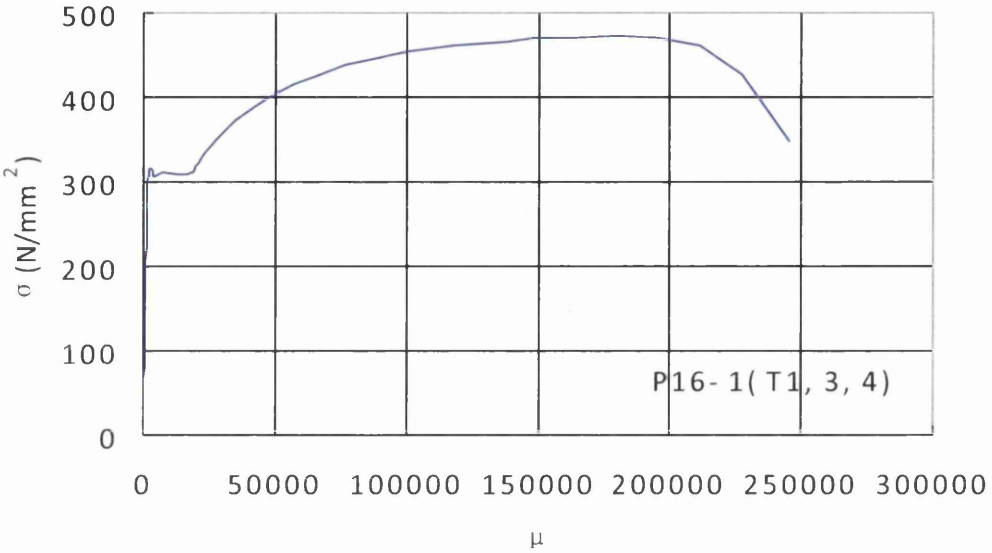
500
400
300
200
100
0
σ (N/mm 2)
P16- 1(T1, 3, 4)
0
50000
100000
150000
200000
250000
300000
μ

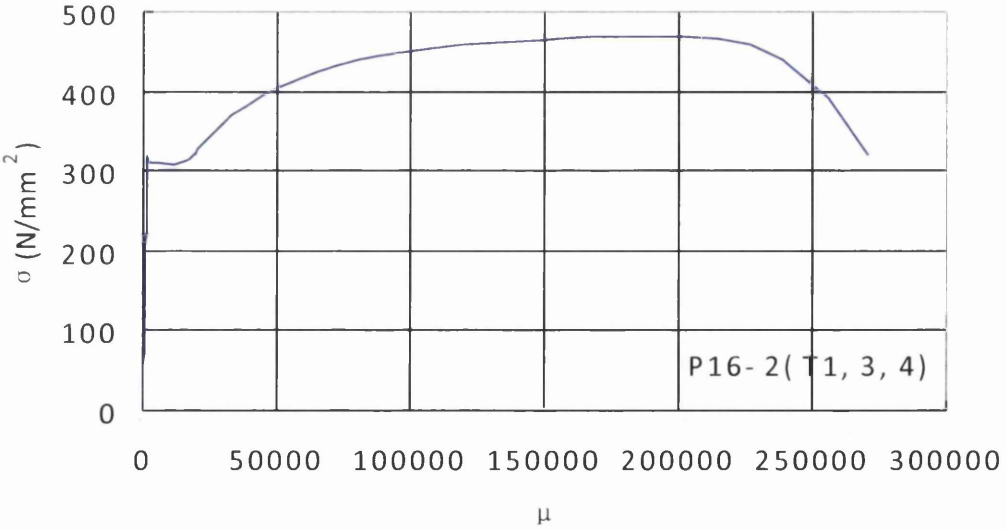
500
400
300
200
100
0
σ (N/mm 2)
P16- 2(T1, 3, 4)
0
50000
100000
150000
200000
250000
300000
μ

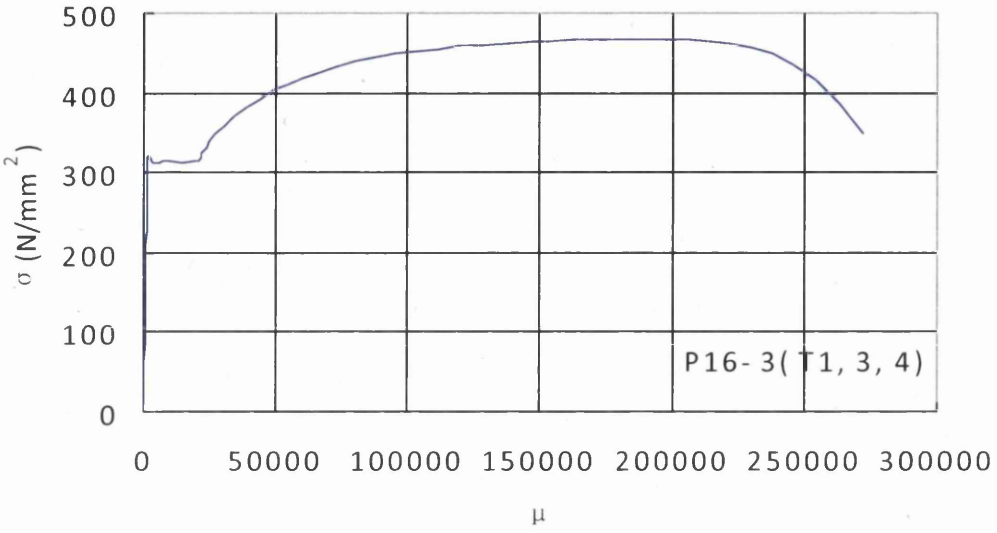
500
400
300
200
100
0
σ (N/mm²)
P16- 3(T1, 3, 4)
0
50000
100000
150000
200000
250000
300000
μ

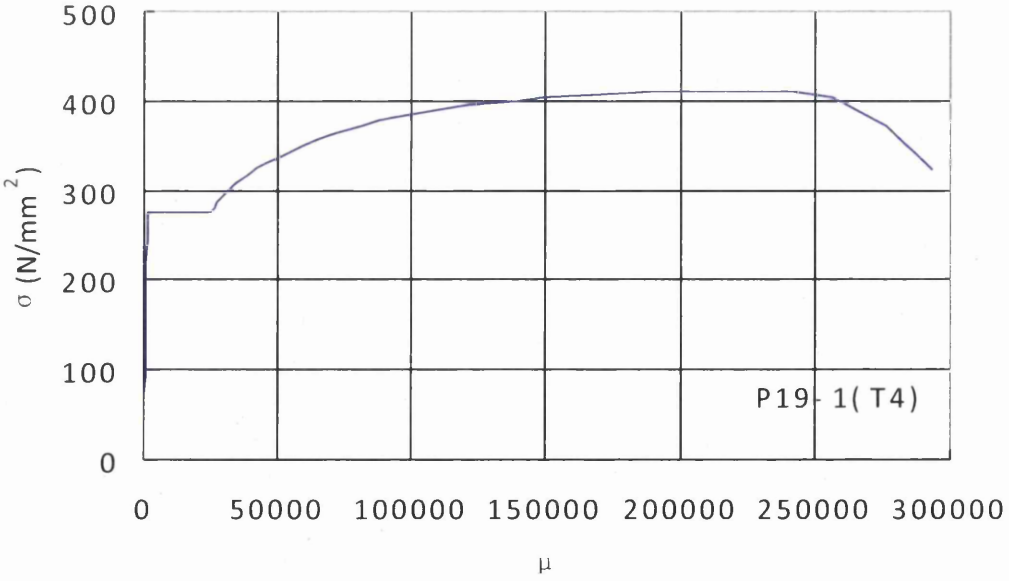
500
400
300
200
100
0
σ (N/mm²)
P19- 1(T4)
0
50000
100000
150000
200000
250000
300000
μ

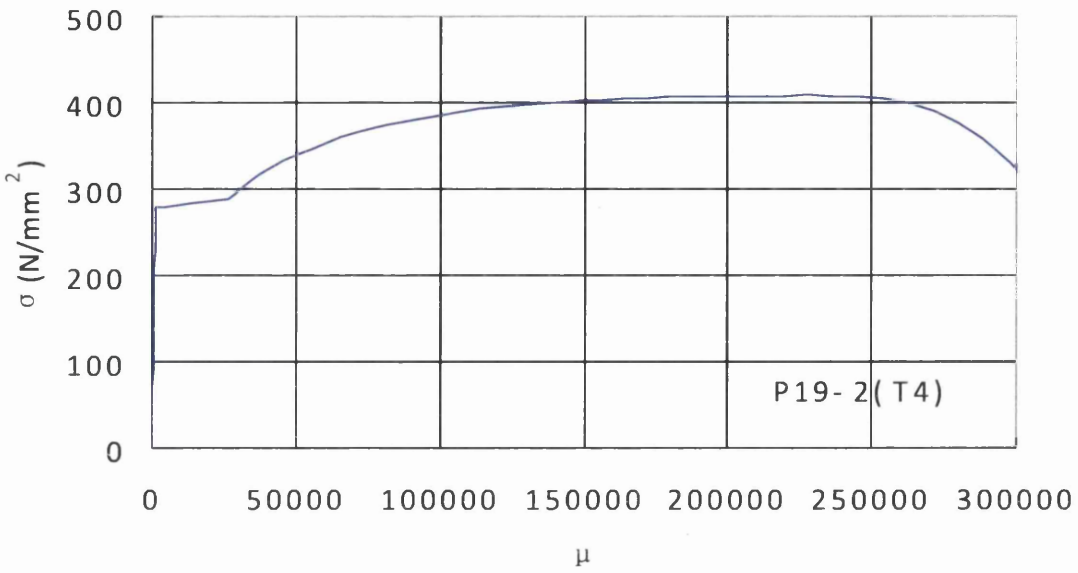
500
400
300
200
100
0
σ (N/mm 2)
P19- 2(T4)
0
50000
100000
150000
200000
250000
300000
μ

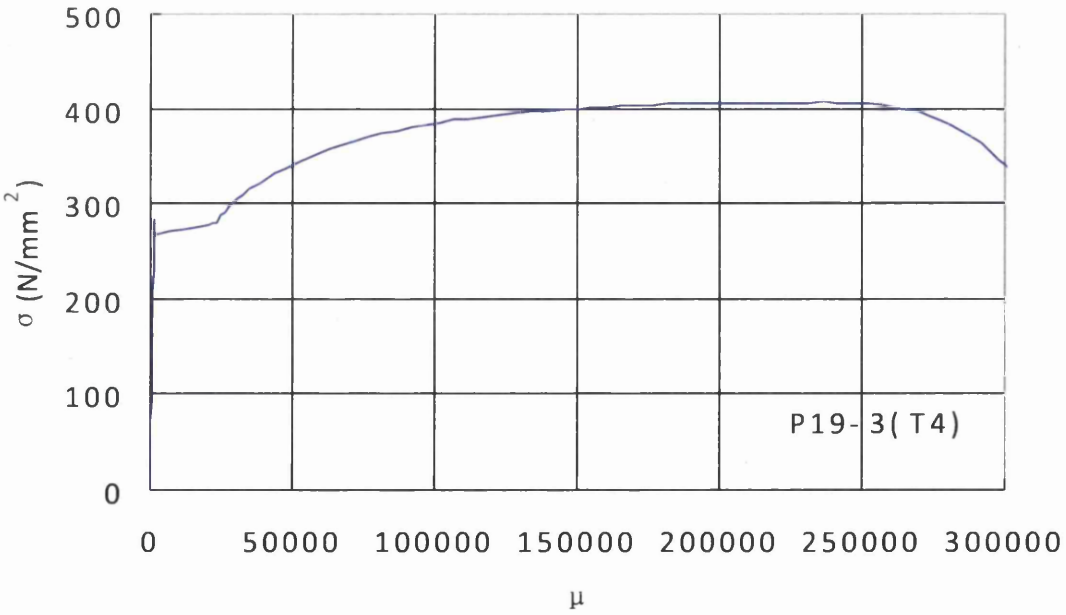
500
400
300
200
100
0
σ (N/mm 2)
P19- 3(T4)
0
50000
100000
150000
200000
250000
300000
μ

Appendix 2

Definition of cumulative plastic deformation factor

The bending moment M_m denotes the maximum beam moment at the column face. The rotation θ_m denotes the rotation of the beam segment between the loading point and the column face (see Figure a). The full plastic moment M_p is calculated by using the measured yield stresses of materials and the measured dimensions of beam sections. The elastic beam rotation θ_p at the full plastic moment is defined as the elastic component of beam rotation at $M_m = M_p$ (see Figure b). The plastic components of beam rotation at the I-th half cycle, non-dimensionalized by dividing it by θ_p, are denoted by η_i^+ and η_i^- in which the + and – symbols distinguish positive and negative moments (see Figure b). The cumulative plastic deformation factor is defined as the sum of η_i^+ and η_i^- by the specimen until failure occurs and written as:

$$\eta = \sum_i \left(\eta_i^+ + \left| \eta_i^- \right| \right)$$

The alternative definition of the cumulative plastic deformation factor is the sum of plastic energies dissipated during all the cycles, non-dimensionalized by dividing the energy by $M_p\theta_p$. According to the latter definition η_i^+ and η_i^- are written as:

$$\eta_i^+ = \frac{\sum_i W_i^+}{M_p \theta_p} \quad \text{and} \quad \eta_i^- = \frac{\sum_i W_i^-}{M_p \theta_p}$$

Where w_i denotes the energy absorbed at the I-th cycle (see Figure b)

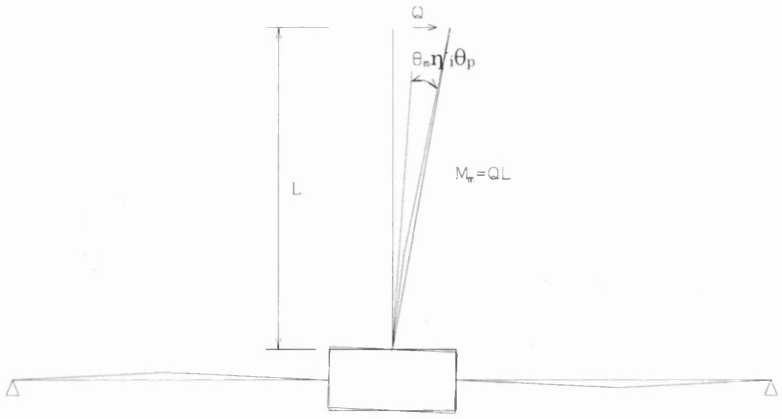

Figure a

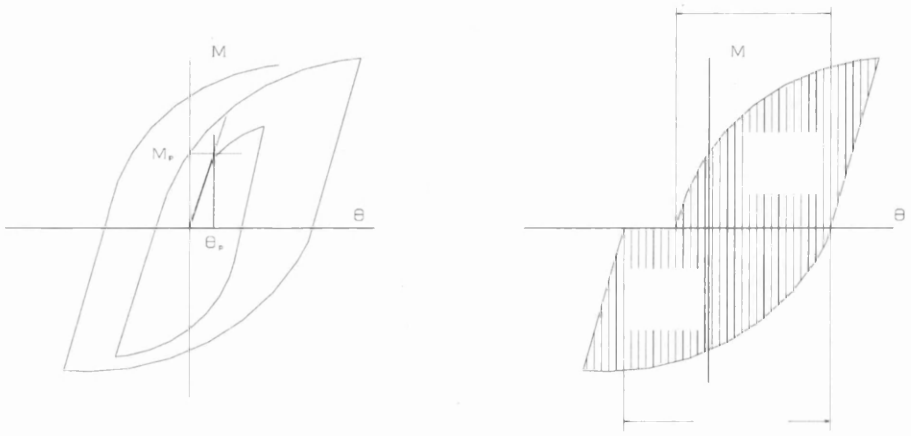

Figure b

Appendix 3

Definition of skeleton curve

The skeleton curve is constructed from a hysteretic curve by linking a portion of the curve that exceeds the maximum load in the preceding loading cycle sequentially (see Figure c)

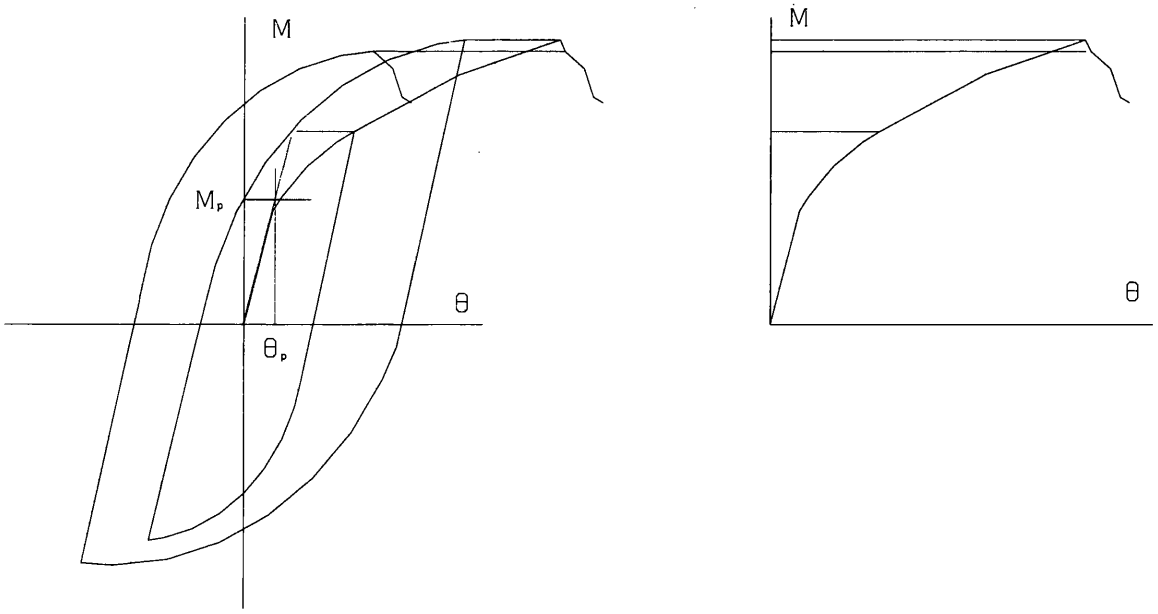

Figure c

References

[1] Kurobane. Y. 1998. Improvement of I beam-to-RHS column moment connections for avoidance of brittle fracture, Tubular Structures VIII, Y.S.Choo and G.J.van der Vegte eds. Balkema, Rotterdam, pp. 3-17

[2] AIJ 1999. WU Jian, IKEBATA Kotaro, KUROBANE Yoshiaki, MAKINO Yuji, OCHI Kenshi and TANAKA Masamitsu. Experimental Study on RHS Column to Wide Flange I-Beam Connections with External Diaphragms, AIJ, Hiroshima, pp.517-520 in Japanese

[3] J Wu. Study of New RHS Column-to-I beam Connections for avoiding tensile fracture. M.S thesis, Kumamoto University, Japan, 2000 in Japanese

[4] ABAQUS, ABAQUS v 6.2 Manuals, Hibbitt, Karisson and Sorenson Inc.

[5] CEN 1994. Eurocode 8-Design provisions for earthquake resistance of structure, Part 1-1, 1-2, 1-3, ENV 1998-1-1, 1-2, 1-3, European Committee for Standardization

[6] AIJ 1996. The state of Art Report on the Structural Behavior of Steel Connections. Architectural Institute of Japan, Tokyo, Japan, in Japanese

[7] AIJ 1990. Technical recommendations for steel construction for buildings. Part 1 Guide to steel-rib fabrications. AIJ pp. 112-124.

[8] AIJ 1996. The manual of design and construction of cold forming RHS columns. AIJ. pp. 39-40, 76.

[9] AIJ Kinki 1997. Full-scale test on plastic rotation capacity of steel wide-flange beams connected with square tube steel columns. Committee on Steel Building Structures. The Kinki Branch of the AIJ. Osaka, in Japanese

[10] ICBO 1994. Uniform Building Code, International Conference of Building Officials, Whittier, CA

[11] Barsom, J.M. and Rolfe, S.T. Fracture and fatigue control in structures. ASTM international 1999

[12] R. Q. Zhang, X. Y. Zhan. Nonlinear finite element analysis. Chongqing University Press. 1990 in Chinese

[13] K. Miura, Y. Makino, Y. Kurobane, M. Tanaka, K. Tokudome and G.J. van der Vegte. Testing of beam-to-RHS column connections without weld access holes. International Offshore and Polar Engineering Conference, Stavanger, Norway, 2001

[14] Suita, K, Tanaka, T. 2000. Flexual strength of beam web to square tube column joints. Summaries of Technical Papers of Annual Meeting Architectural Institute of Japan 2000, pp.731-732, in Japanese

[15] J. Wu and Y.T. Feng. 2013. Finite element simulation of new RHS column-to-I beam connections for avoiding tentsile fracture. Journal of Constructional Steel Research 86(2013) 42-53

[16] Tadaharu Nagao, Tsuyoshi Tanaka and Hisashi Nanba. Performance of beam-column connections in steel structures. 13th World Conference on Earthquake Engineering, Vancouver, B.C.,Canada 2004

[17] Tanaka, N 1999. Study on Structural Behavior of Square Steel Column to H-Shaped Steel Beam Connections. Doctoral Dissertation Submitted to Kummoto Universtiy, in Japanese

[18] G.J. van der vegte and Y. Makino, Numerical simulations of bolted connection: the implicity versus the explicit approach. Connections in Steel Structure V, Amsterdam, 2004

[19] Krishnamurthy, N., Huang, H.T., Jeffrey, P.K. and Avery, L.K., (1979). Analytical M-θ curves for end-Plate connections. Journal of Structural Divison, ASCE, Vol. 105, No.1 pp. 133-145.

[20] Sherbourne, A.N. and Bahaari, M.R., (1994). 3D Simulation of end-Plate bolted connections. Journal of Structural Engineering, Vol. 120, No. 11, pp.3122-3136

[21] Choi, C.K. and Chung, G.T., (1996). Refined three-dimensional finite element model for end-plate connection. Journal of Structural Engineering, Vol. 122, No. 11, pp. 1307-1316

[22] Bursi, O.S. and Jaspart, J.P., (1997). Benchmarks for finite element modelling of bolted steel connections. Journal of Constructional Steel Research. Vol. 44, No. 3, pp. 225-262

[23] Wheeler, A.T., Clarke M.J. and Hancock, G.J., (2000). FE modelling of four bolt, tubular moment end-plate connections. Journal of Structural Engineering, Vol. 126, No. 7, pp.816-822.

[24] Swanson, J.A. and Leon, R.T., (2000). Bolted steel connections: tests on t-stub components. Journal of Structural Engineering, Vol. 126, No. 1, pp. 50-56

[25] AIJ, (2001). Recommendatin for design of connections in steel structures. Architectural Institute of Japan (in Japanese).

[26] Engelhardt MD, Sabol TA. (1994). Testing of welded steel moment

connections in response to Northridge earthquake. American Institute of Steel Construction.

[27] Engelhardt M.D, Sabol T.A. (1998), Reinforcing of steel moment connections with cover plates: Benefits and limitations. Engineering Structures. 20(4_6), 510_520

[28] Aschheim M-A (2000), Moment-resistant structure, sustainer and method of resisting episodic loads. United State patent, patent number: 6,012,256

[29] Wilkinson S, Hurdmanb G, Crowtherb A. (2006), A moment resisting connection for earthquake resistant structures. Journal of Constructional Steel Research. 62,295_302

[30] SAC (1996), Experimental investigations of beam-column subassemblies. Report No.: SAC 96-01. SAC joint venture, Sacramento, Calif.

[31] FEMA350 (2000), Recommended Seismic Design Criteria for New Steel Moment Frame Buildings.

[32] American Welding Society 1994, Structural Welding Code, AWS D1.1-94

[33] Kuma V, M.D German & C.F. Shih 1981, An Engineering Approach for Elastic-plastic Fracture Analysis. NP-1931, EPRI

[34] Tada. H, P.C Paris and G.R. Irwin 1973, The Stress Analysis of Cracks Handbook, Del Research Corporation Hellertown, Pennsylvania.

[35] Moura.B, Shih, C.F., A Treatment of Crack Tip Contour Integrals. International Journal of Fracture, 1987, 35: 295-100

[36] Shivakumar, K.N., Raju, I.S., An Equivalent Doman Integral Method for Three-dimensional Mixed-mode Fracture Problem. Engineering Fracture Mechanics, 1992, 42: 935-959.

[37] Cook. R.D, Malkus. D.S and Plesha. M.E. (1989), Concepts and applications of finite element analysis. John Wiley & Sons, Inc.

[38] Bonet. J and Wood. R.D. (1997), Nonlinear continuum mechanics for finite element analysis. Cambridge University Press

[39] Belytschko. T, Liu. W.K and Moran. B. (2000), Nonlinear finite elements for continua and structures. John Wiley & Sons Ltd

[40] Lemaitre. J and Chaboche. J.-L. (1990), Mehcanics of solid materials. Cambridge University Press

[41] AISC, 2005: Specification for structural steel buildings. ANSI/AISC 360-05, American Institute ofSteel Construction, Chicago, Ill., USA.

[42] ASTM, 2007a: Standard specification for pipe, steel, black and hot-dipped, zinc-coated, welded and seamless. ASTM A53/A53M-07, ASTM International, West Conshohocken, Pa., USA.

[43] ASTM, 2007b: Standard specification for cold-formed welded and seamless carbon steel structural tubing in rounds and shapes. ASTM A500/A500M-07, ASTM International, West Conshohocken,
Pa., USA.

[44] ASTM, 2007c: Standard specification for hot-formed welded and seamless carbon steel structural tubing. ASTM A501-07, ASTM International, West onshohocken, Pa., USA.

[45] AWS, 2008: Structural welding code – Steel. 21st Edition, AWS D1.1/D1.1M:2008, American Welding Society, Miami, Fl, USA.

[46] Packer, J.A., 2007: Design with hollow structural sections – A report on recent developments in the USA. Proceedings 5th International Conference on Advances in Steel Structures, Singapore, Vol. II,pp. 228-237.

[47] Zhao, X.-L., Wardenier, J., Packer, J.A., and Vegte, G.J. van der, 2008: New IIW (2008) static design recommendations for hollow section joints, Proceedings 12th International Symposium on Tubular Structures, Shanghai, China, Tubular Structures XII, Taylor & Francis Group, London, UK,pp. 261-269.

[48] Szlendak, J., and Brodka, J., 1986a: Design of strengthen frame RHS joints. Proceedings International Meeting on Safety Criteria in Design of Tubular Structures, Tokyo, Japan, pp. 159-168.

[49] Packer, J.A., Wardenier, J., Kurobane, Y., Dutta, D., and Yeomans, N., 1992: Design guide for rectangular hollow section (RHS) joints under predominantly static loading. 1st Edition, CIDECT series 'Construction with hollow sections' No. 3, TÜV-Verlag, Köln, Germany.

[50] Owen, J.S., Davies, G., and Kelly, R.B., 1996: A comparison of the behaviour of RHS bird beak Tjoints with normal RHS and CHS systems. Proceedings 7th International Symposium on Tubular Structures, Miskolc, Hungary, Tubular Structures VII, Balkema, Rotterdam, The Netherlands, pp. 173-180.

[51] Ono, T., Iwata, M., and Ishida, K., 1991: An experimental study on joints of new truss system using rectangular hollow sections. Proceedings 4th International Symposium on Tubular Structures, Delft, The Netherlands, Delft University Press, Delft, The Netherlands, pp. 344-353.

[52] Ono, T., Iwata, M., and Ishida, K., 1993: Local failure of joints of new truss system using rectangular hollow sections subjected to in-plane bending moment. Proceedings 5th International Symposium on Tubular Structures, Nottingham, UK, Tubular Structures V, E & FN Spon, London,UK, pp. 503-510.

[53] Mang, F., Bucak, Ö., and Wolfmuller, F., 1983: The development of recommendations for the design of welded joints between steel structural hollow sections (T- and X-type joints). University of Karlsruhe, Germany, Final Report on ECSC Agreement 7210 SA/l 09 and CIDECT Program 5AD.

[54] Lu, L.H., 1997: The static strength of I-beam to rectangular hollow section column connections. Ph.D. Thesis, Delft University Press, Delft, The Netherlands.

[55] Lazar, B.E., and Fang, P.J., 1971: T-type moment connections between rectangular tubular sections. Research Report, Sir George Williams University, Montreal, Canada.

[56] IIW, 1989: Design recommendations for hollow section joints – Predominantly statically loaded. 2nd Edition, International Institute of Welding, Commission XV, IIW Doc. XV-701-89.

[57] IIW, 2009: Static design procedure for welded hollow section joints – Recommendations. 3rd Edition, International Institute of Welding, Commission XV, IIW Doc. XV-1329-09.

[58] Ishida, K., Ono, T., and Iwata, M., 1993: Ultimate strength formula for joints of new truss system using rectangular hollow sections. Proceedings 5th International Symposium on Tubular Structures, Nottingham, UK, Tubular Structures V, E & FN Spon, London, UK, pp. 511-518.

[59] Kanatani, H., Fujiwara, K., Tabuchi, M., and Kamba, T., 1980: Bending tests on T-joints of RHS chord and RHS or H-shape branch, CIDECT Report 5AF-80/15.

[60] Galambos, T.V. (Ed.), 1998: Guide to stability design criteria for metal structures, 5th Edition, Structural Stability Research Council, John Wiley & Sons, New York, USA.

[61] Ghosh, A., and Morris, G., 1981: Behaviour of tubular steel trusses with cropped webs. Canadian Journal of Civil Engineering, Vol. 8, No. 1, pp. 51-58.

[62] Grundy, P., and Foo, E.K.J., 1991: Performance of flattened tube connections. Proceedings 4th International Symposium on Tubular Structures, Delft, The Netherlands, Delft University Press, Delft, The Netherlands, pp. 251-258.

[63] Horne, M.R., and Morris, L.J., 1985: Plastic design of low-rise frames. Collins, London, UK.

[64] Driver, R.G., Grondin, G.Y., and Kulak, G.L., 2006: Unified block shear

equation for achieving consistent reliability. Journal of Constructional Steel Research, Vol. 62, No. 3, pp. 210-222.

[65] Chen, Y., Liu, D.K., and Wardenier, J., 2005: Design recommendations for RHS-K joints with 100% overlap. Proceedings 15th International Offshore and Polar Engineering Conference, Seoul, Korea, Vol. IV, pp. 300-307.